CHEMICAL REVIEWS

Recent Advances in the Theory and Molecular Simulation of Biological Electron Transfer Reactions

Jochen Blumberger*

Department of Physics and Astronomy, University College London, Gower Street, London WC1E 6BT, U.K.

$$H_{ab} = \langle \Psi_a | \mathcal{H} | \Psi_b \rangle$$

$$\lambda(k) = \frac{2}{\pi} \int_k^\infty d\omega \frac{J(\omega)}{\omega}$$

CONTENTS

References   11229

1. INTRODUCTION AND OVERVIEW

The transfer and transport of electrons through biological matter is one of the key steps underlying cellular energy harvesting, storage, and utilization, enabling virtually all cellular activity. The two most important and well-established examples of electron transfer (ET) in biology, which are at the origin of our very own existence, are the reactions catalyzed by the redox protein machinery in photosynthetic cells, converting sunlight into reduction equivalents (Figure 1A),[1−3] and the electron transport chain in the mitochondria, catalyzing the transformation of reduction equivalents in readily usable energy (ATP) (Figure 1B).[4−6] In recent years we have seen compelling evidence that biological ET is not restricted to intracellular processes. Certain microbes have developed an extraordinary type of respiration in response to conditions of low oxygen concentration. In a process known as extracellular respiration they oxidize organic matter inside the cell and transport the electrons generated across the cellular envelope to extracellular space for reduction of insoluble transition-metal oxides, effectively "breathing rocks" in place of oxygen (Figure 1C).[7−9]

In addition, there is currently strong activity worldwide to exploit the exquisite redox properties of naturally evolved metalloenzymes for production of renewable fuels in bioelectrochemical cells, e.g., hydrogenase for H_2 oxidation and production, see Figure 2A,[10−18] and CO-dehydrogenase for CO oxidation and CO_2 reduction, Figure 2B.[18−22] Furthermore, bionanoelectronic devices are being designed for sensing, signaling, electronic communication, and possible incorporation in living systems. For instance, protein containing filaments evolved in "rock breathing" microbes have been recently incorporated in a biological field effect transistor exhibiting charge mobilities comparable to the ones of organic semiconducting materials (Figure 2C−E).[23]

In parallel to these exciting recent developments on the experimental front, it becomes increasingly important to further our theoretical understanding of biological ET so as to improve our ability (i) to explain experimental observations, (ii) to predict new phenomena and mechanisms, and (iii) to guide the design of new experiments, new redox active biological materials, and devices. From a theoretical perspective, the most fascinating characteristics of biological ET are probably the length and time scales at which this phenomenon occurs: from picoseconds (ps) for charge separation in reaction center proteins to milliseconds (ms) for long-range ET in cytochromes,[24−26] and from nanometer electron tunneling between cofactors[24−26] to electron transport on the centimeter scale in long, filamentous bacteria that form living electrical cables in sediments.[27] What are the mechanisms at work that allow for the realization of such disparate time and length scales? Why is biological ET so efficient, specific, and often so remarkably reversible? How does protein structure determine redox function? Can we develop computational tools that will allow us to control and tailor biological ET through targeted mutations?
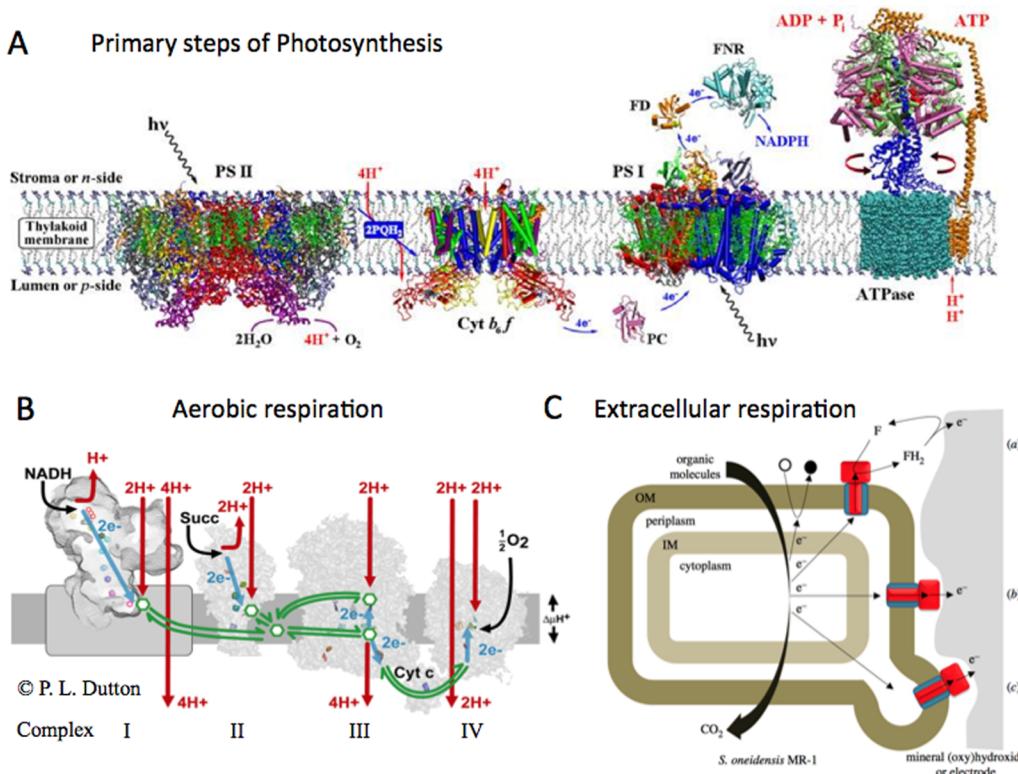
The field has come a long way from the early ideas of bridge-mediated electron tunneling, at first proposed by Halpern et al. in the early 1960s,[28] and the square barrier tunneling model of Hopfield in the 1970s.[29] These structureless models of the physicists were subsequently replaced by more refined models

of physical chemists, honoring for the first time the existence of the atomic structure of biomolecules. In the late 1980s Beratan and co-workers proposed the idea that electrons tunnel along specific pathways connecting electron donating and accepting cofactors, thereby capturing a potentially complicated multi-electron quantum mechanical process in a human-accessible, comprehensible picture.[30,31] Now, in the era of computational molecular science and high performance computing, these elegant models are becoming increasingly complemented, informed, or replaced by numerical data as obtained by solving, though approximately, the most fundamental equations of quantum mechanics (many-electron Schrödinger equation) in combination with ensemble averaging over the strongly fluctuating structures of biomolecules.
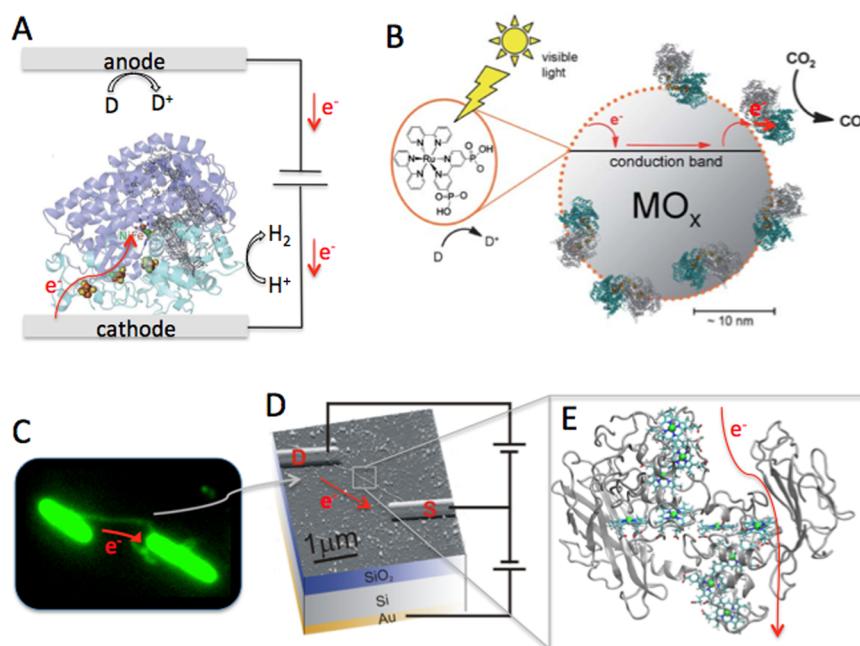
The aim of this review is to give a critical account of both analytical and numerical methods that have been developed to investigate, characterize, quantify, and explain biological ET reactions; see Figure 3 for an outline. Analytical ET theories (blue box in Figure 3) have been and remain of central interest as they are the condensed extracts of physical insight and they are of some generality within certain, well-defined limits. Nowadays, theories are increasingly informed by computer simulation methods that provide numerical estimates for ET parameters that enter the rate equations (green box in Figure 3). Moreover, atom-scale simulation methods allow one to understand and interpret these parameters in terms of microscopic protein structure and dynamics. Yet, any analytic ET theory is the result of a number of simplifying assumptions. Direct charge propagation schemes can be used to test some of these assumptions (red box in Figure 3). These methods are, in principle, very powerful and may lead to entirely new pictures for ET in situations where existing theories do not apply. Moreover, they can provide benchmark data for the formulation of new analytic theories in such regimes.

While focus is firmly placed on theoretical and computational methods, a brief summary of experimental approaches that have prompted many of the theoretical/computational developments is given in section 2. In section 3, I review the traditional picture of single step ET reactions and summarize the very basic theoretical concepts and established ET rate expressions. I believe this tutorial-style section gives the nonexpert readers the necessary background to understand the more advanced concepts in section 5. The expert reader may skip section 2 and may proceed directly to section 4, where approaches are described for the calculation of the ET parameters, electron coupling matrix elements, reorganization free energy, and driving force. Modern quantum mechanics (QM) based computational techniques are reviewed such as constrained and fragment orbital density functional theory as well as QM/molecular mechanics (MM) and classical molecular dynamics (MD) for the calculation of free energies. Focus is placed throughout on atomistic simulation methods. Continuum electrostatic methods, while undoubtedly useful in many situations, are not treated here, and I refer to the literature instead.[32−34]

Section 5 is the centerpiece of this review. I reexamine and critically discuss four topics of burgeoning interest that have attracted, and are very likely to continue to attract, much attention in the field. The first topic (section 5.1) concerns the proposal of a new mechanism for multistate biological ET across a chain of biological redox active units, denoted the flickering resonance (FR) mechanism.[35] Recently suggested by Beratan, Skourtis and co-workers, I will review the physical

Figure 1. Biological electron transfer in native systems. (A) Primary steps of photosynthesis.[366] (B) Aerobic respiration.[367] (C) Extracellular respiration. Reprinted with permission from ref 347. Copyright 2015 The Royal Society.

Figure 2. Examples for biological electron transfer in (nano)biotechnological applications. (A) Production of H_2 from protons and electrons, catalyzed by hydrogenase adsorbed on an electrode. Protein structure adapted with permission from ref 18. Copyright 2014 Royal Society of Chemistry. (B) Reduction of CO_2 by the enzyme carbon-monoxide dehydrogenase, adsorbed on a metal oxide particle. Adapted with permission from ref 20. Copyright 2011 Royal Society of Chemistry. (C) Two bacterial cells from *Shewanella oneidensis* MR-1 connected by an electronically conducting biological nanowire. Adapted with permission from ref 9. Copyright 2014 National Academy of Sciences. (D) Field effect transistor made of a nanowire similar to the one shown in (C). Adapted from ref 23. Copyright 2013 American Chemical Society. (E) Crystal structure of the deca-heme protein MtrF (PDB code 3PMQ),[257] a member of a family of multi-heme cytochromes thought to confer electronic conductivity to the nanowires shown in (C) and (D).

picture and the rate expression for this mechanism and make a comparison with the established superexchange (SE) and

hopping models. The second topic (section 5.2) is on methods that deal with ultrafast ET, such as the nonergodicity correction
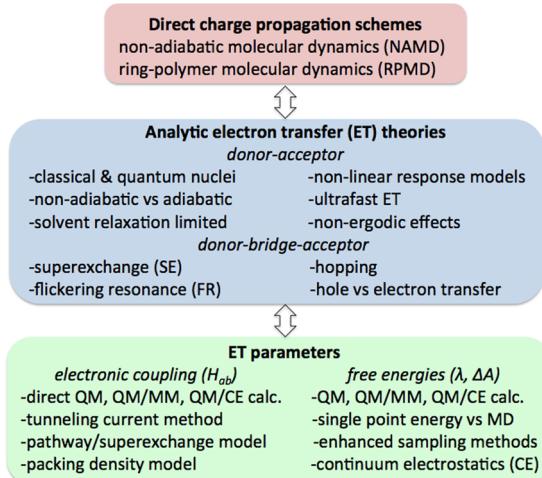
recently proposed by Matyushov and co-workers[36] and the explicit nonadiabatic charge propagation schemes implemented by Kubař, Elstner, and co-workers.[37,38] With the third topic (section 5.3) I will review the recent suggestion that nonergodic effects, such as the dynamical arrest of slow protein conformational transitions, accelerate biological ET rates.[36] A simple modification of the linear free energy relationship is reexamined that may be able to describe this phenomenon quantitatively. The fourth topic (section 5.4) is on recent developments of path-integral methods, specifically ring-polymer molecular dynamics for rigorous calculation of ET rates that include nuclear quantum effects.[39,40]

In section 6 I review a few selected computational studies on ET in proteins and DNA to illustrate some of the concepts and methods that are presented in sections 4 and 5. I discuss the performance of QM/MM-type and classical MD simulations for the calculation of reorganization free energy in Ru-modified proteins and in cytochrome c oxidase. These systems can be considered as the "fruit flies" of biological ET for which experimental ET data is available, thanks to the longstanding efforts of Gray, Dutton, and others. Some of the critical issues that are important for successful calculation of this quantity are discussed. Possible ET mechanisms in multi-heme cytochromes are reexamined, specifically the SE, FR, and hopping models with parameters obtained from QM/MM and classical MD simulations. Ultrafast hole transfer studies in DNA are then briefly reviewed, focusing on a recent reinterpretation of experimental results in terms of the FR model and summarizing the results obtained from explicit nonadiabatic charge propagation schemes in short DNA strands. Application of the latter method to DNA photolyase is also briefly reviewed as an example where the assumption of equilibrium statistical mechanics gives qualitatively incorrect results.

This review is concluded in section 7 with suggestions for further tests of the novel concepts and mechanisms described in section 5 and with a perspective on future opportunities for computational biological ET. I hope it will complement other reviews and perspectives in the field that have appeared some time ago[24–26,41–48] and more recently.[36–38,49–59] Related topics not covered here are proton transfer coupled ET (see refs 60–66 for recent reviews), photoinitiated biological ET reactions (reviewed in ref 67), excitation energy transfer (reviewed in ref 68), and electrochemical ET between electrodes and biomolecules (reviewed in refs 10, 13, 18, 69, and 70).

2. EXPERIMENTAL APPROACHES

Perhaps one of the most remarkable aspects of biological ET reactions is the wide range of time scales on which these reactions occur: from picoseconds (ps) for primary charge separation in photosynthetic reactions centers to milliseconds (ms) for long distance tunneling in cytochromes and blue copper proteins. A number of different experimental approaches were developed over the past decades to probe biological ET over these vastly different time scales, including optical spectroscopy,[26,71–75] NMR (ref 76 and references therein), pulsed radiolysis,[77–81] and electrochemical techniques.[10,13,18,22,69,70,82–87] Moreover, conductive atomic force microscopy (AFM) and scanning tunneling microscopy (STM) techniques have been recently developed, to probe charge transport across multiple cofactors in single proteins[88,89] and in micrometer-long bacterial nanowires.[90] In the following I summarize some of the optical techniques whose applications

Figure 3. Overview of electron transfer theories and computational methods discussed in this review.

to ET proteins have prompted the development of many theoretical concepts and modern computational tools, some of which I shall discuss in later sections.

In their pioneering work in the 1980s, Gray and co-workers developed a laser flash-quench triggering method for the measurement of ET rates in small Ru-modified metalloproteins including cytochromes and azurin.[26,91] A photosensitizer, typically an inorganic Ru complex, is attached to a His residue at the surface of the protein. Upon photoexcitation of Ru^{2+} by a short laser flash, a quencher (Q) is reduced in a bimolecular ET reaction, triggering intramolecular ET from the transition metal containing protein cofactor to the oxidized Ru^{3+} label. Reduction of the cofactor by the quencher closes the cycle. During the reaction sequence the oxidation state of the metal center is monitored by transient absorption spectroscopy and the rate constant for ET is extracted from the absorption decay. A number of different photoexcitable electron donors have been developed also by other groups and successfully applied to study ET in metalloproteins.[74,75,92]

Gray, Winkler, and co-workers showed that 20 Å coupling limited Fe(II) to Ru(III) and Cu(I) to Ru(III) electron tunneling in Ru-modified cytochromes and azurins can occur on the microsecond time scale both in solutions and in crystals.[26,91] Measurements for proteins with different distances between protein metal center and Ru label yielded estimates for the distance decay of electronic coupling in proteins, and the use of high-potential Ru complexes enabled the experimental estimation of reorganization free energies for protein ET (to be defined in section 3). More recently, evidence was found for tryptophan-accelerated multistep electron tunneling (hopping) in Re-modified azurins[93] and across a protein–protein interface.[94] Several reviews by this group are available to which I refer for a detailed summary and discussion.[26,56,91,95] Their measurements on small cytochromes and azurins have obtained benchmark status and provided a very fertile ground for theoretical and computational developments in the past 30 years;[30,31,96–106] see, e.g., section 6.1.

Non-light driven protein ET that is faster than microseconds is rather unusual, but was shown to occur between heme a and heme a_3 in cytochrome c oxidase. This terminal ET step is coupled to O_2 reduction and proton pumping across the mitochondrial membrane. The experimental approach for rate measurement starts from the mixed-valence complex with the

reduced heme a_3 ligated by CO. A laser flash initiates CO photolysis resulting in a change of heme a_3 redox potential and subsequent ET to heme a. In the early 1990s, using this method with microsecond instrumentation, a 3 μs ET equilibrium was reported.[107,108] But in 2001 optical spectroscopy measurements by Verkhovsky et al. revealed first indications that this reaction is much faster, on the time scale of nanoseconds.[109] This was confirmed a few years later by Pilet et al.[72] and Jasaitis et al.,[110] who, using transient absorption spectroscopy with femtosecond time resolution, reported an ultrafast, nanosecond tunneling rate for heme a → heme a_3 ET. Similarly fast rates were reported subsequently, for the bacterial homologue cytochrome bo_3.[111] These results have sparked a controversy as to whether the ultrafast tunneling is a consequence of unusually small reorganization free energy or high electronic coupling. A number of computational investigations have been carried out in search for an explanation, and I shall discuss them in section 6.2.

At the ultrafast end of biological ET reactions is the 3 ps light-initiated primary charge separation from the special pair P to the bacteriopheophytin H_A in reaction center proteins, measured again by pump−probe femtosecond transient absorption techniques.[71,112] The experimental results have posed a number of serious challenges for theory: (i) the reaction rate increases with decreasing temperature[2] (see also refs 48, 113 and references therein), (ii) the kinetics is multiexponential, (iii) the dependence of rate with respect to driving force is not consistent with the temperature dependence (see ref 112 and references therein), (iv) the reaction could proceed sequentially via a two-step mechanism involving the intermediate B_A^- or directly via superexchange,[114,115] and (v) although there are two quasi-symmetric branches for the reaction (L and M), only the L branch supports ET.

These observations cannot be understood in terms of "standard" ET theories. To address (i), Parson and Warshel[48,113,116] devised a scheme where the ET dynamics is obtained by integrating a stochastic Liouville equation following excitation of the system with a short pulse of light and using MD simulation for model parametrization. Moreover, quantum dynamical schemes were developed that aim at solving the time-dependent Schrödinger equation in a product basis of electronic and nuclear wave functions.[117] To account for (ii) and (iii), Woodbury and co-workers[112] and subsequently Chaudhury et al.,[118] modeled the experimental population decay with the diffusion-reaction equation, which was originally developed by Sumi and Marcus[119] (see also ref 120). To address (iv), Marchi and co-workers extended the spin-boson model to handle three diabatic states that are coupled to a harmonic bath (=protein environment), respectively.[114,115] I shall discuss more recent theoretical developments for the treatment of ultrafast ET reactions in section 5.2.1.

Proteins are not the only biomolecules supporting charge transfer. Since the 1990s a large number of studies have been carried out to characterize and understand hole transport properties of DNA;[44,73,121−125] see recent reviews refs 37 and 38 and references therein. Such processes are of interest because they play a crucial role in the radiative damage of DNA. A remarkable experiment was reported in 2001 by Giese et al. on the kinetics of hole transfer in DNA strands.[121] The authors found that the hole transfer rate between two guanine (G) bases separated by a adenine−thymine (A−T) "bridge" decreases exponentially with the number of A−T base pairs (i.e., the length of the bridge) only up to three A−T base pairs

but exhibits a much weaker distance dependence for longer bridges. This was interpreted as a change of mechanism from superexchange at short distances to hole hopping at longer distances.

Lewis et al. observed a similar change in the distance dependence for hole transfer in stilbene-capped DNA hairpins.[73] For this system the crossover occurred already for bridges comprised of two A−T units. In the latter study, combining femtosecond broadband pump−probe spectroscopy, nanosecond transient absorption spectroscopy, and picosecond fluorescence decay measurements, a ≈2 ps hole transfer rate was reported for tunneling across a single A−T bridge, rivaling primary charge separation in photosynthetic systems (although the hole transfer rate dropped quickly to about 1 ns for longer bridges).

An alternative interpretation of the above results on DNA in terms of the recently suggested flickering resonance mechanism for charge transfer across multiple redox sites is reviewed in section 5.1.2. The fast time scale for charge migration poses a serious challenge to rate theories, however, and has motivated the development of direct charge propagation schemes such as the nonadiabatic molecular dynamics method developed by Elstner and co-workers; see section 5.2.3. Applications of this method to DNA and DNA photolyase are discussed in sections 6.4 and 6.5.

3. ESTABLISHED ET THEORY

Since the seminal work of Marcus in 1956,[126,127] several expressions for the rate of ET reactions have been derived for certain limits using classical, semiclassical, and quantum mechanical formalisms. Excellent reviews on the subject have been written in the 1980s and 1990s,[41−46] to which I refer for a detailed treatment. Here I review the basic concepts of ET theory for readers less acquainted with the theoretical formalism and present the most important rate expressions that are frequently in use and that will be referred to in later sections.

3.1. Diabatic and Adiabatic States

In this review I shall consider electron transfer (ET) reactions between two ionizable groups (e.g., cofactors, amino acids, or DNA bases)

$$RO \rightarrow OR \qquad (1)$$

where RO denotes the donor−acceptor complex with the electron donor in the reduced state (R) and the electron acceptor in the oxidized state (O), and vice versa for OR. The initial ET state RO and the final ET state OR are referred to as states a and b, respectively.

Experimental ET measurements can be induced in different ways. For instance, for intramolecular ET reactions leading to a stable product OR, the reactant state RO can be prepared by a laser flash and the decay of the RO state and/or the rise of the OR state monitored with a probe that is sensitive to the redox state of donor and/or acceptor (pump−probe experiment). Therefore, the natural starting point is to describe states a and b by two charge localized or diabatic electronic states with energies $E_a(\mathbf{R}^N)$ and $E_b(\mathbf{R}^N)$. The dependence of these energies on the nuclear coordinates is made explicit, with $\mathbf{R}^N$ denoting the $3N$ dimensional configuration vector of all N atoms of the system. Diabatic states are reminiscent of the resonance structures of valence bond theory (see, e.g., ref 41 and references therein). They are not unique (they depend on the

experimental preparation of the initial state) and they do not diagonalize the electronic Hamiltonian, which takes the form

$$\mathbb{H} = \begin{pmatrix} E_a & H_{ab} \\ H_{ba} & E_b \end{pmatrix}$$

(2)

in the diabatic representation, where H_{ab} is the electronic coupling matrix element. In eq 2 it is assumed that the diabatic states are orthogonal.[43] Diagonalization of $\mathbb{H}$ gives the adiabatic electronic ground and charge-transfer excited states, E_0 and E_1, respectively:

$$E_{0/1}(\mathbf{R}^N) = \frac{E_a(\mathbf{R}^N) + E_b(\mathbf{R}^N)}{2}$$
$$\pm \frac{1}{2}\sqrt{\Delta E^2(\mathbf{R}^N) + 4|H_{ab}|^2(\mathbf{R}^N)}$$

(3)

where on the right-hand side (RHS) of eq 3 the minus sign is for the ground state and the plus sign for the excited state, and ΔE is the vertical diabatic energy gap:

$$\Delta E(\mathbf{R}^N) = E_b(\mathbf{R}^N) - E_a(\mathbf{R}^N)$$

(4)

Most readers are probably more familiar with the adiabatic states as these are the ones that are usually obtained from electronic structure calculations. E_0 is, e.g., readily obtained from density functional theory (DFT) and E_1, e.g., readily obtained from time-dependent DFT calculations. In fact, often the adiabatic states are computed first and then rotated to obtain the diabatic states. See refs 43 and 128−132 for discussion of various diabatization procedures and the recent work of Migliore, who clarified some of the associated technical details.[133]
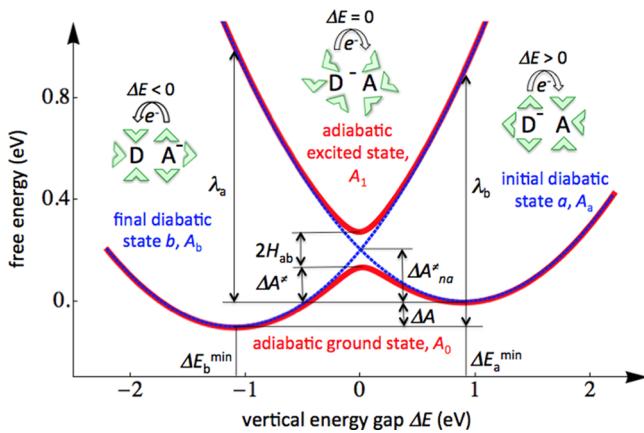
3.2. Established Picture of ET Reactions

To describe ET reactions, one needs to define a suitable reaction coordinate, $\xi(\mathbf{R}^N)$. In solid state problems this coordinate is usually identified with a phonon mode or a combination of phonon modes that promote the ET. For ET reactions between solvated molecules with the solvent treated at the continuum level as done by Marcus, a similar choice can be made by considering the normal modes of the donor–acceptor complex and the dielectric polarization function of the solvent. In modern computer simulations of the energetics of ET reactions also the environment is treated at full atomistic detail. This has the added advantage that ET in highly heterogeneous media, which are difficult to describe with continuum models, can be realistically treated, e.g., protein solutions. In these systems a very large number of modes due to protein residues and solvent couple to ET, which makes the choice of a good reaction coordinate difficult. Moreover, the energy landscape of biomolecules is rather smooth on the thermal energy scale. This means that the modes promoting ET are expected to have a large amplitude and it may no longer be safe to treat them in the harmonic approximation.

In their pioneering works in the early 1980s, Zusman[134] and Warshel[135] addressed this problem by using the diabatic energy gap eq 4 as a reaction coordinate for ET reactions in solutions, $\xi = \Delta E$. The energy gap is a measure for the energetic preference of the electron to be on the donor rather than acceptor site, and as such depends on and is a sensitive measure of the atomic configuration of D and A and the dipolar orientation of the environment. The energy gap coordinate has been successfully used in many early classical MD studies,[136−142] and more recently in DFT-based molecular

dynamics simulations of redox reactions.[143−152] It also stood the test set by more elaborate kinetic theories. For instance, a recent transition path sampling investigation has shown that the energy gap is an excellent reaction coordinate for the ferrous–ferric electron self-exchange reaction.[153]

This brings us to the generally accepted picture of (nonadiabatic) ET reactions, which draws on the concepts of transition state theory of chemical reactions[154] and Landau–Zener theory for electronic transitions.[155,156] At first one defines the two diabatic energies for initial and final states as a function of the energy gap, $E_a(\Delta E)$ and $E_b(\Delta E)$, respectively, as indicated by the pair of curves in blue in Figure 4. (Note, the

Figure 4. Free energy curves for electron transfer between electron donor (D) and acceptor (A) in a dielectric environment (solution or protein). Diabatic free energy curves are shown in blue for $\lambda = \lambda_a = \lambda_b$ = 1 eV, $\Delta A = -0.1$ eV (eqs 11, 12), and adiabatic free energy curves are shown in red for a constant electronic coupling value $H_{ab} \equiv \langle | H_{ab}|^2 \rangle_{\Delta E}^{1/2} = 0.07$ eV (eq 10). See sections 3.5 and 4.2 for definition of quantities indicated. Finite temperature fluctuations and reorganization of the dielectric environment along the ET reaction coordinate are indicated by green chevrons.

corresponding free energy curves are shown in Figure 4 as explained in section 3.3; here I assume for simplicity that energy and free energy curves are similar.) For positive values of ΔE, the configuration of the D−A pair and environment (indicated in green) is such that the ET initial state is more favorable, and vice versa for negative values. ET occurs when thermal fluctuations are large enough that the system, initially at the bottom of the well of the initial state, reaches the point where initial and final states cross, referred to as transition state. This is where the electron can "jump" from the initial to the final diabatic state with a probability given by the Landau–Zener formula.[155,156] After thermal relaxation, the system ends up at the bottom of the final state.

In Figure 4 the pair of adiabatic energy curves are indicated in red. In the bottom of the well for the initial state, the energy gap is typically orders of magnitude larger than electronic coupling, $\Delta E \gg H_{ab}$. Hence, according to eq 3 diabatic and adiabatic states are virtually identical, $E_a \simeq E_0$, $E_b \simeq E_1$, and similarly for the bottom of the final state, $-\Delta E \gg H_{ab}$ and $E_b \simeq E_0$, $E_a \simeq E_1$. However, when the diabatic states are degenerate, $\Delta E = 0$, the ground adiabatic state is lowered to $E_0 = E_a - H_{ab}$ and the energy of the first excited ET state is raised to $E_1 = E_a + H_{ab}$. Moreover, at this point both adiabatic wave functions are delocalized over donor and acceptor (+ and − combination),

whereas the diabatic wave functions remain, per definition, localized on donor and acceptor, respectively.

3.3. ET Free Energy Curves

As mentioned above, the energy landscape of biological systems is smooth compared to the thermal energy and as a consequence of this many nuclear configurations $\mathbf{R}^N$ can produce the same value of the reaction coordinate $\Delta E(\mathbf{R}^N)$. This means entropic effects are important and diabatic and adiabatic energy curves should be replaced by the corresponding free energy curves, also termed Landau free energies A_M:

$$A_M(\Delta E) = -k_B T \ln p_M(\Delta E) + \text{const} \tag{5}$$

$$p_M(\Delta E) = \langle \delta(\Delta E'(\mathbf{R}^N) - \Delta E) \rangle_M \tag{6}$$

where p_M is the probability distribution of ΔE, δ is the Dirac delta function, and the brackets $\langle \cdots \rangle_M$ denote the thermal (Boltzmann) average over configuration space on the diabatic electronic potential energy surfaces $M = a, b$ or the adiabatic potential energy surfaces eq 3, $M = 0, 1$. As in my previous works I use Helmholtz rather than Gibbs free energies, because most of the molecular simulations that will be discussed in later sections are run at constant volume. For aqueous solutions the difference between the two free energies is usually vanishingly small due to their small compressibility.

A pair of diabatic free energy curves are shown in Figure 4 in blue and red, respectively. They are characterized by two important free energies. The vertical difference between the minima of the two curves is the free energy difference or driving force ΔA, which is proportional to the ratio of configurational partition sums for E_a and E_b. Their curvatures are related to the reorganization free energies λ_a and λ_b. λ_a is defined as the free energy required to change the equilibrium configuration for diabatic state a to the equilibrium configuration of diabatic state b while remaining on the diabatic free energy curve a, and similarly for λ_b:

$$\lambda_a = A_a(\Delta E_b^{\min}) - A_a(\Delta E_a^{\min}) \tag{7}$$

$$\lambda_b = A_b(\Delta E_a^{\min}) - A_b(\Delta E_b^{\min}) \tag{8}$$

where $\Delta E_M^{\min}$ is the position of the minimum of the diabatic free energy curve of M. It is thus a measure for the difference in nuclear and electronic polarization between the equilibrium states a and b, which can depend on the electronic state under consideration (hence, λ_a and λ_b instead of a single λ).

An important property of the diabatic free energy curves defined in eq 5 is the linear free energy relation[141]

$$A_b(\Delta E) - A_a(\Delta E) = \Delta E \tag{9}$$

This perhaps surprising identity, equating free energy with energy gaps, can be easily derived by substituting E_b by $\Delta E + E_a$ in the definition of A_b in eq 5 and noting that ΔE is constant due to the δ function in the integrand. It is important to note that eq 9 is exact for *any* distribution $p_M(\Delta E)$ (i.e., not specific to Gaussian distributions) as long as the full equilibrium average over the canonical ensemble is taken. The equivalence of free energy and energy gaps as expressed in eq 9 is solely a consequence of taking the energy gap as reaction coordinate. It is no longer generally true for other reaction coordinates.

Finally, it may be useful to express the adiabatic free energy profiles $A_{0/1}$ in terms of the diabatic free energy profiles $A_{a/b}$. If one assumes that electronic coupling H_{ab} is constant, which is commonly referred to as the Condon approximation,[157] or

depends only on the reaction coordinate ΔE, one can use the linear free energy relation eq 9 to substitute E_b in eq 3 by $\Delta E + E_a$ and write $A_{0/1}$ exactly in terms of the diabatic free energies $A_{a/b}$. However, in general the electronic coupling will depend on all coordinates, not only on ΔE. In this case the thermal averaging is approximated by substituting $|H_{ab}|^2(\mathbf{R}^N)$ in eq 3 by $\langle |H_{ab}|^2 \rangle_{\Delta E}$, where the subscript ΔE denotes thermal averaging over all configurations that give the energy gap ΔE. Then the adiabatic free energy profiles take the form

$$A_{0/1}(\Delta E) \simeq \frac{A_a(\Delta E) + A_b(\Delta E)}{2}$$
$$\pm \frac{1}{2}\sqrt{\Delta E^2 + 4\langle |H_{ab}|^2 \rangle_{\Delta E}} \tag{10}$$

Hence, if one averages separately over diabatic energies and electronic couplings, the adiabatic energies in eq 3 can be simply replaced by the corresponding Landau free energies.

3.4. Linear Response Approximation

In the linear response (LR) or harmonic approximation one assumes that the equilibrium distribution eq 6 is Gaussian for a given diabatic state, e.g., for a, $p_a = \text{const}(\exp[-(\Delta E - \langle \Delta E \rangle_a)^2/(2\sigma_a^2)])$. The free energy curve for a is then parabolic according to eq 5. Insertion of the parabolic free energy curve for a in the linear free-energy relation eq 9 and using the definitions for reorganization free energy eqs 7 and 8 and driving force, one, obtains the following analytic expressions:

$$A_a = \frac{1}{4\lambda}(\Delta E - (\Delta A + \lambda))^2 \tag{11}$$

$$A_b = \frac{1}{4\lambda}(\Delta E - (\Delta A - \lambda))^2 + \Delta A \tag{12}$$

and the following identities hold:

$$\lambda \equiv \lambda_a = \lambda_b \tag{13}$$

$$\Delta E_M \equiv \langle \Delta E \rangle_M = \Delta E_M^{\min} \tag{14}$$

$$\lambda = (\Delta E_a - \Delta E_b)/2 \tag{15}$$

$$\Delta A = (\Delta E_a + \Delta E_b)/2 \tag{16}$$

Thus, in case of Gaussian statistics, which is one crucial assumption in Marcus theory, the diabatic free energies are parabolas with equal reorganization free energies and equal force constants, $k = 1/(2\lambda)$. Furthermore, the reorganization free energy is equal to half of the difference of the mean energy gaps, and the driving force is equal to the average mean energy gaps. These latter identities are very useful for numerical computation of λ and ΔA. Importantly, due to the simple harmonic shape, the ET activation free energy at the crossing point of the two diabatic state parabolas eqs 11 and 12 can be expressed in analytic form and is given by

$$\Delta A_{na}^{\ddagger} = \frac{(\lambda + \Delta A)^2}{4\lambda} \tag{17}$$

where the subscript "na" stands for nonadiabatic (see section 3.5). The activation free energy on the adiabatic curves can be obtained by inserting eqs 11 and 12 in eq 10. One obtains

$$\Delta A^{\ddagger} \simeq A_0(\Delta E = 0) - A_0(\Delta E_a) = \Delta A_{na}^{\ddagger} - \Delta \tag{18}$$

$$\Delta = \langle |H_{ab}|^2 \rangle_{TS}^{1/2}$$

$$+ \frac{\lambda + \Delta A - \sqrt{(\lambda + \Delta A)^2 + 4\langle |H_{ab}|^2 \rangle_a}}{2} \qquad (19)$$

where $\Delta A_{na}^{\ddagger}$ is given by eq 17. The second term on the right-hand side (RHS) of eq 18 (Δ) is a correction that becomes important when electronic coupling is large. The first term on the right-hand side of eq 19 is the difference between adiabatic and diabatic free energy surface at the transition state (TS, $\Delta E = 0$), and the second term is the corresponding difference at the bottom of the initial state. (Note that in deriving eqs 18 and 19 I have assumed that the position of the minima and transition state on the adiabatic free energy profiles are at the same "horizontal" position as on the diabatic free energy profiles, which is not exactly the case but typically a very good approximation.) Equations 15−19 reflect the importance of the average vertical energy gap eq 14 as a key quantity in linear response ET theory, allowing us to quantify simultaneously the thermodynamics (ΔA, eq 16) and together with electronic coupling the kinetics of ET reactions (λ, eq 15; $\Delta A^{\ddagger}$, eq 18).

3.5. ET Rates for Classical Nuclei

In the simplest case, one assumes that the nuclei can be treated as classical (c) particles, as was already implicitly asserted in the treatment of free energies in sections 3.3 and 3.4. This should give a reasonably good description in the limit of high temperature where nuclear quantum effects are expected to be less important. Combining classical transition state theory (TST) in the harmonic approximation[154,157] and Landau−Zener theory (LZT) for the probability of electronic transitions between initial and final diabatic ET states,[155−157] one obtains the following expression for the rate of ET in the donor−acceptor complex:[41,43,157,158]

$$k_c = \kappa_{el}\nu_n \exp\left(-\frac{\Delta A^{\ddagger}}{k_B T}\right) \qquad (20)$$

In eq 20, κ_{el} is the electronic transmission coefficient, ν_n is an effective nuclear frequency along the reaction coordinate, and $\Delta A^{\ddagger}$ is the ET activation free energy eq 18. The electronic transmission coefficient is given by[41]

$$\kappa_{el} = \begin{cases} \dfrac{2P_{LZ}}{1 + P_{LZ}} & \text{if } \Delta A \geq -\lambda \\[2ex] 2P_{LZ}(1 - P_{LZ}) & \text{if } \Delta A < -\lambda \end{cases} \qquad (21)$$

$$P_{LZ} = 1 - \exp(-2\pi\gamma) \qquad (22)$$

$$2\pi\gamma = \frac{\pi^{3/2}\langle |H_{ab}|^2 \rangle_{TS}}{h\nu_n\sqrt{\lambda k_B T}} \qquad (23)$$

where P_{LZ} is the Landau−Zener transition probability for a single crossing event from the initial to the final diabatic state surface, λ is the reorganization free energy given by eq 13 or 15, and h is Planck's constant. The electronic transmission coefficient in eq 21 accounts for multiple uncorrelated passages through the intersection region assuming steady state populations of four intermediate species just before and after the crossing point.[41] Note, the resulting expression differs for normal ($\Delta A \geq -\lambda$) and inverted Marcus regime ($\Delta A < -\lambda$). The nuclear frequency is related to the force constant of the diabatic free energy curves, i.e., to λ, through $2\pi\nu_n = (2\lambda m)^{-1/2}$,

where m is the effective mass for motion along the reaction coordinate. The effective nuclear frequency can be obtained from MD simulation by spectral deconvolution of reorganization free energy (see section 4.2.1 for details).

The LZ transition probability eq 22 was originally derived for crossing between diabatic energy curves with constant electronic coupling. That is, the dependence of electronic coupling on nuclear geometry is disregarded (Condon approximation).[155,156] The thermal averaging over configurations, as indicated by the brackets $\langle ... \rangle_{TS}$ on the RHS of eq 23, is often not explicitly considered.[41,43,158] Here, the effect of finite temperature fluctuations on the LZ transition probability is included in eqs 22 and 23 by replacing the velocity along the reaction coordinate by the thermal average and the electronic coupling matrix element by a thermal average over all transition state configurations at the crossing point region. This is, of course, an approximation to the exact thermal average. However, Troisi, Nitzan, and Ratner showed that, for nonadiabatic ET reactions (see definition below) with fluctuating electronic couplings, the rate constant can be expressed as a series of contributions with decreasing importance, with the leading term coinciding with the standard nonadiabatic expression except that $|H_{ab}|^2$ is replaced by the thermal average $\langle |H_{ab}|^2 \rangle_{TS}$;[159] see eq 24. Hence, the use of $\langle |H_{ab}|^2 \rangle_{TS}$ on the RHS of eq 23 is expected to give a good approximation. See also ref 159 for further discussion.

I would like to emphasize that all assumptions underlying TST and LZT as well as their range of validity carry over to eq 20. One of the key assumptions is that ET is assumed to be slow compared to the slowest mode coupling to ET (see ref 157). If the time scale assumption is not valid, the initial state is no longer Boltzmann populated, which can give rise to a number of complexities such as a distribution of rate constants and nonexponential kinetics. For a discussion of theories that go beyond the time scale separation (i.e., fast ET reactions), I refer the reader to section 5.2. Furthermore, I would like to point out that eq 20 describes ET in the nonadiabatic, adiabatic, and intermediate regimes. These regimes are defined by the adiabaticity parameter $2\pi\gamma$, eq 23. If $2\pi\gamma \ll 1$ the reaction is nonadiabatic (na) and the exponent in eq 22 can be expanded in a Taylor series and truncated after the first order term, giving $P_{LZ} = 2\pi\gamma$ and $\kappa_{el} = 2P_{LZ}$. Insertion of this result into eq 20 gives the nonadiabatic ET rate[157,160]

$$k_{c,na} = \frac{2\pi}{\hbar}\langle |H_{ab}|^2 \rangle_{TS} FC_c \qquad (24)$$

$$FC_c = (4\pi\lambda k_B T)^{-1/2} \exp\left(-\frac{\Delta A_{na}^{\ddagger}}{k_B T}\right) \qquad (25)$$

where FC_c is the classical Franck−Condon factor and $\Delta A_{na}^{\ddagger}$ the activation free energy, eq 17. In this regime the mixing of the initial and final diabatic ET states is weak for any configuration along the reaction coordinate, including the transition state. Thus, when the diabatic states become degenerate in the crossing region, and the change from diabatic state a to b occurs with probability P_{LZ}, the electron jumps abruptly (that is, nonadiabatically) from the donor to the acceptor.

In the opposite limit $2\pi\gamma \gg 1$ the ET is adiabatic (ad) and P_{LZ} and κ_{el} approach unity. The rate expression is the same as for "standard" chemical reactions in the classical transition state approximation; i.e., the prefactor depends only on the frequency along the reaction coordinate:[157]

$$k_{c,ad} = \nu_n \exp\left(-\frac{\Delta A^{\ddagger}}{k_B T}\right) \qquad (26)$$

In this case the mixing of the initial and final diabatic ET states along the reaction coordinate is strong and the reaction occurs on the adiabatic ground state potential energy surface.

As we will see in later sections, for biological ET reactions electronic coupling is typically very small and the vast majority of reactions are nonadiabatic, i.e., described by eq 24. Though there may be cases where the adiabaticity parameter $2\pi\gamma$ is close to unity or larger (as one may expect for ET between stacked DNA base pairs in a low-dielectric medium), in which case the more general eq 20 should be used.

3.6. ET Rates for Quantum Mechanical Nuclei

At low temperature or when ET is strongly coupled to high frequency vibrational motions, nuclear quantum effects become significant. In this case one can relax the restriction to classical nuclear motion and use a quantized rate equation instead of eq 20. Assuming that the nuclear motion coupling to ET can be modeled by a collection of quantized harmonic oscillators, Song and Marcus obtained the following expression for the quantized (q) nonadiabatic ET rate.[161]

$$k_{q,na} = \frac{2\pi}{\hbar}|H_{ab}|^2 FC_q \qquad (27)$$

$$FC_q = \frac{1}{2\pi k_B T}\int_{-\infty}^{+\infty} dR$$

$$\exp\left\{-[1/(2k_B T) + iR/(k_B T)]\Delta A - \frac{2}{\pi\hbar}\int_0^{\infty} d\omega\right.$$

$$\left.\frac{J(\omega)}{\omega^2}\frac{\cosh(\hbar\omega/(2k_B T)) - \cosh(iR\hbar\omega/(k_B T))}{\sinh(\hbar\omega/(2k_B T))}\right\} \qquad (28)$$

where $J(\omega)$ is the spectral density function. The latter can be obtained either from experimental spectra[161] or from computer simulation via the cosine transform of the time correlation function of the vertical energy gap ΔE.[145]

$$J(\omega) = \frac{\omega}{2k_B T}\int_0^{\infty} dt \langle\delta\Delta E(0)\,\delta\Delta E(t)\rangle \cos\omega t \qquad (29)$$

where ΔE is defined in eq 4 and $\delta\Delta E = \Delta E - \langle\Delta E\rangle$. A simpler version of eq 28 was derived longer ago, by quantization of only a single ("effective") mode.[162]

$$k'_{q,na} = \frac{2\pi}{\hbar}|H_{ab}|^2 FC'_q \qquad (30)$$

$$FC'_q = \frac{1}{\hbar\omega}(n + 1/n)^{P/2}I_P(2S(n(n+1))^{1/2})$$

$$\exp[-S(2n+1)] \qquad (31)$$

where $S = \lambda/(\hbar\omega)$, $P = \Delta A/(\hbar\omega)$, $n = 1/[\exp(\hbar\omega/(k_B T)) - 1]$, and I_P is the modified Bessel function of the first kind of order P. In the classical limit $\hbar \to 0$, the quantized FC factors given by eqs 28 and 31 reduce to the classical FC factor eq 25.

4. COMPUTATIONAL APPROACHES FOR ET PARAMETERS

4.1. Electronic Coupling Matrix Element

The electronic coupling matrix element between an electron donor and an electron acceptor is defined by

$$H_{ab} = \langle\Psi_a|\mathcal{H}|\Psi_b\rangle \qquad (32)$$

where Ψ_a and Ψ_b are the N-electron wave functions of the initial and final diabatic states a and b, respectively, $\mathcal{H}$ is the N-electron Hamilton operator for fixed positions of the nuclear coordinates, and N is the total number of electrons of the system including donor, acceptor, and the medium (protein, solvent). Direct calculation of H_{ab} using high-level ab initio methods would of course be the most desirable method. However, there are two problems one faces in practical calculations. First, appropriate high-level ab initio methods for ET, such as multireference configuration interaction (MRCI),[163-165] or N-electron valence state perturbation theory (NEVPT2)[166-168] are due to their unfavorable scaling with particle number still limited to very small donor−acceptor systems of about 10 second-row atoms.[169,170] Second, for long-distance biological ET the sheer smallness of H_{ab} makes a direct calculation impractical. According to estimates by Hopfield and later by Moser and Dutton (see below), one can expect that electronic couplings are on the order of $10^{-1}-10^{-4}$ meV (1−10^{-3} cm^{-1}) for typical donor−acceptor separations found in proteins, 10−20 Å. This is well below basis set convergence and numerical noise of present-day electronic structure calculations.
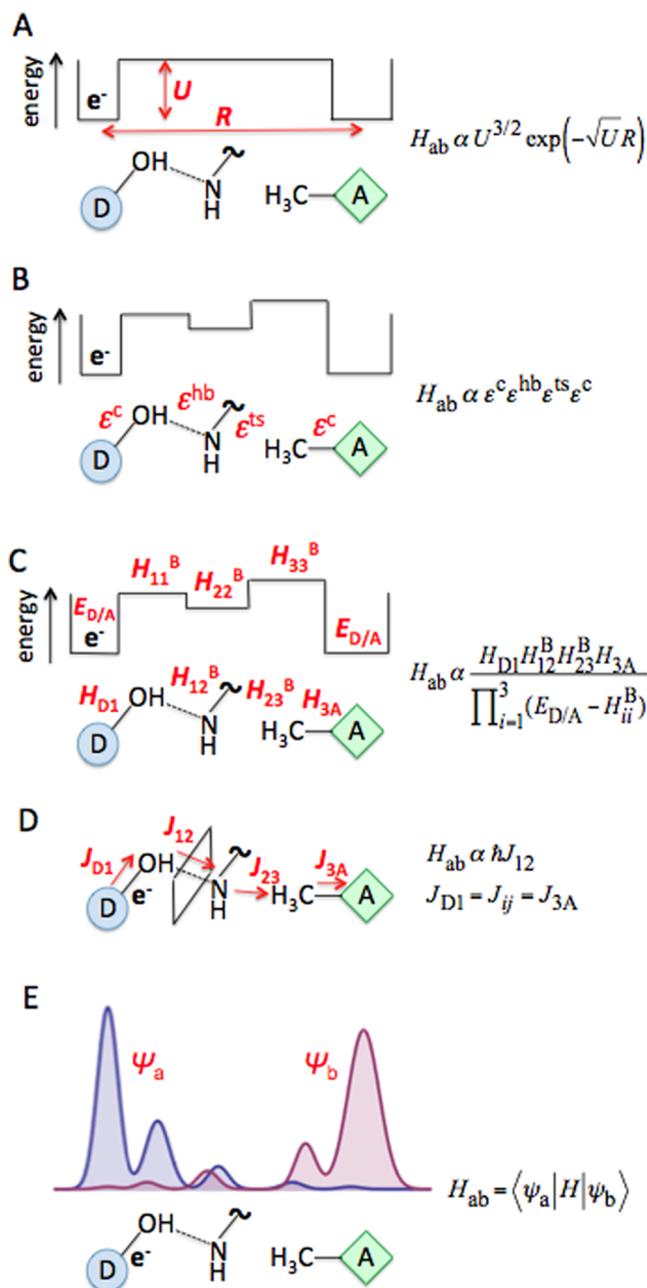
However, a number of indirect methods for estimation of H_{ab} have been developed over the last 30 years, which I briefly review in sections 4.1.1−4.1.5. These are empirical or semiempirical models where a certain tunneling mechanism is assumed a priori and where $\mathcal{H}$ is replaced by a simple but physically motivated model Hamiltonian; see Figure 5A−D. (Semi)empirical models have proved very useful for a qualitative and sometimes semiquantitative understanding of the tunneling process. This is not to say that biological ET is a lost case for more rigorous electronic structure calculations. In many situations ET occurs over smaller donor−acceptor distances (<10 Å) where H_{ab} is significantly larger and where smaller model systems can be employed for computations (schematically shown in Figure 5E). In section 4.1.6 I briefly mention these methods and focus in sections 4.1.7 and 4.1.8 on two approaches that have recently gained much attention, constrained density functional theory (CDFT) and fragment orbital DFT (FODFT).

4.1.1. Packing Density (or Square Barrier) Model. In this simplest possible approach that goes back to the pioneering work of Hopfield,[29] the tunneling medium (protein, solvent, ions, or vacuum) is modeled by a square barrier with an effective barrier height U; see Figure 5A. Solving the one-dimensional Schrödinger equation for this problem, one finds that the coupling matrix element between the initial and final wave function decays exponentially with distance $R - R_0$ with a decay constant β proportional to the barrier height U:

$$H_{ab} = A \exp[-\beta(R - R_0)/2] \qquad (33)$$

$$\beta = 2(Um_{eff})^{1/2} \qquad (34)$$

$$A = wU(Um_{eff})^{1/2} \qquad (35)$$

Figure 5. Electronic coupling matrix elements for biological electron transfer from models of varying complexity (A)−(D) and from direct electronic structure calculations (E). Each method is illustrated by the same donor (D)−bridge−acceptor(A) system with the bridge comprised of an OH, NH, and CH$_3$ group. One-electron energy levels are indicated in black lines. (A) Packing density model, section 4.1.1. (B) Pathway model, section 4.1.2. (C) Superexchange model, section 4.1.4 (D) Tunneling current model, section 4.1.5. (E) Schematic of the initial and final diabatic state wave functions, Ψ_a and Ψ_b, obtained from direct electronic structure calculations, section 4.1.6.

where m_{eff} is the effective mass of the electron and w is the width of the potential well on donor and acceptor (see, e.g., ref 171 for a derivation, expression given there for A contains a typographical error and should be replaced by eq 35). The simple square-barrier tunneling model combined with a suitable decay constant gives a surprisingly good description for biological ET. Moser and Dutton adopted Hopfield's semi-

classical rate expression with a specific choice of reorganization energy and effective temperature.[24,25] They observed that experimental rates, when adjusted to optimal driving force $\Delta A = -\lambda$, can be modeled to good accuracy by the tunneling expression

$$\log k_{ET} = 13 - (1.2 - 0.8\rho)(R - R_0) \quad (36)$$

with values $R_0 = 3.6$ Å and $\rho = 0.76$.[172] In eq 36 ρ is referred to as the packing density of the medium, which is equal to the fraction of the volume between cofactors that is within the united van der Waals radius of intervening atoms, and R_0 is the van der Waals contact distance. Inserting eq 33 in eq 24 and comparing with eq 36, one obtains

$$\beta = \ln 10(1.2 - 0.8\rho) \quad (37)$$

$$A = \left(\frac{10^{13}\hbar}{2\pi}\right)^{1/2} (4\pi\lambda k_B T)^{1/4} \quad (38)$$

which gives numerical values $\beta = 1.39$ Å^{-1} and $A = 22$ meV for $\rho = 0.76$, $\lambda = 0.7$ eV, and $T = 300$ K. Insertion of eq 37 in eq 34 gives the relationship between ρ and the effective tunneling barrier U. The packing density model of Moser and Dutton was shown to capture the physics of the tunneling pathway model, which was published a year earlier[31] (see section 4.1.2), and the equivalence of the electronic coupling factor in the two models was proven in ref 173.

The analysis of experimentally measured ET rates in the framework of eq 36 is subject to a few uncertainties. First, while driving forces are well-known for many ET reactions, reorganization free energies are usually not well-known. Hence, a numerical value for λ often needs to be assumed to correct the measured rate constant to correspond to $\Delta A = -\lambda$. A particularly interesting case in this regard is ET between heme a and heme a_3 in cytochrome c oxidase (cco). The value of λ used to be highly uncertain, and depending on the actual value used, the ET was either very well described or 2−3 orders overestimated by eq 36. I will discuss this reaction in more detail in section 6.2. Second, the distance between donor and acceptor groups is not uniquely defined. For instance, for ET between metal containing π-conjugated rings (e.g., hemes) one could choose the distance between the two metals or between an atom pair of the conjugated ring as a distance metric. This issue has been recently investigated in some detail.[172] Using the shortest edge-to-edge distance between macrocycles as a metric, it was found that most of the measured ET rates, spanning distances from about 4 to 20 Å, fall within an order of magnitude on the straight line described by eq 36.[172]

4.1.2. Pathway Tunneling Model. In the pathway model proposed by Beratan, Onuchic, and Hopfield,[30,31] the atomistic structure of the tunneling medium is recognized; see Figure 5B. Tunneling is assumed to be mediated by consecutive electronic interactions between atoms connecting donor with acceptor. Electronic coupling along a given pathway connecting donor and acceptor is written as a product of a (hypothetical) closest contact term, H_{ab}^0, times an attenuation factor ϵ that is a product of decay factors for consecutive tunneling across covalent bonds (ϵ_i^c), hydrogen bonds (ϵ_j^{hb}), or vacuum (ϵ_k^{ts}, ts for "through space"):

$$H_{ab} = H_{ab}^0 \epsilon \quad (39)$$

$$\epsilon = \prod_i \epsilon_i^c \prod_j \epsilon_j^{hb} \prod_k \epsilon_k^{ts} \tag{40}$$

where $\epsilon_i^c = 0.6$, $\epsilon_j^{hb} = 0.36 \exp[-1.7(r/\text{Å} - 2.8)]$, and $\epsilon_k^{ts} = 0.6 \exp[-1.7(r/\text{Å} - 1.4)]$ and r is the distance between heavy atoms. The through-bond decay parameter ϵ_i^c is a renormalized parameter, drawn from experiment. The through-space decay parameter ϵ_j^{ts} was discussed and downsized in the study of ref 173. I note that the pathway model is an empirical version of the superexchange model which will be discussed in section 4.1.4.

Obviously, there are many paths in a protein that connect donor and acceptor. In practice one prunes the protein to the region between donor and acceptor and/or uses efficient search algorithms to calculate the attenuation factor for a large number of paths. The path with the largest ϵ is then selected as the preferred path. It is worth noting that the pathway model predicts *relative* H_{ab} values, thus allowing for the prediction of relative rates between identical or at least very similar pairs of donor−acceptor cofactors. Estimation of absolute H_{ab} values and rates (or relative H_{ab} values between different pairs of donor−acceptor cofactors) would require specific electronic structure calculations to determine the cofactor-dependent closest contact term H_{ab}^0.

The pathway model predicts that the influence of structure is to cause scatter of rate data about 2 orders of magnitude around any single average exponential decay line. Thus, the influence of protein structure was predicted (and validated experimentally) to cause scatter of about 100-fold around average tunneling decay line. The appeal and popularity of the pathway model is due to the qualitative insight it offers. Likely tunneling paths and ET mediating protein residues can be relatively easily identified[46,51,100,104,174,175] and possibly subjected to mutation studies in investigations aiming to interfere with protein ET.

4.1.3. Packing Density vs Pathway Model. The pathway model recognizes the atomistic structure of the protein, in contrast to the packing density model, where the protein is fully coarse grained and described by just a single parameter ρ (see section 4.1.1). The issue whether an average medium description is adequate and biological ET is purely a matter of donor−acceptor distance (eq 36), or whether proteins have evolved to form specific electron tunneling paths (eq 40 has been hotly debated over the years.[104,174,176] The fact that a large number of free energy optimized biological ET reactions fall within an order of magnitude within a straight exponential decay line for a suitably chosen distance metric (edge-to-edge) is a strong support for the packing density model.[172] On the other hand, if a metal-to-metal distance metric is used, the pathway model can explain resultant anomalous ET rates well assuming orientation dependent electronic couplings.[104] In this respect it is interesting to note that recent electronic structure calculations have indicated strong anisotropy in heme−heme electronic couplings at van der Waals distances[177,178] (see also below), which may persist over longer distances through the protein medium. Further support for the pathway model is the significantly lower exponential distance decay constant reported by Gray and Winkler for beta-strand proteins like azurins ($\beta = 1.1$ Å^{-1}[126]) compared to the average value of $\beta = 1.3-1.4$ Å^{-1}. All of this implies that for long-range biological ET (>10 Å) distance is the single most important parameter, but for a more quantitative understanding atomistic protein structure needs to be considered, too.

What is less clear is whether the packing density model gives a reliable estimate at short distances (3.6−10 Å), where the space between donor and acceptor is mostly empty. It is well-known that "through empty space" electronic coupling does not only depend on distance but, due to the complicated nodal shape of the relevant wave functions, can also be strongly dependent on the orientation of donor and acceptor. Indeed, for ET between closely spaced heme pairs it was shown that electronic coupling can vary by orders of magnitude for different heme−heme orientations at fixed donor−acceptor distance.[177,178] Thus, I expect that eq 36 should be less reliable for shorter distances where the effect of cofactor orientation becomes important. Indeed, recent electronic structure calculations on a bacterial multi-heme protein did not give a simple monoexponential distance decay for short distances, but one that should be described by two decay constants depending on the particular heme−heme orientation.[178] See section 6.3 for further discussion of these calculations.

4.1.4. Superexchange Model. In the superexchange model for electron transfer, it is assumed that electron tunneling between donor and acceptor is mediated by unoccupied atomic orbitals of the medium (also termed "bridge"); see Figure 5C. The bridge is considered to enhance electron tunneling with respect to vacuum, but it does not carry a significant excess electron population at any time. In the limit of weak perturbation, where the difference in energy between unoccupied bridge orbitals (H_{ii}^B) and donor/acceptor frontier orbitals (H_{DD}/H_{AA}) is large compared to electronic couplings (H_{ij}^B), one can derive the following expression for the effective coupling matrix element:[157]

$$H_{ab} = \sum_{i,j=1}^N (H_{Di} - ES_{Di})G_{ij}^B(H_{jA} - ES_{jA}) \tag{41}$$

$$\mathbb{G}^B = (E\mathbb{S}^B - \mathbb{H}^B)^{-1} \tag{42}$$

where S_{Di} and H_{Di} are the overlap and coupling matrix elements, respectively, between the donor orbital and the atomic orbital i of the bridge, G_{ij}^B are the matrix elements of the Green's function of the bridge, $\mathbb{G}^B$, $\mathbb{S}^B$, and $\mathbb{H}^B$ are the overlap and Hamiltonian matrices, respectively, of the bridge, E is the tunneling energy, and N is the number of bridge sites. The dominant term on the RHS of eq 41, G_{1N}^B, can be written in terms of a Dyson expansion. Keeping only the lowest-order term, neglecting the overlap elements in eq 41 and setting the tunneling energy E equal to the energy at the transitions state, $E_{D/A}$, one obtains

$$H_{ab} \approx H_{D1}G_{1N}^B H_{NA} \tag{43}$$

$$G_{1N}^B = \left(\prod_{i=1}^{N-1} \frac{H_{ii+1}^B}{E_{D/A} - H_{ii}^B} \right) \frac{1}{E_{D/A} - H_{NN}^B} \tag{44}$$

Thus, the effective electronic coupling eq 41 is given by a product of nearest-neighbor couplings from the donor along the bridge to the acceptor divided by the energy difference between bridge sites and donor/acceptor at the transition state configuration. For a discussion of overlap effects in the Green's function coupling analysis I refer to ref 179. Equation 44 justifies the pathway model eq 40 where the coupling matrix elements H_{Di}, H_{ii+1}^B, and H_{jA} are approximated by simple distance dependent decay constants ϵ_i. Similar to the pathway model, important amino acids forming the bridge between

donor and acceptor need to be selected. Several methods have been developed for this purpose including artificial intelligence search.[97−99]

Alternatively to ET superexchange, charge transfer could occur via hole transfer (HT) superexchange. In this case a bridge site close to the oxidized acceptor donates an electron to the acceptor and the resultant hole tunnels through occupied bridge states to the donor, in which case both the donor and acceptor are reduced during the tunneling process. A combination of electron and hole tunneling is also possible. Thus, both electron and hole tunneling states should be included when constructing the bridge Hamiltonian. In early studies involving periodic alkane bridges, Beratan and Hopfield showed that both electron and hole mediated propagation could be included without making a Dyson-expansion approximation, and the simple product forms for the decay are captured.[180] Calculations in the literature have employed Hartree−Fock and DFT calculations as well as extended Hückel calculations to approximate the Hamiltonian.[97−99,181] The latter are computationally very efficient and cannot be expected to yield quantitative estimates, but, similar to the pathway model, can capture effects of the protein structure and dynamics.

4.1.5. Method of Tunneling Currents. Like the pathway model, the method of tunneling currents describes the tunneling process at an atomistic resolution. However, instead of empirically searching for the best pathways, explicit electronic structure calculations are carried out and analyzed in the framework of interatomic tunneling currents to identify the atoms mediating the tunneling process; see Figure 5 D. As shown in refs 182 and 183, for a nonstationary electronic state the tunneling current between two atoms m and n is given by

$$J_{mn} = \frac{2}{\hbar} \, \mathrm{Im} \sum_i \sum_j H_{mi,nj} c_{nj} c_{mi}^*$$

(45)

where $H_{mi,nj}$ is the Hamiltonian matrix element in the atomic orbital basis, c_{mi} and c_{nj} are the expansion coefficients of the wave function, and the summation is over all atomic orbitals i on atom m and orbitals j on atom n (see also review ref 184). Importantly, the initial diabatic state of ET theory is a nonstationary state that evolves in time to the final diabatic state and returns to the initial state at the Rabi frequency $H_{ab}/\hbar$ (when the energies of initial and final diabatic states are the same). This establishes the link between J_{mn} and the electronic coupling H_{ab}. The final working expression reads

$$H_{ab} = -\hbar \sum_{m \in S_D} \sum_{n \notin S_D} J_{mn}$$

(46)

where S_D is the volume of space that comprises the donor complex. The expression for the electronic coupling matrix element has been rederived recently using a Golden Rule approach.[185] The tunneling current method has been applied to Ru-modified proteins (reviewed in ref 184), and to the photosynthetic reaction center protein.[186] In the latter study the method was used in combination with molecular configuration sampling to assess the existence of quantum interferences among tunneling routes. More recently, applications were reported to electron tunneling in respiratory complex I[187,188] and a ubiquinol:cytochrome c oxidoreductase model complex.[185]

4.1.6. Direct Electronic Structure Methods. In this section I review electronic structure methods that give direct access to the diabatic state wave functions and the corresponding coupling matrix element, as indicated schematically in Figure 5E. There exist a large number of different approaches. They differ (i) in the way how the diabatic states of ET theory are defined and obtained in practical calculations and (ii) in the level of theory used for the actual calculation. I would like to briefly expand on the first point. The ET diabatic states can be viewed as ground states of two separate noninteracting Hamiltonians, one for the donor and one for the acceptor. At a time t the interaction terms between donor and acceptor are switched on, and the diabatic states are no longer stationary but start to oscillate as governed by the time-dependent Schrödinger equation, causing an electron to transfer from donor to acceptor. While this is a well-defined theoretical concept, the problem in actual calculation is that the former, noninteracting state is an idealized state that is, unlike the stationary adiabatic states of the full interacting Hamiltonian, not uniquely defined. This is similar to the situation where one is free to choose the initial conditions for a time-dependent problem. The issue of initial state preparation is particularly important in the case of low barrier ET as pointed out by Skourtis and Nitzan.[189]

Several physically motivated definitions of diabatic states have been suggested and implemented such as block diagonalization of the adiabatic electronic Hamiltonian,[128,129,190] generalized Mulliken−Hush method (GMH), where the adiabatic states of the interacting Hamiltonian are rotated to obtain charge-localized diabatic states that diagonalize the dipole moment operator,[129,191] fragment charge difference,[192] fragment energy difference,[193] fragment orbital DFT (FODFT),[177,194−199] projection methods,[103,200,201] constrained DFT (CDFT)[52,130,202−207] and frozen density embedding.[208] I refer to publications in the literature[131,132] and references therein for a review of diabatization methods. With regard to the issue of level of theory used, I note that the latter is not always independent from the electronic structure method used for diabatization and ranges from full configuration interaction (FCI) to MRCI, NEVPT2, CASPT2, CDFT, and density functional tight binding (DFTB).
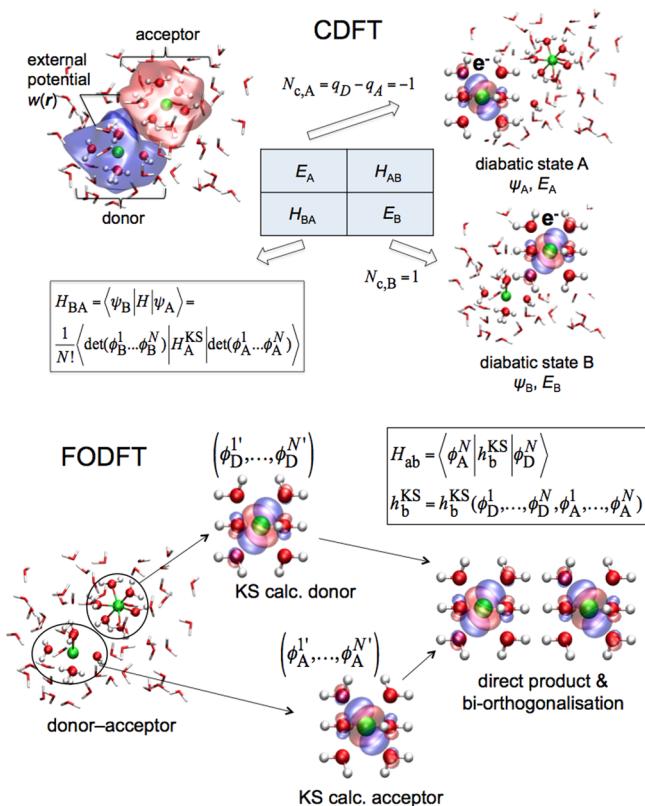
4.1.7. Constrained Density Functional Theory. In the CDFT method developed by Van Voorhis and co-workers[130,202] the diabatic states are obtained from DFT calculations with the excess electron or hole constrained to either the donor (state A) or acceptor (state B), respectively; see Figure 6 for an illustration. This is achieved by adding an external potential term $Vw(\mathbf{r})$ to the usual Kohn−Sham (KS) equations

$$\left(-\frac{1}{2} \nabla_{\mathbf{r}}^2 + v_{\mathrm{KS}}(\mathbf{r}) + Vw(\mathbf{r}) \right) \phi_i(\mathbf{r}) = \epsilon_i \phi_i(\mathbf{r})$$

(47)

and adjusting the height of the potential, V, so that the charge difference between donor and acceptor group is equal to a specified value, e.g., $N_{c,A}$ for state A:

$$\int w(\mathbf{r}) \, \rho(\mathbf{r}) \, \mathrm{d}\mathbf{r} = N_{c,A}$$

(48)

The weight function $w(\mathbf{r})$ is chosen to be negative at the donor site and positive at the acceptor site, which leads to localization of the excess electron at the site with the lower potential (donor if V is positive). In practice one solves the KS equation eq 47 for an initial guess of V (also referred to as undetermined Lagrange multiplier) to obtain the ground state density ρ of the constraint state, which is used for the calculation of the charge constraint on the left-hand side (LHS) of eq 48. If the LHS of

Figure 6. Illustration of CDFT and FODFT methods for the calculation of electronic coupling matrix elements, H_{ab}. In the upper panel, the $Ru^{2+}-Ru^{3+}$ ion pair is shown, solvated in a box of water (Ru, green; O, red; H, white). Two isosurfaces of the external potential $w(\mathbf{r})$ are drawn, one for a negative (blue) and one for a positive value of the weight function w (red). In the first CDFT calculation (charge difference constraint $N_{c,A} = -1$) the excess electron, depicted schematically by the isosurfaces of the highest molecular orbital (HOMO), is localized on the donor, and in the second CDFT calculation ($N_{c,B} = 1$) it is localized on the acceptor. The electronic coupling is obtained from the two sets of Kohn–Sham (KS) orbitals obtained from the two CDFT calculations. In the FODFT scheme in the lower panel, two KS calculations are carried out, one for the donor and one for the acceptor fragments (in a vacuum or in contact with the environment via QM/MM, for instance). After biorthogonalization of the two sets of orbitals, the KS Hamiltonian matrix of the two fragments is built and electronic coupling identified with the matrix element between the HOMOs on donor and acceptor. See sections 4.1.7 and 4.1.8 for further details.

eq 48 is not equal to $N_{c,A}$, one iterates V[202] and solves eq 47 for the new value of V. The iteration in V is repeated until eq 48 is fulfilled. This gives a set of Kohn–Sham orbitals that can be used to form a N-electron determinant for the initial ET state, Ψ_A. In order to obtain the determinant for the final ET state B, Ψ_B, the charge constraint is changed to $N_{c,B}$ (usually $|N_{c,B} - N_{c,A}| = 2$ corresponding to the transfer of one electron from the donor to the acceptor) and the same iterative procedure in V is carried out to localize the electron on the acceptor. In case of electron self-exchange reactions, the magnitude of the final value for V is the same for both states A and B, and differs only in the sign.

The CDFT calculations generate states that are not orthogonal, which is why they are denoted here in capital letters. Thus, the electronic coupling matrix element in the nonorthogonal A, B basis, H'_{AB}, is given by[43,194,205,209]

$$H'_{AB} = \frac{1}{1 - S_{AB}^2}(H_{AB} - S_{AB}H_{BB}) \tag{49}$$

where $H_{AB} = \langle \Psi_A | \mathcal{H}_B^{KS} | \Psi_B \rangle$ and $S_{AB} = \langle \Psi_A | \Psi_B \rangle$. The Hamiltonian in the nonorthogonal basis is in general not Hermitian; therefore $H_{AB} \neq H_{BA}^*$. This problem has been addressed on an ad hoc basis by symmetrizing the two off-diagonal elements.[43,194,205,209] The consequences of nonorthogonality on the two-state ET dynamics has been described in detail in ref 133; see also ref 210. Alternatively, the states Ψ_A and Ψ_B can be transformed to the orthogonal states Ψ_a and Ψ_b by a similarity transformation of the 2×2 Hamiltonian. The off-diagonal element of the resultant Hermitian Hamiltonian, H_{ab}, is then the electronic coupling matrix element between the orthogonal states. See also ref 205 for further details. The difference between H'_{AB} and H_{ab} is often negligibly small.[171,205]

A crucial issue in CDFT calculations is the sensitivity of the results on the functional form chosen for the weight function w. A recent investigation of this issue found that H_{ab} can vary by up to about 30% for a relatively broad range of weight functions and that the sensitivity decreases with increasing donor–acceptor separation distance.[171,205] The most suitable choice appears to be real-space charge definitions according to Hirshfeld or Becke.[130,205,206,211] The performance of CDFT in predicting electronic couplings for databases of π-conjugated organic dimer cations[169] and anions[170] was recently scrutinized by comparison to the results of high-level ab initio calculations (NEVPT2 and SCS-CC2, respectively). It was found that CDFT in combination with a GGA functional (PBE) overestimates the ab initio benchmarks by 38.7%[169] and 60.8%,[170] respectively, due to slightly too large excess charge delocalization over both donor and acceptor fragments (despite the charge constraint being fulfilled, but which acts only on the total electron density). Inclusion of 50% Hartree–Fock exchange in the density functional gave best results for both cations and anions, reducing the errors to 5.3[169] and 8.2%,[170] respectively. This error is negligibly small for all practical purposes. From these studies it was concluded that functionals containing about 50% Hartree–Fock exchange are expected to give the best performance for CDFT electronic coupling calculations on π-conjugated (bio)organic systems. While theory-to-theory benchmarks are extremely useful, the utility of the machinery described above will finally be decided by its linkage to experimental benchmarks. In this regard, calculations on Paddon-Row donor–bridge–acceptor systems,[212] for which experimental coupling estimates are available, are currently being carried out by de la Lande, Elstner, Blumberger, and co-workers.

The CDFT method, at first developed in the present form by Wu and Van Voorhis,[130,202] has been implemented in a number of codes using either localized basis sets (NWChem,[130,202,213] Q-Chem,[214] deMon2k[206,215]), numerical basis functions (CONQUEST),[207,216] or a plane-wave basis set (CPMD[204,205,217]). Recently, de la Lande and co-workers applied CDFT to problems in biological ET. In their initial study the authors attempted to reparametrize the through-space and hydrogen-bond tunneling decay factors that are used in the Beratan–Onuchic pathway model.[206] Refined parameters were suggested that take into account the dependence of the coupling on the orientation of the donor–acceptor pair. An application to ET between methyl amine dehydrogenase and amicyanin followed.[218] More recently, the same authors combined CDFT with QM/MM and computed the coupling

decay for electron tunneling along a polyglycine chain of increasing length.[219] An exponential distance decay was reported down to electronic couplings as small as 10^{-3} meV. The decay constant obtained (1.04 Å^{-1}) was in good agreement with experimental estimates for tunneling through β-strands (1.1 Å^{-1}).[220] The ability to compute such small couplings with a direct electronic structure method is remarkable, albeit somewhat surprising in view of the numerical accuracies that can usually be achieved with atomic basis sets.

I note that CDFT has also been combined with real-time time-dependent density functional theory for the calculation of electron transfer rates coherently coupled to photoexcitations[221] and for simulation of electronic conductance in a molecular wire.[222] Although photoinduced ET processes are not further covered in this review, I would like to summarize very briefly the study of ref 221. In this work CDFT calculations are carried out at first to construct the initial and final diabatic ground states. These states are then propagated by solving the time-dependent Kohn–Sham equations including an external electric field term (with nuclei fixed), and their time-dependent overlap calculated. According to the theory developed in this work, the frequency dependent photoinduced ET rate is proportional to the Fourier transform of the time-dependent overlap times a conventional Franck–Condon factor that can be obtained from CDFT calculations of reorganization free energy and free energy difference. While a first application of this approach targeted ET in inorganic metal clusters, this method may also become a viable tool to model ultrafast photoinduced ET in biological systems, in particular when extended to include nuclear dynamical effects.

4.1.8. Fragment Orbital Density Functional Theory.

There are several implementations of the FODFT method that differ in a number of details with regard to the construction of the orbitals and Hamiltonian and the definition of the coupling matrix element.[177,194−197,199,205] Here I review our own implementation in the CPMD code[199,205] and refer to refs 169 and 170 for a discussion of some of the other implementations. In the FODFT approach denoted "FODFT ($2N − 1$)" in ref 169, the diabatic wave functions are constructed from the orbitals of the isolated (noninteracting) donor (D) and acceptor (A) groups; see Figure 6 for an illustration. Without loss of generality, D and A are assumed to have the same electron number N. For a system with an electron hole the ET is described by $D^+ + A \rightarrow D + A^+$ with total electron number $2N − 1$. Kohn–Sham (KS) DFT calculations are carried out for isolated neutral D and isolated neutral A giving two sets of KS orbitals which are biorthogonalized via Löwdin transformation. The Kohn–Sham Hamiltonian of the combined system, h_b^{KS}, is constructed from the $N − 1$ occupied spin orbitals of D the N occupied spin orbitals of A, respectively. The coupling matrix element for ET is then given by the off-diagonal matrix element

$$H_{ab} = \langle \phi_A^N | h_b^{KS} | \phi_D^N \rangle \tag{50}$$

where ϕ_A^N and ϕ_D^N are the highest occupied molecular orbitals (HOMO or SOMO if N is odd) of A and D, respectively. For a system with an excess electron the ET is described by $D^- + A \rightarrow D + A^-$ with $2N + 1$ electrons. KS calculations are carried out for the isolated anions A^- and D^-, followed by biorthogonalization and construction of h_b^{KS} from the $N + 1$ occupied spin orbitals of D^- and the lowest N occupied spin orbitals of A^-. The coupling matrix element is then given by

$$H_{ab} = \langle \phi_A^{N+1} | h_b^{KS} | \phi_D^{N+1} \rangle \tag{51}$$

where ϕ_A^{N+1} and ϕ_D^{N+1} are the singly occupied molecular orbital (SOMO or HOMO if N odd) of A and D, respectively. It is worth noting that in this scheme the KS-Hamiltonian has the correct number of electrons and that for ET the SOMOs of the donor/acceptor groups with one extra electron are coupled, not the LUMOs of the neutral fragments, in contrast to some other implementations of this method.[195−197]

Equations 50 and 51 seem to be a rather drastic approximation to the exact expression eq 32. Wave functions are replaced by orbitals and the exact Hamiltonian by a KS-Hamiltonian made up of a direct product of one-electron orbitals. These approximations have been recently discussed in some detail in refs 169 and 199. The advantage of FODFT is that the spurious delocalization of an excess electron or hole over donor and acceptor cannot occur as electronic structure calculations are carried out only for the isolated fragments, not for the donor–acceptor pair. The downside of this method is that physical electronic interactions between donor and acceptor are missing, at last in the scheme implemented in refs 199 and 205.

The accuracy of the FODFT approach was benchmarked recently against the same set of high-level ab initio calculations that was used to test the CDFT calculations (see above). It was found that despite the many approximations of the FODFT method, the performance is good, with H_{ab} values for π-conjugated organic cations and anions underestimated by 37.6%[169] respectively 27.9%[170] at the GGA (PBE) level. Furthermore, it was shown that a single scaling factor can correct for this deficiency across a wide range of π-conjugated compounds.[169,170]

The underestimation of couplings in FODFT is most likely due to the neglect of orbital polarization by the electron transfer partner in this method, and possibly also due to inaccuracies of the GGA functional. In a recent study it was shown that FODFT couplings increase by up to a factor of 2 when the percentage of Hartree–Fock exchange was increased from 0% (GGA) to 100%.[223] Thus, while CDFT couplings are expected to be overestimated at the GGA level due to the electron delocalization error and decrease by addition of Hartree–Fock exchange, the exact opposite can be expected for FODFT couplings as a consequence of the missing electronic interaction between the electron transfer partners. A strong advantage of FODFT calculations is that they are robust and straightforward, and they provide a relatively safe and efficient route for reasonably accurate estimation of electronic couplings for large, biological systems. Applications of this method to heme–heme couplings are discussed in section 6.3.

4.2. Free Energies for Electron Transfer

In sections 3.3 and 3.4 the free energy profiles for ET reactions were introduced as well as the linear response approximation that leads to Marcus theory. In this section I review the free energies in more detail and introduce two types of reorganization free energies in addition to the definition given in eqs 7 and 8. I also reexamine the validity of the linear response approximation and review recent extensions of it that account for nonlinear response effects. At the end of this section a summary of state-of-the-art computational methods is given for the calculation of ET free energies.

4.2.1. Driving Force and Reorganization Free Energy.

The classical reaction free energy or driving force of reaction eq

1, ΔA, is given by the ratio of classical partition sums over the potential energy surfaces of adiabatic states 0/1 or diabatic states a/b (the difference is negligibly small for small coupling values). Expressing the Boltzmann factor in the partition sums by the vertical energy gap ΔE (eq 4, one obtains[224]

$$\Delta A = A_b - A_a = -k_B T \ln\langle \exp[-\Delta E/(k_B T)]\rangle_a \tag{52}$$

$$= k_B T \ln\langle \exp[\Delta E/(k_B T)]\rangle_b \tag{53}$$

where the brackets in eqs 52 and 53, $\langle \cdots \rangle_M$, denote the canonical average evaluated for the potential energy of state M, M = a, b.

Reorganization free energy has been defined in eqs 7 and 8 as the free energy required changes the nuclear configuration from the minimum of the initial state to the minimum of the final state. Two more definitions for reorganization free energies are in use that I distinguish from the ones defined in eqs 7 and 8 by subscripts "st" and "var", respectively. The former is defined to be equal to the difference in the mean energy gaps of the two states

$$\lambda^{st} = (\langle \Delta E \rangle_a - \langle \Delta E \rangle_b)/2 \tag{54}$$

and can be directly obtained from experiments as the difference of absorption and emission peaks (=Stokes shift, hence "st"). The latter is defined in terms of the thermal fluctuations of ΔE

$$\lambda_a^{var} = \frac{\sigma_a^2}{2k_B T} \tag{55}$$

$$\lambda_b^{var} = \frac{\sigma_b^2}{2k_B T} \tag{56}$$

where σ_M^2 is the variance ("var")

$$\sigma_M^2 = \langle (\Delta E - \langle \Delta E \rangle_M)^2 \rangle_M \tag{57}$$

λ_M^{var} can be obtained from the inhomogeneous broadening of the absorption or emission peak. At first sight, the different definitions for reorganization free energy do not seem to have much in common. However, in the linear response or Gaussian approximation (see section 3.4) all definitions for reorganization free energies are equivalent as a consequence of the linear free energy relation eq 9.

$$\lambda \equiv \lambda_a = \lambda_b = \lambda^{st} = \lambda_a^{var} = \lambda_b^{var} \tag{58}$$

The definition of reorganization free energy in terms of the gap fluctuations, eqs 55 and 56, is very useful because it allows one to understand this property in terms of contributions from different nuclear modes. To this end one defines the time-correlation function of the energy gap

$$c_M(t) = \langle \delta\Delta E(0)\, \delta\Delta E(t) \rangle_M \tag{59}$$

where $\delta\Delta E(t) = \Delta E(t) - \langle \Delta E \rangle_M$, and carries out a cosine transform to obtain the spectral density function $J_M(\omega)$

$$\frac{J_M(\omega)}{\omega} = \frac{1}{2k_B T} \int_0^\infty dt\, c_M(t)\cos\omega t \tag{60}$$

Integration of the inverse transform in frequency space gives at $t = 0$
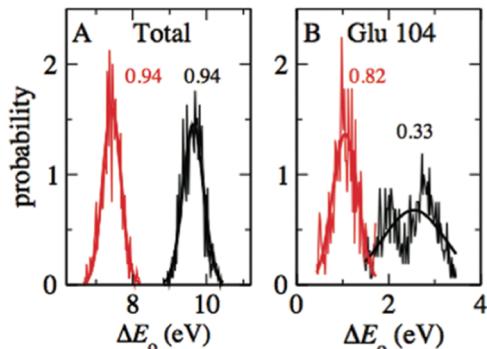
$$c_M(0) = \frac{4k_B T}{\pi} \int_0^\infty d\omega\, \frac{J_M(\omega)}{\omega} \tag{61}$$

Since $c_M(0) = \langle \delta\Delta E^2 \rangle_M = \sigma_M^2$, one obtains by comparison to eqs 55 and 56

$$\lambda_M^{var} = \frac{2}{\pi} \int_0^\infty d\omega\, \frac{J_M(\omega)}{\omega} \tag{62}$$

Thus, reorganization free energy can be resolved and understood in terms of spectral components by integration over the corresponding spectral density.

4.2.2. Deviations from Linear Response. The LR assumption is often found to give a good approximation. Experimental evidence for this comes from band-shape analysis of individual vibronic lines in the optical absorption and emission spectrum of donor–acceptor complexes; see, e.g., ref 225 and references therein. Moreover, the energy gap law, that is the parabolic dependence of the ET rate with respect to reorganization free energy, $\ln k_{c,na} \propto -(\lambda + \Delta A)^2$ (from eqs 24, 25, and 17) is a direct consequence of the LR assumption, and has been observed for a series of aromatic donor–bridge–acceptor compounds[226] (serving as the first experimental verification of Marcus' inverted regime), as well as for proteins.[227] Deviations from the energy gap law in the inverted region are often attributed to nuclear quantum effects.[225] Evidence for LR behavior also comes from MD simulation studies of ET between transition metal ions in aqueous solution,[139,198,204,228] and in native and Ru-modified cytochromes;[105,106,229−231] see, e.g., Figure 7A.

Figure 7. (A) Probability distribution for the total outer-sphere energy gap, ΔE_o, for ET in cytochrome c-His33Ru(NH$_3$)$_5$ (cca, see Figure 19A for protein structure). ET Fe^{2+} → Ru^{3+} in black and Ru^{2+} → Fe^{3+} in red. (B) Probability distribution for the contribution of the amino acid Glu104 to the total outer-sphere energy gap (see Figure 20A for illustration of the response). Notice that the total energy gaps in (A) are well approximated by Gaussian distributions, whereas the energy gap contributions by Glu104 in (B) are non-Gaussian. Reprinted from ref 106. Copyright 2010 American Chemical Society.

For large condensed phase systems like protein solutions the Gaussian statistics can be understood in terms of the central limit theorem. That is, a large number of uncorrelated and arbitrary distributions of the electrostatic potential at the redox site due to the thermal fluctuations of charged or dipolar molecules or molecular fragments (here side chains, backbone, and the solvent) result in an overall Gaussian distribution. Clearly, in molecular systems fluctuations are not strictly uncorrelated but for large systems like protein solutions the distances between many of the charged or dipolar groups are large and may be considered as uncorrelated to a first approximation. Interestingly, the distribution of the energy gap due to single amino acid residues can be profoundly non-

Gaussian as reported for certain amino acids in Ru-labeled cytochromes; see Figure 7B. It is the averaging over many non-Gaussian distributions from protein residues that gives the overall Gaussian distribution shown in Figure 7A.
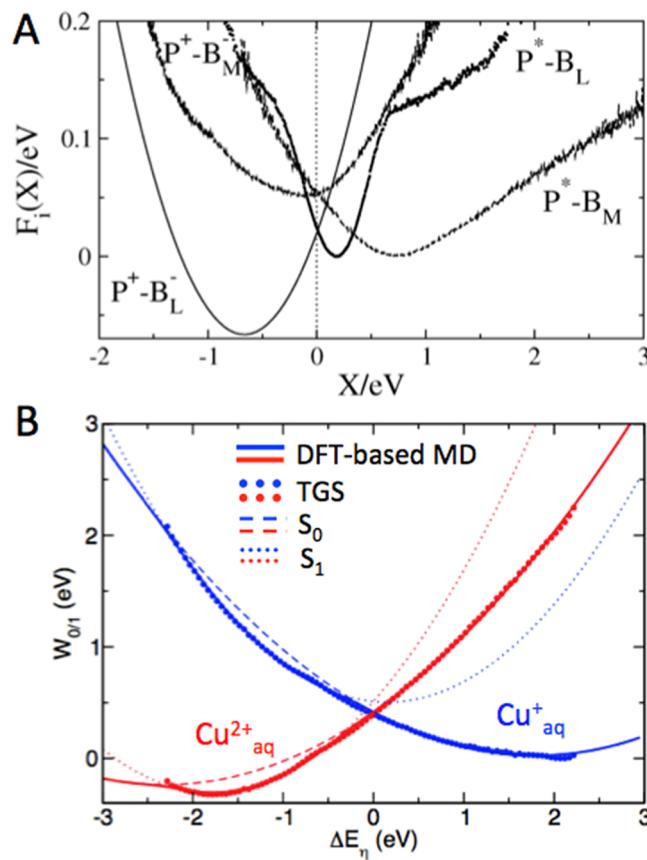
Deviations from LR have been observed and typically manifest themselves in different curvatures of the free energy wells. So far, this has been attributed to three different causes: (i) a strong change in the electronic polarizability of the solute with charge state;[225,232−234] (ii) very strong changes in the solvation of the ET reactant and product species,[136−138] e.g., when ET is coupled to a change in coordination numbers or to chemical bond break,[146,148,152] the latter is usually referred to as "inner-sphere mechanism"; and (iii) fast ET in combination with strong nonergodic effects.[232−234] I note that standard Marcus theory was developed for "outer-sphere" ET reactions, where the chemical bonding of the oxidized/reduced species remains intact during ET. Therefore, it is not expected to hold for case (ii). Moreover, assuming a Boltzmann distribution of states, it is not expected to hold for case (iii).

The first case (i) is typically observed for a solute that is neutral and apolar in one ET state and charged in the other.[140] An example in biology is the primary charge separation reaction in photosynthetic reaction center proteins, for which distinctly non-Gaussian free energy profiles were reported when the special pair is described with an electronically polarizable (fluctuating charge) model;[232−234] see Figure 8A. In this case the curves could be fit to an extension of the standard Gaussian picture allowing for asymmetry between the two diabatic curves by introducing different electronic polarizabilities in initial and final ET states (Q-model[225,235]).

As an example for the second case, I mention the strong nonlinear response reported for the Cu^+/Cu^{2+} redox reaction in aqueous solution as obtained from density functional based MD simulation (DFMD); see Figure 8B.[148] The curvatures at the bottom of free energy profiles for the monovalent and divalent ions are very different and are interpreted as arising from two different types of solvent reorganization in response to oxidation: a chemical response in the low free energy region for Cu^+ (high free energy region for Cu^{2+}), leading to a change in the first shell coordination number from an equilibrium value of 2 for Cu^+ to the equilibrium value of 5 for Cu^{2+}, and a standard dielectric response of higher solvation shells in the low free energy region of Cu^{2+} (high free energy region for Cu^+). Even larger nonlinearities have been obtained for the Ag/Ag^+ oxidation in water, again using DFMD simulations.[152] Also in this case first shell coordination changes dramatically upon oxidation.

To account for these observations (which could not be explained with the Q-model[152]), Vuilleumier and co-workers have extended the Marcus picture for reactions with large solvation changes and developed a 2-Gaussian and a non-Gaussian solvation model.[152] In the 2-Gaussian model the solvent response is formulated in terms of two separate Gaussian solvation states S_0 and S_1 with reorganization free energies λ_{S_0}, λ_{S_1} and free energy differences between initial and final ET states, ΔA_{S_0}, ΔA_{S_1}. Each solvation state gives rise to a separate pair of diabatic free energies

$$W_{S,0}(\epsilon) = \frac{1}{4\lambda_S}(\epsilon - (\Delta A_S + \lambda_S))^2 + A_{S,0}$$
$$+ \frac{k_B T}{2} \ln 4\pi k_B T \lambda_S \quad (63)$$

Figure 8. (A) Non-Gaussian diabatic free energy curves for primary charge separation in the special pair along the L and M branches. Reprinted with permission from ref 234. Copyright 2010 Royal Society of Chemistry. (B) Non-Gaussian diabatic free energy curves for the redox reaction $Cu^+ \rightarrow Cu^{2+} + e^-$ in aqueous solution. Adapted from ref 152. Copyright 2012 American Chemical Society. In panel B TGS stands for the two-Gaussian solvation model, eqs 65 and 66, with solvation states S_0 and S_1, eqs 63 and 64. ΔE_η (denoted ϵ in the main text) is the vertical electron removal energy, eq 70.

$$W_{S,1}(\epsilon) = \frac{1}{4\lambda_S}(\epsilon - (\Delta A_S - \lambda_S))^2 + A_{S,0} + \Delta A_S$$
$$+ \frac{k_B T}{2} \ln 4\pi k_B T \lambda_S \quad (64)$$

where the subscript S takes values $S = S_0$, S_1 and the second subscript of W denotes the initial (0) and final (1) diabatic states. The resultant total diabatic free energies are given by

$$W_0(\epsilon) = -k_B T \ln[\exp(-W_{S_0,0}/(k_B T))$$
$$+ \exp(-W_{S_1,0}/(k_B T))] \quad (65)$$

$$W_1(\epsilon) = -k_B T \ln[\exp(-W_{S_0,1}/(k_B T))$$
$$+ \exp(-W_{S_1,1}/(k_B T))] \quad (66)$$

where $W_0(\epsilon)$ corresponds to $A_a(\Delta E)$ in our notation and $W_1(\epsilon)$ to $A_b(\Delta E)$. Note that the profiles for the two solvent states eqs 63 and 64 and the total free energy profiles in eqs 65 and 66 obey the linear free energy relation eq 9, the latter only assuming a canonical equilibrium distribution. The model has five fit parameters, λ_{S_0}, λ_{S_1}, ΔA_{S_0}, ΔA_{S_1}, and a free energy shift to constrain the free energy difference to ΔA.

The profiles eqs 65 and 66 were found to fit very well the non-Gaussian free energy curves obtained from the DFMD data for the Cu^+/Cu^{2+} and Ag/Ag^+ aqueous redox couples; see Figure 8B.[152] In case of the Cu couple, the Gaussian fluctuations of S_0 describe the change in the first shell coordination number in the low free energy region of Cu^+, whereas the Gaussian fluctuations of S_1 take over in the low free energy region of Cu^{2+} to describe the standard dielectric response of higher solvation shells. The mixing region between the two different solvation regimes at around $\Delta E = 0$ is of sigmoidal shape due to the particular functional form of eqs 65 and 66. The excellent fit of the data is a confirmation that the solvent response to oxidation/reduction of these ions can indeed be thought of as two distinct solvation responses, each of which is Gaussian but with different parameters, resulting in an overall non-Gaussian solvent response.

The situation described here for aqueous transition metal ions with flexible coordination spheres is probably less relevant for electron transporting proteins, where transition metals are incorporated in rather rigid molecular frames (hemes, cubanes) that hardly change bond lengths, let alone coordination numbers when oxidized or reduced. However, nonlinear response of this kind may occur at the catalytic termini of ET chains when ET is coupled to substrate binding, chemical reaction steps, or product unbinding.

A third possible source for non-Gaussian profiles is the nonergodicity of fast ET reactions.[36,232−234] Here the thermal averaging should be carried out only over the part of phase space that can be visited on the time scale of the reaction; see section 5.2.1 for details. Taking again the example of the primary charge separation, rather different shapes were found for the free energy curves, depending on whether they were averaged over the computationally accessible nanosecond time scale or over the relevant picosecond time scale of the actual reaction.[232]

4.2.3. All-QM, QM/MM, and QM + MM Implementations.
The key quantity for calculation of ET free energies is the vertical energy gap ΔE, defined in eq 4. All what is required, is to sample ΔE in the initial and final ET states and insert in either eq 52, 53, or 16 to obtain the driving force ΔA, and in eq 5 to obtain diabatic free energy curves, and thereby reorganization free energy (eq 7,8, or 15) and activation free energies (eq 17). Accurate calculation of these thermal averages is a challenge, however. The fluctuations of the energy gap, essentially being proportional to the fluctuations of the average electrostatic potential at the active site, can be very large due to wide amplitude motion of charged/dipolar protein residues surrounding the active site and can span many orders of magnitude in frequency space due to the different time scales of protein/domain motions.

To improve the accuracy of the sampling procedure, simulations may be carried out for intermediate states bridging initial and final states. The usual formulas for thermodynamic integration/free energy perturbation can then be used to compute the driving force, and standard unbiasing methods can be used to obtain the diabatic free energy profiles. To this end, several computational schemes have been developed for calculation of energy gaps for biological ET. While most of them employ classical MD simulations to sample the protein configurations and use snapshots from these simulations to compute the energy gap, their major difference is the level of theory used for the energy gap calculation.

At the most rigorous level, one may employ all-QM calculations using linear or low scaling DFT as was done in a study on ferredoxin.[236] This treatment circumvents the problems that are introduced by an interface between a high-level and a low-level description of the system as is the case in quantum mechanics/molecular mechanics calculations (QM/MM, e.g., convergence with QM system size, electron spill-out, termination of QM region, etc.). Moreover, electronic polarizability, which is crucial for more quantitative estimates for reorganization free energy, is included in a most realistic way. However, the all-QM treatment means that the system is potentially prone to spurious charge transfer between ionizable protein residues and redox active cofactors due to the electron self-interaction error of GGA functionals. This can be a potential problem especially when the protein contains amino acids with relatively low ionization potentials (tyrosine, tryptophan, and cysteine), that are similar in magnitude to the electron affinity of the redox active cofactors. Functionals containing a certain percentage of Hartree−Fock exchange (hybrid functionals) and/or range-separated hybrids may cure this deficiency, but these functionals are computationally more expensive.

In QM/MM schemes the problem of spurious charge transfer is avoided simply by treating only the redox active cofactor with explicit electronic structure methods and the rest of the protein with a classical force field. A possible scheme for the calculation of ΔE at the level of QM/MM is shown in Figure 9. In the first step (top left) the electron donating
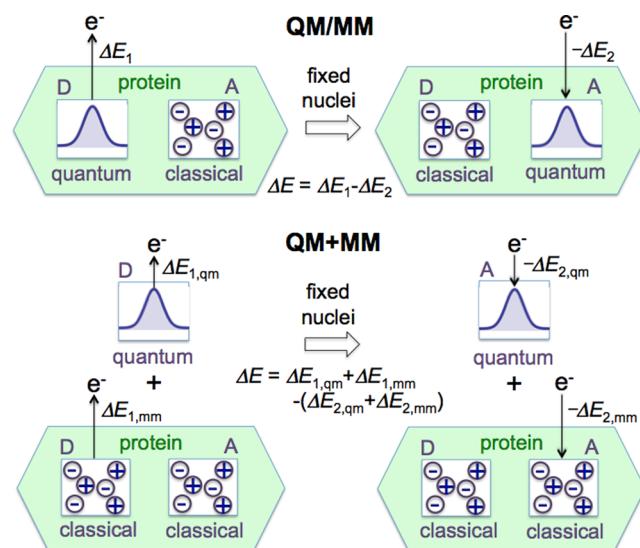
Figure 9. QM/MM and QM + MM schemes for calculation of the vertical electron transfer energy, ΔE. See section 4.2.3 for details.

cofactor (D) is treated at the QM level and the electron accepting cofactor (A) as well as the protein and solvent is treated at the classical force field level. The vertical ionization energy of D, ΔE_1, is obtained as the energy difference between two single-point calculations at the same nuclear geometry, one for D in the oxidized state and one for D in the reduced state, while A remains in the oxidized state in both calculations. In the second step (top right, Figure 9) the nuclear positions remain the same as in step 1 but the QM region changes. D is now described with a classical force field and A at the QM level. The electron removed from D in step 1 is now inserted in A and the electron affinity is calculated as the energy difference of two

single-point calculations with A in the reduced and oxidized state, respectively, while D remains in the oxidized state in both calculations. The difference between ionization energy of D and electron affinity of A is the vertical energy gap.

QM/MM calculations of driving force and reorganization free energy, based on the above computational scheme, were reported for Ru-modified cytochromes[105,230] and catalases[237] and for the redox potential of azurin.[238] Similar calculations were carried out by Ryde and co-workers to determine reorganization energies for multi copper oxidases employing either a mechanical or an electrostatic QM/MM embedding scheme.[239] More recently, a double-QM/MM scheme has been reported, where both D and A are treated at the QM level at the same time.[240] This allows one to compute the ET energy directly as the energy difference between final and initial states without going through the doubly oxidized states of the above (single-)QM/MM method (final state of step 1 and initial state of step 2). A first application to the electron exchange between Fe and Ru cations in liquid water was promising, and the method should be well suited for future calculations of ET energy gaps between protein cofactors. Distinct from the above approaches is the QM/MM approach developed by Yang and co-workers, who combined the theory of fractional electron numbers with the minimum free energy path method (FNE-MFEP) to compute ET free energies.[241−244] Applications to aqueous redox systems including Ru cations, flavins, and most recently azurin were rather successful.

While QM/MM calculations significantly reduce the computational effort with respect to all-QM approaches, they are still relatively expensive. A number of alternatives have been proposed over the years to reduce the cost of the QM calculations, including frozen density functional theory coupled to MD with a classical reference potential,[245] the perturbed matrix method avoiding self-consistent iteration of the electronic orbitals at each MD time step,[246,247] self-consistent charge density functional tight-binding,[248−250] and decoupling between QM and MM calculations (QM + MM).[105] In the latter method, illustrated in Figure 9, the total ionization energy ΔE_1 is divided into an inner sphere contribution, $\Delta E_{1,qm}$, due to the redox active cofactor, and an outer sphere contribution, $\Delta E_{1,mm}$, due to protein and solvent. The former is obtained from a QM gas-phase model of the inner sphere, and the latter is obtained from a classical force field description of the outer and inner spheres. A similar division is done for the calculation of the electron affinity of A, ΔE_2. As in the QM/MM scheme, the total energy gap is obtained from the difference between ionization energy of D and electron affinity of A.

In contrast to QM/MM, in QM + MM the calculations for the QM and MM parts are decoupled, assuming additivity between the inner and outer spheres. This is expected to give a good approximation when the cofactors are relatively rigid and correlations between protein and cofactor fluctuations can, to a first approximation, be ignored. In this case the calculation of the inner-sphere contribution to λ by thermal averaging at the QM level may be replaced by the usual four-point QM scheme[251] and the inner-sphere contribution to ΔA may be replaced by the more standard quantum chemical approach, i.e., single point energy and frequency calculations. In the special case where donor and acceptor are chemically identical (e.g., chain of FeS clusters or bis-His coordinated c-hemes), the inner-sphere contribution to ΔA vanishes at this level of theory and the driving force is due only to the outer sphere, i.e., protein and water.

Due to their simplicity and efficiency, QM + MM-type investigations have been the most common computational approach, not only for the modeling of biological ET but also for other electronic processes such as excitation energy transfer. Examples include biological ET in native and Ru-modified monoheme cytochromes,[105,106,229,252] azurin,[253] cytochrome c oxidase,[231] deca-heme proteins,[178,254] and the photosynthetic reaction center.[114,115,232−234,255] Relatively good agreement with QM/MM results were reported, where available.[105]

5. RECENT THEORETICAL DEVELOPMENTS
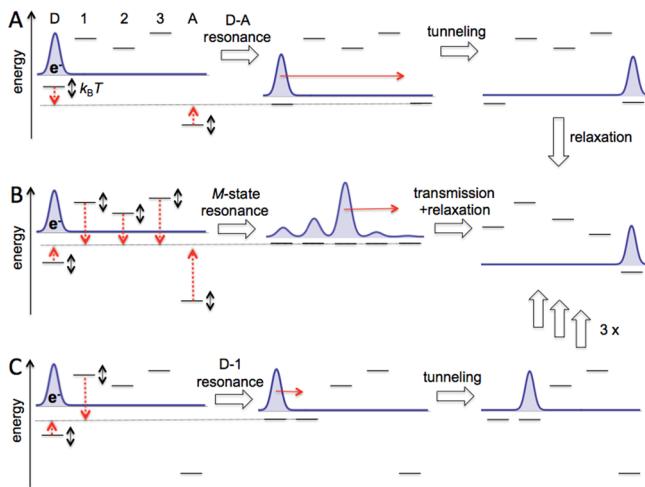
5.1. Multistate Biological ET

In sections 3 and 4 single step electron tunneling between a donor and an acceptor was considered. The tunneling time tables in proteins compiled by Moser and Dutton and Winkler and Gray suggest that single step tunneling gives functional, millisecond free energy optimized ET rates up to tunneling distances of ≈20 Å[50,56] (a more precise value would depend on many details including the distance metric used). On the other hand, it is well-known that protein structures support ET over significantly longer distances, e.g., documented for the complexes of the respiratory chain,[6,176] hydrogenases,[11] carbon monoxide-dehydrogenases[256] (FeS clusters), and the multi-heme cytochromes involved in extracellular respiration (c-type hemes).[8,257]

The solution for very long ranged ET in biology is to arrange redox active cofactors in chains at close cofactor spacings of typically 10−15 Å, enabling consecutive electron tunneling steps over shorter distances (=hopping). In addition to metal containing cofactors, ionizable protein residues such as tryptophan, tyrosine, or cysteines could act as an electron relay, e.g., in ribonucleotide reductase, photosystem II, DNA photolyase, and cytochrome c/cytochrome c peroxidase; see ref 56 and references therein. Moreover, long-ranged charge transfer has also been observed between low potential DNA bases (typically guanines) bridged by intervening high potential base pairs (typically adenines).[73,121]

Over the years several theoretical models have been suggested to describe long-range ET across a chain of ionizable molecular subunits including superexchange (SE),[29] charge hopping, variable-range hopping,[258] hopping maps,[259] and, most recently, the flickering resonance mechanism[35] (FR). In this section the two most common models, SE (section 5.1.1) and charge hopping (section 5.1.3), will be described following the book of Nitzan.[157] Then the FR model developed by Beratan, Skourtis, and co-workers is reviewed and reexamined in some detail in section 5.1.2. The FR model may be viewed as in between the SE and the hopping model, which is why the SE model is discussed first, followed by FR and hopping; see Figure 10 for a schematic illustration. At the end of this section (section 5.1.5) the recently established concept of hopping maps is briefly described.

5.1.1. Superexchange Model. The superexchange (SE) model has been introduced in section 4.1.4 and is illustrated schematically in Figure 10 A. Thermal fluctuations bring donor and acceptor levels into degeneracy (resonance) causing the electron to tunnel along the bridge from donor to acceptor. Nuclear relaxation following the ET stabilizes the electron on the acceptor site. Importantly, during the tunneling process the electron does not populate the bridge. The latter merely lowers the tunneling barrier, or equivalently increases the electronic coupling between donor and acceptor.

Figure 10. (A) Superexchange (SE), (B) flickering resonance (FR), and (C) hopping models for ET along a chain of $M = 5$ redox active molecular sites (e.g., cofactors, DNA base pairs). The first site is the electron donor (D), the last site is the acceptor (A), and there are three bridge sites (1, 2, 3) between D and A. One-electron energy levels are drawn in black lines for each site. The excess electron is indicated by a Gaussian function, initially localized at site D. In the SE model (A), thermal fluctuations bring D and A levels into resonance, followed by tunneling from D to A. The bridge sites remain off-resonant; they only enhance tunneling but are not significantly occupied by the tunneling electron at any time. In the FR model (B) all five levels are assumed to be in resonance before the electron transfers to the acceptor. The bridge sites become partially occupied by the tunneling electron. In the hopping model (C), the donor D and the nearest neighbor bridge site 1 get into resonance, followed by electron tunneling from D to 1. This step is repeated three times until the electron has made four consecutive hops to reach A.

The SE mechanism relies on the assumption that the gap between highest occupied/lowest unoccupied electronic energy levels of the bridge units (here the chain of redox active molecular units between donor and acceptor) and the redox active levels of donor and acceptor is large compared to electronic coupling between donor/acceptor and the bridge.[157] Assuming that in eqs 43 and 44 all electronic couplings are the same, $H_{D1} = H_{ii+1}^B = H_{NA}$, and that all bridge energy levels H_{ii}^B are the same, one obtains[157]

$$|H_{ab}|^2 = V^2 \left(\frac{V}{\Delta E_{D/A} - \Delta E_B} \right)^{2N} = V^2 \exp[-\beta(R - \Delta R)] \tag{67}$$

$$\beta = \frac{2}{\Delta R} \ln \left| \frac{\Delta E_{D/A} - \Delta E_B}{V} \right| \tag{68}$$

where $\Delta R = R/(N + 1)$ is the spacing between the sites, assumed to be equidistant. Hence, for a periodic bridge the effective coupling matrix element eq 67 is found to drop exponentially with donor–acceptor distance with a decay constant determined by the site–site spacing ΔR and the ratio of energy spacing between D/A and bridge levels, $\Delta E_{D/A} - \Delta E_b$, and the site–site electronic coupling V. To facilitate comparison to the results of the following sections, the absolute electronic potential energies in eq 44, $E_{D/A}$ and H_{ii}^B, are replaced in eqs 67 and 68 by the electron removal energy of the donor at the transition state configuration, $\Delta E_{D/A}$, and the electron removal energy of the bridge, ΔE_b, respectively. The gap energy

$\Delta E_{D/A} - \Delta E_b$ can be expressed in terms of ET free energies and reorganization free energy and is given by eq 77. The electronic coupling matrix element between sites, H_{ii+1}^B, has been replaced by the root-mean-square fluctuations $V = \langle |H_{ii+1}^B|^2 \rangle^{1/2}$ to take into account thermal effects.

The superexchange ET rate for a periodic bridge, k_{SE}, is then given by the usual nonadiabatic ET rate eq 24 using expression eq 67 for $|H_{ab}|^2$:

$$k_{SE}(R) = \frac{2\pi}{\hbar} \frac{V^2}{\sqrt{4\pi\lambda k_B T}} \exp[-\beta(R - \Delta R)]$$
$$\exp\left[-\frac{(\Delta A + \lambda)^2}{4\lambda k_B T} \right] \tag{69}$$
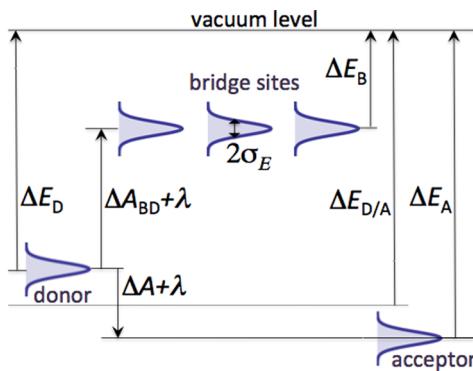
5.1.2. Flickering Resonance Model. An interesting situation arises when ET occurs along a chain of redox sites where donor, acceptor, and bridge levels are similar in energy. In this situation the SE mechanism, assuming large energetic separation of donor/acceptor and bridge levels, may no longer apply. Beratan, Skourtis, and co-workers recently suggested a new model that might describe such situations, termed the flickering resonance (FR) model. In the FR model the medium between donor and acceptor is no longer considered as merely a bridge enhancing electronic coupling (as in the SE model, see section 5.1.1), but as a chain of redox sites, each of which can accept and donate electrons or holes. See Figure 10 B for an illustration of the FR mechanism. ET from donor to acceptor is assumed to take place when thermal fluctuations bring the redox active energy levels of donor, bridge, and acceptor sites *simultaneously* in alignment or resonance, in contrast to the SE model where bridge sites remain off-resonant during ET. Then the charge carrier is assumed to move with very little or no nuclear relaxation (i.e., ballistically) through the energy-aligned redox states to become trapped on the acceptor. This is in contrast to charge hopping (section 5.1.3), where the carrier moves sequentially from one site to the next and nuclear relaxation takes place between each step (Figure 10 C).

In the following the FR model introduced in ref 35 is examined in detail. To this end, an excess electron is considered that moves in a chain of M redox sites, including the donor, labeled $i = 1$, $N = M - 2$ bridge sites, with labels $i = [2, M - 1]$, and the acceptor, labeled $i = M$. The redox level of each site i is characterized by a probability distribution, $\rho_i(\Delta E_i)$, where

$$\Delta E_i = E_{O,i} - E_{R,i} \tag{70}$$

is the energy for removal of the excess electron from site i at fixed ionic configuration, termed electron removal energy. The state denoted "O" (for "oxidized") refers to the state with no excess electron present, and the state "R" (for "reduced") refers to the state with the excess electron present. A schematic of the energy level distributions of a system with three bridge sites is shown in Figure 11. I note in passing that the difference in electron removal energy between two sites i and j is equal to the energy for ET from i to j at fixed ionic configuration (=vertical ET energy) as defined in eq 4, $\Delta E \equiv \Delta E_{ji} = \Delta E_i - \Delta E_j$.

Generalizing Hopfield's formulation for nonadiabatic ET between two sites,[29] the FR model asserts that ET across the chain of sites takes place when the energy levels of all M sites match one another to within the electronic coupling between the sites, $\pm V$. The ET rate is written as the corresponding matching probability $P(M)$ times a frequency $1/\tau$

Figure 11. Definition of energetic quantities for ET in a simple donor−bridge−acceptor system treated in section 5.1.2. The thermal distribution of electron removal energies with respect to the vacuum level, eq 70, is indicated by Gaussians. All distributions have the same width σ_E. ΔE_D is the average vertical electron removal energy of the donor in the nuclear configurations of the reduced state, ΔE_B and ΔE_A are the average vertical electron removal energies of the bridge and acceptor sites in the nuclear configurations of the oxidized state (that is, average vertical electron affinity), respectively, and $\Delta E_{D/A}$ is the electron removal energy from a level halfway between the centers of the distributions for donor and acceptor. ΔA_{BD} and ΔA are the free energy differences for ET from the donor to the bridge and from the donor to the acceptor, respectively, and $\lambda = \sigma_E^2/(k_B T)$ is the reorganization free energy for ET from donor to bridge or acceptor sites.

$$k_{FR}(M) = \frac{1}{\tau} P(M) \tag{71}$$

where $1/\tau$ is associated with the rate-limiting process once an M-state resonance is reached. This is either the inverse transport time for an M-state resonance with finite lifetime (denoted $1/\tau_{trans}$ in ref 35) or the inverse trapping time of the carrier on the acceptor ($1/\tau_{trap}$), depending on whether transport or trapping is rate limiting.

For nonadiabatic ET between two states (no bridge sites, $M = 2$, $V = \langle |H_{ab}|^2 \rangle^{1/2}$), the FR rate eq 71 is equal to the nonadiabatic ET rate expression eq 24, with $1/\tau$ the Rabi frequency, $1/\tau_{rabi} = 2V/h$:

$$k_{FR}^{na}(2) = \frac{\pi^2}{\tau_{rabi}} P(2) \tag{72}$$

$$= k_{c,na} \tag{73}$$

Equation 73 holds if one makes the same assumptions that lead to the nonadiabatic rate eq 24, i.e., Gaussian distributions of the electron removal functions of donor and acceptor sites. A derivation of eq 73 is given in Appendix A.

The FR model extends the idea of the two-state matching probability to the M-state case. The probability that the ionization energy of the donor and the electron affinity of the $M-1$ electron accepting sites are all within $\pm V$ of one another is given by

$$P(M) = \int_{-\infty}^{\infty} d\Delta E_1\, \rho_1(\Delta E_1) \int_{\Delta E_1 - V}^{\Delta E_1 + V} d\Delta E_2\, \rho_2(\Delta E_2)$$
$$\cdots \int_{\max\{\Delta E_1, \Delta E_2, \ldots, \Delta E_{M-1}\} - V}^{\min\{\Delta E_1, \Delta E_2, \ldots, \Delta E_{M-1}\} + V} d\Delta E_M\, \rho_M(\Delta E_M) \tag{74}$$

This integral was solved in ref 35 by Monte Carlo integration. For a simple model of four sites with equal mean site energies

and width $\sigma = 0.16$ eV, $P(M)$ was found to decrease very fast with decreasing V, by about 3 orders of magnitude for each order of magnitude reduction in V. Moreover, $P(M)$ was found to decrease exponentially with the number of sites, i.e., with donor−acceptor distance.

In order to explain these numerical results for $P(M)$, an approximate upper bound of eq 74 was derived in ref 35. In Appendix B I derive a similar expression assuming Gaussian energy distributions with equal widths σ_E and different mean values for donor, bridge, and acceptor sites, as schematically shown in Figure 11. For large M ($M \geq 4$), one finds

$$P(R(M)) \leq \exp[-\Theta R]\, \exp\left[-\frac{(\Delta E_{D/A} - \Delta E_B)^2}{2\lambda k_B T}\right]$$
$$\exp\left[-\frac{(\Delta A + \lambda)^2}{4\lambda k_B T}\right] \tag{75}$$

$$\Theta = \frac{1}{\Delta R} \ln\left(\sqrt{\frac{\pi}{2}} \frac{\sigma_E}{V}\right) \tag{76}$$

where $\Delta E_{D/A} = (\Delta E_D + \Delta E_A)/2$, $\Delta E_D = \langle \Delta E_1 \rangle_R$ is the thermally averaged electron removal energy of the donor in the geometry of the reduced state (and the acceptor and brides sites in the oxidized state), $\Delta E_A = \langle \Delta E_M \rangle_O$ is the thermally averaged electron removal energy of the acceptor in the geometry of the oxidized state (with the donor and bridge sites in the oxidized state), and $\Delta E_B = \langle \Delta E_i \rangle_O$, $i \in [2, M-1]$, is the thermally averaged electron removal energy of a bridge site in the geometry of the oxidized state (with the donor and acceptor in the oxidized state). The latter is assumed to be the same for each bridge site. ΔA is the usual free energy difference for ET from D to A, $\lambda = \sigma_E^2/(k_B T)$ is the reorganization free energy for ET between two neighboring sites, $\Delta A + \lambda = \Delta E_D - \Delta E_A$, R is the total length of the chain of M sites, and ΔR is the (equidistant) spacing between the sites, $R = (M - 1)\Delta R$. An expression for the cases $M = 3$ and 2 is given in Appendix B. For the case M = 2 (no bridge site) eq 117 is recovered. For numerical evaluations of eq 75, it may be useful to express the energy gap $\Delta E_{D/A} - \Delta E_B$ in terms of free energies:

$$\Delta E_{D/A} - \Delta E_B = \Delta A_{BD} + (\lambda - \Delta A)/2 \tag{77}$$

A derivation of eq 77 is also given in Appendix B.

Hence, according to eq 75 the upper bound to the matching probability can be written as a product of three exponentially decaying terms. The first term on the right-hand side of eq 75 is an exponential distance decay with decay constant Θ given by eq 76. It is of similar form as the decay constant β in the SE mechanism eq 68, except that the energy gap $\Delta E_{D/A} - \Delta E_B$ is replaced by the width of the fluctuations of the electron removal energy, σ_E. This results in a weaker distance dependence than for the SE model (see section 5.1.4). However, the energy gap $\Delta E_{D/A} - \Delta E_B$ does enter the expression for the matching probability in the second exponential term, which is not present in the SE model. The third term on the right-hand side of eq 75 recovers the exponential part of the classical Franck−Condon factor, eq 25, which is also present in the SE model.

Besides $P(M)$, an estimate for the transmission time τ is required for transfer of the electron from the donor to the acceptor once all energy levels match to within $\pm V$; see eq 71. This could be done numerically by solving the time-dependent Schrödinger equation for a chain of cofactors with static energy

levels and electronic couplings. In ref 35 a lower limit to the transmission time was estimated in the infinite lifetime limit of the FR, $\tau_{trans}^{min} \approx R/\langle v \rangle$, where $\langle v \rangle = (2V/\hbar)\Delta R$. Hence, τ is expected to increase only linearly with M implying that the decay of the FR rate eq 71 is dominated by the exponential decay of $P(M)$.

Inserting eqs 77 and 75 in eq 71 and replacing τ by τ_{trans}^{min}, one obtains an upper estimate for the FR rate for a chain of equal bridge energy distributions and electronic couplings ($M \geq 4$):

$$k_{FR}^{max}(R(M)) = \frac{2\pi}{\hbar} \frac{V^2}{\sqrt{4\pi\lambda k_B T}} \frac{2\sqrt{2}}{\pi R/\Delta R} \exp[-\Theta(R - \Delta R)]$$
$$\exp\left[-\frac{(\Delta A_{BD} + (\lambda - \Delta A)/2)^2}{2\lambda k_B T}\right]$$
$$\exp\left[-\frac{(\Delta A + \lambda)^2}{4\lambda k_B T}\right] \tag{78}$$

with the decay constant Θ given by eq 76. In section 5.1.4 eq 78 for the FR rate is compared to the SE and hopping rate expressions. The FR model has been suggested as a possible mechanism for charge transport along DNA base pairs and heme chains.[35] Applications of the FR model to these systems will be discussed in sections 6.3 and 6.4.

5.1.3. Charge Hopping Model.
Charge hopping is an alternative mode of transport that can become relevant for longer bridges. In contrast to the SE mechanism, charge hopping is an incoherent transport channel where a localized excess electron or charge is assumed to hop between consecutive sites i and j, with hopping rates $k_{ji} \equiv k_{j \leftarrow i}$ given, e.g., by eq 24. The time dependent site populations of the charge, p_i, are given by a system of coupled first order differential equations:

$$\dot{p}_D = -k_{1D}p_D + k_{D1}p_1$$
$$\dot{p}_1 = k_{1D}p_D - (k_{D1} + k_{21})p_1 + k_{12}p_2$$
$$\vdots \tag{79}$$
$$\dot{p}_M = k_{MM-1}p_{M-1} - (k_{M-1M} + k_{AM})p_M + k_{MA}p_A$$
$$\dot{p}_A = k_{AM}p_M - k_{MA}p_A$$

where M is as above the number of bridge sites. As discussed in ref 157, the assumption of first order kinetics is justified when the charge population on the bridge remains small. In this case the second order rates (a charge can hop from i to $i + 1$ only of i is occupied and $i + 1$ is not occupied) becomes first order, $k_{i+1i}p_i(1 - p_{i+1}) \approx k_{i+1i}p_i$, for $p_{i+1} \ll 1$. The bridge population remains small if the bridge levels are energetically well separated from the donor/acceptor levels.

Here one is interested in the steady state flux through the chain when the donor is a constant source p_D = const and the acceptor population is instantly drained so that $p_A = 0$. This can be realized, for instance, by a fast equilibrium between the donor and an external electron source in excess concentration, and a fast and irreversible ET from the acceptor to an external electron sink. Moreover, one assumes that all rate constants between bridge sites are equal, $k_{ij} = k_{BB}$, which implies that they are on the same (free) energy level. At steady state, $\dot{p}_i = 0 \; \forall \; i$, the flux J of electrons transferred between neighboring sites is the same and equal to the flux through the entire chain (no

charge accumulation/loss at any site). The steady state flux is given by

$$J = k_{hop}p_D \tag{80}$$

$$k_{hop}(R) = \frac{\exp[-\Delta A_{BD}/(k_B T)]}{1/k_{AN} + 1/k_{D2} + [(R/\Delta R) - 2]/k_{BB}} \tag{81}$$

where ΔA_{BD} is the free energy difference for ET from the donor to the bridge sites. Equations 80 and 81 can be readily derived by simple algebraic manipulation of the linear eq 79 using the above boundary conditions; see ref 157 for details. The kinetic constant k_{hop} can be interpreted as an effective rate constant for hopping from the donor to the acceptor via the bridge sites. Importantly, the hopping model predicts that the effective hopping rate k_{hop} decreases linearly with the number of bridge sites, i.e., as $1/R$, in contrast to the exponential distance dependence of the SE and FR rates, eqs 69 and 78, respectively.

5.1.4. Analysis.
The FR mechanism was only very recently suggested as an alternative to SE. There are still a number of uncertainties with regard to this mechanism concerning, e.g., the form of the prefactor that should be best used with this theory and the treatment of the site fluctuations. The latter may be strongly correlated in contrast to what was assumed in section 5.1.2. With these caveats in mind, I compare here the FR rate eq 78 derived for the simple donor–bridge–acceptor system in Figure 11 to the corresponding SE rate eq 69.

$$r_1 = \frac{k_{FR}^{max}}{k_{SE}} = \frac{2\sqrt{2}\,\Delta R}{\pi R} \exp[(\beta - \Theta)(R - \Delta R)]$$
$$\exp\left(-\frac{(\lambda + 2\Delta A_{BD} - \Delta A)^2}{8\lambda k_B T}\right) \tag{82}$$

where Θ and β are given by eqs 76 and 68, respectively. Assuming typical values $\Delta E_{D/A} - \Delta E_B = 1$ eV and $\sigma_E = 0.15$ eV (corresponding to $\lambda = 0.9$ eV at 300 K), the ratio $\Theta/\beta \approx 0.1$, implying that the FR model has a much softer distance dependence than the SE model. Therefore, the first exponential term on the RHS of eq 82 is positive and exponentially increasing with distance R. At small distances or, equivalently, a small number of sites, this term is small and the ratio will be dominated by the second exponential term on the RHS of eq 82. Thus, for very short bridges (typically one to two bridge sites) SE is favored over FR ($r_1 < 0$). For longer bridges (typically three to four bridge sites) the distance dependent exponential term increases leading to a crossover from SE to FR ($r_1 > 0$). For even longer bridges SE is not competitive due to the much sharper distance decay compared to FR. Moreover, one can expect that a decrease in electronic coupling will reduce the SE rate more than the FR rate because β is more sensitive to changes in V than Θ (factor 2 in front of logarithm in eq 68). The dependence on the free energies is more complicated, but for most situations a reduction in bridge free energies ΔA_{BD} should increase the FR rate more than the SE rate.

For comparison of FR to hopping, I assert that in eq 81 the rates k_{D2} and k_{AN} are not too small compared to k_{BB} so that k_{hop} exhibits the usual $1/R$ dependence. Assuming $k_{D2}, k_{AN} \geq k_{BB}$, which is fulfilled for the wide parameter range $0 \leq \Delta A_{BD} \leq 2\lambda$, $\Delta A_{BD} - 2\lambda \leq \Delta A \leq \Delta A_{BD}$, the hopping rate eq 81 is bound from below by $k_{hop}^{min} = k_{BB} \exp[-\Delta A_{BD}/(k_B T)]\Delta R/R$, $k_{hop}^{min} \leq k_{hop}$. Using this lower bound, one finds for the ratio between k_{FR}^{max}, eq 78, and k_{hop} the following relation:

$$r_2 = \frac{k_{FR}^{max}}{k_{hop}} \leq \frac{k_{FR}^{max}}{k_{hop}^{min}} = \frac{2\sqrt{2}}{\pi} \exp[-\Theta(R - \Delta R)]$$

$$\exp\left(-\frac{C\lambda}{4k_BT}\right) \leq 1 \tag{83}$$

$$C = \left(\frac{\Delta A_{BD} - \Delta A}{\lambda}\right)^2 + \left(\frac{\Delta A_{BD}}{\lambda} - 1\right)^2 + \frac{1}{2}\left(\frac{\Delta A}{\lambda} + 1\right)^2$$

$$- 1 \geq 0 \tag{84}$$

The constant $C \geq 0$ for all values of ΔA_{BD}, ΔA, and λ. It takes a minimum $C = 0$ at $\lambda = 2\Delta A_{BD}$, $\Delta A = 0$ for any value of ΔA_{BD}. Hence, the first and the second exponents in eq 83 are always negative. This implies that at least for the simple model system investigated, with equal distribution functions and couplings for each site, and a bridge representing a rectangular free energy barrier between donor and acceptor, the FR rate is smaller than or equal to the hopping rate. Of course, it can be questioned whether this perhaps unexpected result carries over to real systems, especially with the above-mentioned caveats in mind. Different rate prefactors and/or a better treatment of correlated fluctuations in the FR model may tip the balance among mechanisms. In this respect I note that some of the correlation effects may be captured using, e.g., MD simulations to estimate distributions for site energies and electronic couplings.

5.1.5. Hopping Maps. In 2008 Gray and co-workers found evidence that $Cu(I) \rightarrow Re(II)$ ET in Re-labeled azurins is accelerated by an intervening tryptophan residue by 2 orders of magnitude.[93] More recently, the same group reported a more than 10-fold increase in the $Cu(I) \rightarrow Ru(III)$ ET rate in Ru-labeled azurins by an intervening nitro-tyrosine residue.[260] These observations were interpreted in terms of a switch of mechanism from electron tunneling to two-step hopping with the singly oxidized tryptophan/nitro-tyrosine residue as a charged intermediate. In their analysis, the hopping rate calculated for a single intermediate using typical values for reorganization free energies (0.8 eV) and distance decay constants (1.1 $Å^{-1}$) was in good agreement with the experimental rate constant, whereas the calculated SE rate was found to be significantly lower.

The question hopping vs SE prompted the authors to develop so-called hopping maps or hopping advantage maps.[259,261] This is the ratio between the two rates, $\ln(k_{hop}/k_{SE})$ plotted as a function of two parameters, e.g., the donor–acceptor free energy difference and the intermediate–acceptor free energy difference. Applied to the above-mentioned azurin systems, these maps have revealed clear boundaries where hopping dominates over SE and vice versa. They could be particularly useful for the design of hopping systems.[260] Here $\ln(k_{hop}/k_{SE})$ is plotted as a function of the distance between given donor and intervening residue and between the latter and a given acceptor as well as for different values of the intermediate–acceptor free energy difference. The map then reveals the optimal positioning and the optimal free energy of the intermediate to give the highest hopping advantage. Further details on hopping maps can be found in a recent review.[56]

5.2. Ultrafast ET

The treatment of ET reactions in the usual Marcus picture assumes a canonical equilibrium distribution of all possible microstates of donor and acceptor, as implied by the brackets

$\langle\cdots\rangle_M$. This was also a crucial assumption in the derivation of the SE, FR, and hopping models in section 5.1. The assertion of equilibrium thermodynamics can be expected to give a good approximation if the ET rate is slower than the slowest system vibrational mode coupling to ET.[157] Molecular dynamics simulations have shown that for small proteins the slowest modes coupling to ET are due to the electroelastic fluctuations of the protein/water interface occurring on the 1−10 ns time scale.[36] Even longer time scales may be possible, e.g., when large protein conformational changes couple to ET (see section 5.3). Hence, one can expect that for slow to modestly fast biological ET reactions occurring on the millisecond to microsecond time scale, equilibrium statistical mechanics and Marcus theory give an adequate description. Indeed, the successful interpretation of many experimental measurements of millisecond to microsecond biological ET reactions are an undeniable proof for the strength of this theory.

However, some biological ET reactions are ultrafast, occurring on the nanosecond to picosecond (ns−ps) time scale, e.g., heme a to a_3 electron tunneling in cytochrome c oxidase (ns), hole transport in DNA, DNA photolyase, and cryptochrome (ns−ps), and primary charge separation in photosystem II (ps). In these systems the ET is comparable to or faster than the electroelastic fluctuations at the biomolecule/water interface. Hence, a significant fraction, if not all, of these fluctuations are frozen on the time scale of the ET, invalidating the use of canonical equilibrium statistical mechanics. Consequently, the time averages measured in experiment are no longer equal to the canonical equilibrium averages, which means that the system is nonergodic.
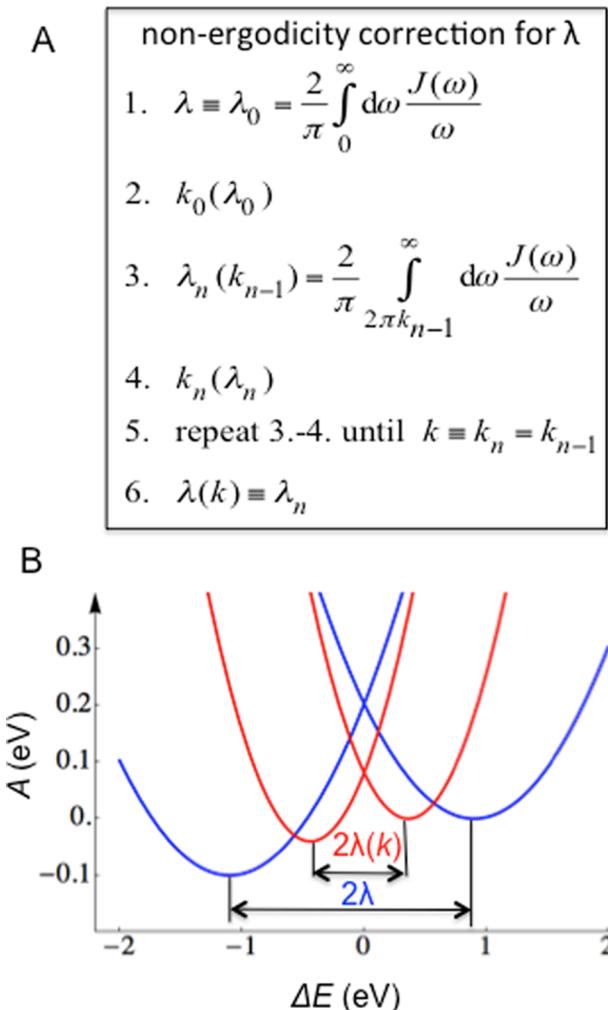
5.2.1. Nonergodicity Correction. Matyushov and co-workers suggested a simple correction for nonergodic effects based on the theory of dynamically restricted canonical ensembles.[262] The formalism is similar to equilibrium statistical mechanics with the crucial difference that integration is not done over full phase space, but over the part of phase space that is accessible on the time scale of the ET event. As a consequence, reorganization free energy, average energy gap, free energy difference, and activation free energy become a function of the ET rate.

If one assumes that the ET rate constant is known from experiment, say k, one can replace in the formula for the canonical reorganization free energy in the frequency domain, eq 62, the lower integration limit "0" by "k". This leads to the definition of a noncanonical (or nonergodic) reorganization free energy

$$\lambda(k) = \frac{2}{\pi} \int_k^\infty d\omega \, \frac{J(\omega)}{\omega} \tag{85}$$

which includes only the contributions from modes that are at least as fast as the reaction rate. However, these fast contributions are averaged over all of configuration space including the part described by the slow modes, because the spectral density function J is formally obtained from infinitely long trajectories. A similar correction has been suggested for the rate dependent average energy gap $\Delta E_A(k)$[36,234] and for the free energy difference $\Delta A(k)$ by virtue of $\Delta A(k) = \Delta E_A(k) - \lambda(k)$. In case the ET rate constant is not known experimentally, one could solve the equations for $\lambda(k)$ and $\Delta A(k)$ together with the one for the ET rate (k_{ET}, e.g., eq 25) self-consistently until $k_{ET} = k$; see scheme in Figure 12A.

Application of eq 85 to the picosecond primary charge separation reaction in bacterial photosynthesis has given a

A
non-ergodicity correction for λ

1. $\lambda \equiv \lambda_0 = \dfrac{2}{\pi} \displaystyle\int_0^\infty d\omega \, \dfrac{J(\omega)}{\omega}$

2. $k_0(\lambda_0)$

3. $\lambda_n(k_{n-1}) = \dfrac{2}{\pi} \displaystyle\int_{2\pi k_{n-1}}^\infty d\omega \, \dfrac{J(\omega)}{\omega}$

4. $k_n(\lambda_n)$

5. repeat 3.-4. until $k \equiv k_n = k_{n-1}$

6. $\lambda(k) \equiv \lambda_n$

B

Figure 12. (A) Self-consistent correction scheme for reorganization free energy for fast (nonergodic) ET reactions. The lower integration limit ($2\pi k_{n-1}$) for the spectral density function J (eq 29) is iterated until it is equal to the ET rate k. The result is a nonergodic reorganization free energy, $\lambda(k)$, that is smaller than the equilibrium reorganization free energy including all frequencies, λ. In (B) parabolic free energy profiles are drawn for the equilibrium case (blue) and after the nonergodicity corrections have been applied (red). The nonergodicity correction for the free energy difference between the two states, i.e., the vertical difference between the minima, is assumed to result in the same scaling factor as for reorganization free energy. The Stokes shift is indicated by twice the reorganization free energy. See section 5.2.1 for further details.

spectacular reduction in reorganization free energy from unphysically high values of 2.36 eV obtained from integration over all frequencies (eq 62) to about 0.36 eV[233,234] in good agreement with the experimental estimate of 0.22 eV;[24] see Table 1. A similar analysis for heme a to a_3 tunneling in cytochrome c oxidase is discussed in section 6.2. In general, the result of dynamical freezing of the slow modes is that reorganization and activation free energy as well as the magnitude of the free energy difference decrease compared to canonical equilibrium conditions, as shown schematically in Figure 12B.

5.2.2. Sumi–Marcus theory. The elimination of slow modes according to the nonergodicity correction discussed in section 5.2.1 gives self-consistent rate-adjusted ET parameters. When used in the framework of Marcus theory, the kinetics

described by these parameters is still monoexponential. More complicated multiexponential decay kinetics, as measured, e.g., for photosynthetic reaction center proteins, requires a treatment beyond the standard Marcus formalism.[112] Multiexponential decay implies that motions on at least two different time scales couple to ET. In their theory developed some time ago, Sumi and Marcus describe the ET by two coordinates, one coordinate P for a fast polarization response and another coordinate q for a slow polarization response compared to the ET time scale.[119] In case of the picosecond photosynthetic charge separation reaction P would correspond to the subpicosecond response of the intramolecular vibrations of the cofactors, and q would correspond to all other relaxation processes of the protein and solvent. The total energy gap is assumed to be a linear function of P and q

$$\Delta E = aP + bq \tag{86}$$

resulting in a fast energy gap component, $\Delta E_P = aP$, and a slow component, $\Delta E_q = bq$. The fast component ΔE_P is assumed to be in thermal equilibrium for each value of ΔE_q, whereas the slow component ΔE_q is assumed to diffuse on a free energy surface $A(\Delta E_q)$ with diffusion coefficient D. The rate for ET along the ΔE_P direction is $k(\Delta E_q)$. In this picture the initial state population p is a function of ΔE_q and time only, $p(\Delta E_q, t)$, with a time dependence given by the diffusion-reaction (Fokker−Planck) equation[119]

$$\frac{\partial p}{\partial t} = D \frac{\partial}{\partial \Delta E_q} \left[\frac{\partial p}{\partial \Delta E_q} + \frac{1}{k_B T} p \frac{\partial A(\Delta E_q)}{\partial \Delta E_q} \right] - k(\Delta E_q)p \tag{87}$$

and the ET rate is obtained from the initial state population decay
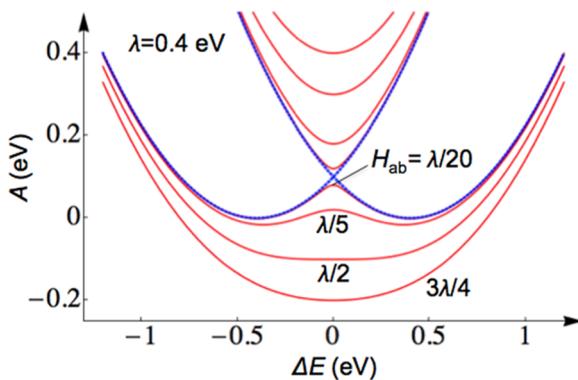
$$k_{ET} = \left. \frac{d \ln p}{dt} \right|_{t \to 0} \tag{88}$$

Matyushov and co-workers have stressed that also in this formalism a nonergodicity correction is necessary in the form of a self-consistent ET rate-adjusted diffusion coefficient $D \to D(k_{ET})$ and free energy surface, $A(\Delta E_q) \to A(k_{ET}, \Delta E_q)$. Indeed, the authors have shown that self-consistent solutions to eqs 87 and 88 using data from MD simulation give good agreement with the multiexponential decay kinetics reported for a number of mutants of *Rhodobacter sphaeroides*.[112] The dynamical quenching of the slow protein response was suggested to be an important mechanism enabling ultrafast biological ET while reducing the loss of free energy to heat.[36]

A note of caution may be appropriate at this point. In certain systems the nonergodicity correction may lead to small reorganization free energies on the order of the electronic coupling matrix element. Then one needs to verify if the assumption of localized charge carriers and the use of the nonadiabatic or adiabatic rate formalisms (eqs 24, 26) are still appropriate, or if the carrier is delocalized and explicit charge propagation schemes should be used, as discussed in section 5.2.3.

5.2.3. Nonadiabatic Molecular Dynamics. In all previous sections it was assumed that initial and final ET states are characterized by potential wells that are sufficiently deep so that localized charge carriers can form in initial and final states. This is the case when reorganization free energy, after correction for possible nonergodic effects according to eq 85, is still

significantly larger than electronic coupling, $\lambda(k) \gg H_{ab}$. An interesting situation occurs when this is no longer true. In Figure 13 I show the adiabatic free energy curves for different

Figure 13. ET free energy curves for large ratios H_{ab}/λ. The diabatic free energy curves eqs 11 and 12 are drawn in blue for $\lambda = 0.4$ eV and $\Delta A = 0$ eV. Adiabatic ground and excited state free energy curves are obtained according to eq 10, and drawn in red for increasing values of electronic coupling H_{ab} at constant $\lambda = 0.4$ eV. At $H_{ab} = \lambda/20$ the ET can be classified as nonadiabatic, and at $\lambda/5$ it can be classified as adiabatic. For $H_{ab} \geq \lambda/2$ the free energy barrier disappears and the transition state at $\Delta E = 0$ becomes a minimum.

values of the ratio λ/H_{ab}. If $\lambda/H_{ab} \leq 2$, the activation barrier for ET vanishes according to eqs 18 and 19 (at $\Delta A = 0$), and the transition state becomes a minimum. In this regime the excess electron is no longer localized on one cofactor or molecular fragment, but spontaneously delocalizes; the ET rate becomes ill-defined. This scenario may occur for two or more closely spaced cofactors or DNA bases with strong electronic interactions and surrounded by a low dielectric and/or slowly responding (viscous) medium.

The phenomenon of excess charge delocalization is well-known in the chemistry literature on mixed-valence compounds, where the degree of delocalization is classified according to Robin and Day.[263] In class I compounds the excess charge is highly localized, in class II compounds there is some localization of distinct valences but with low activation energy for interconversion, and in class III compounds the excess charge is completely delocalized. Textbook examples for class I, II, and III compounds are Pb_3O_4, tetrathiafulvalene[264] (also correctly predicted by CDFT[130,205]) and the Creutz−Taube ion.[265]

Considering a chain of closely spaced ionizable sites, the situation also has some similarity with the band transport problem in solids. However, in contrast to solids, the thermal fluctuations in proteins are so large that the mean free path of the electron is smaller than the typical site spacings, making band-theoretical approaches inapplicable. In other words, in this regime the electronic interaction between the sites can no longer be treated as a perturbation as is done in Marcus theory, while the strong nuclear fluctuations in proteins cannot be treated as a perturbation to the electronic problem as is done in band theory. Nuclear and electronic motion can no longer be safely separated and the coupled nuclear−electronic problem should be solved instead.

Potential solutions to this problem are direct propagation schemes of the coupled electron−nuclear motions. In particular, mixed quantum−classical (MQC) nonadiabatic molecular dynamics (NAMD) methods have been developed

for (bio)molecular systems including the very early work by Warshel and co-workers,[266,267] with applications to charge separation in photosynthetic reaction center proteins,[268] mean field (MF) Ehrenfest, and fewest switches surface hopping (SH).[269−272] These approaches are also referred to as semiclassical trajectory methods because nuclear motion is treated using classical mechanics and electronic motion is treated quantum mechanically. MF and SH have served as the methods of choice for the last 20 years, primarily in the context of ab initio and DFT electronic structure calculations of photoexcitation processes.[272] Also electron transfer reactions in the gas phase have been investigated by combining the MF approach with real-time TDDFT.[273] (In the latter study the competition between superexchange and hopping was investigated for a small donor−bridge−acceptor system.) Recently, the MF and SH methods have been adopted for simulation of thermal charge transport in larger, biological systems such as DNA and proteins.[37,38,250,274,275] I note in passing that charge transfer in organic semiconducting materials is in a similar regime,[199,276,277] and first NAMD simulations for simple one-dimensional model Hamiltonians[278−281] and approximate NAMD simulations for a slab of organic molecules[282] have recently been reported.

MF and SH are MQC schemes where the electronic wave function $\Psi(t)$ is expanded in a set of adiabatic electronic states ϕ_l (ϕ_0 and ϕ_1 for a simple two-state donor−acceptor problem)
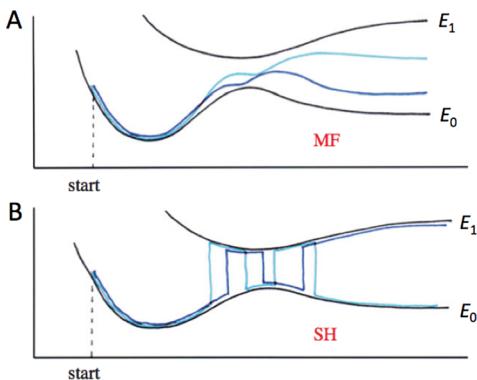
$$\Psi(t) = \sum_l c_l(t)\, \phi_l(\mathbf{R}(t)) \tag{89}$$

with $c_l(t)$ the time dependent expansion coefficients and $\mathbf{R}$ the position vector of all nuclear coordinates. Insertion of eq 89 in the time-dependent electronic Schrödinger equation gives

$$i\hbar \dot{c}_k = \sum_l c_l(H_{kl} - i\hbar \mathbf{d}_{kl}\cdot\dot{\mathbf{R}}) \tag{90}$$

where H_{kl} are the Hamiltonian matrix elements, $\mathbf{d}_{kl}$ are the nonadiabatic coupling vectors between states k and l, and $\dot{\mathbf{R}}$ is the velocity vector for all nuclei. The expansion coefficients are propagated in time according to eq 90 for a time dependent electronic Hamiltonian as determined by the classical nuclear motion. The crucial difference between MF and SH is the way how the classical nuclear dynamics is treated. In MF the nuclei move on a mean field electronic surface composed of the adiabatic potential energy surfaces $E_k = H_{kk}$ (e.g., E_0, E_1 given by eq 3 for a two-state system) with weights proportional to the electron coefficients $|c_k|^2$; see Figure 14A. In the SH method the nuclei are propagated on a single adiabatic surface E_k at any time and transitions between surfaces $E_l \leftarrow E_k$ occur stochastically according to a transition probability derived by Tully;[269] see Figure 14B. In both cases initial state population decay occurs when the nuclear dynamics generates nuclear configurations where the initial electronic state becomes (quasi)-degenerate with an excited electronic state. In practice, one needs to run a large number of Ehrenfest of SH trajectories with different initial conditions. Then effective ET rates can be obtained from the ensemble averaged time-dependent decay of the initial charge population and charge mobilities calculated from the mean square displacement of the center of excess charge versus time.

The strength of NAMD approaches is that the ET mechanism is, in principle, a result of the calculation, in contrast to Marcus or band theory, which are based on a preconceived picture of the ET process. However, the

Figure 14. Two popular quantum−classical nonadiabatic molecular dynamics (NAMD) methods: (a) mean-field (MF) Ehrenfest MD and (b) surface hopping (SH) MD. For each case, two adiabatic potential energy surfaces are shown, E_0 and E_1. The trajectories of two independent simulations are indicated in blue. After passing the high-coupling region at the avoided crossing, the trajectories evolve on a potential that is an average of E_0 and E_1 in the MF simulations. By contrast, the trajectories evolve on either E_0 or E_1 in the SH simulations. Reprinted with permission from ref 38. Copyright 2013 The Royal Society.

computationally amenable MF and SH approaches still have a number of well-known shortcomings (see below) and a major drawback is their very high computational demand, in particular when the electronic structure problem is solved at the ab initio[283] or DFT level.[273,284] Elstner and co-workers have addressed the problem of efficiency by developing MF and SH implementations based on self-consistent charge density functional tight binding (SCC-DFTB) calculations of the electronic Hamiltonian. This allows for an efficient propagation of the coupled electron−nuclear motions for relevant biological systems on the picosecond−nanosecond time scale. I refer here to two recent reviews by the authors for a detailed presentation of their implementation.[37,38] Applications of the method to DNA and DNA photolyase are discussed in sections 6.4 and 6.5.

The shortcomings of the MF approach are well documented (see ref 285 and references therein): (1) while a reasonably good approximation to the short time dynamics of the system is obtained, after reaching an avoided crossing the system remains in a mixed state indefinitely instead of returning to one of the adiabatic states. A consequence of this is unphysically large delocalization of the excess electron or hole. (2) The method does not satisfy a detailed balance between quantum and classical subsystems, resulting in the quantum system acquiring too much energy during the course of the reaction. (3) A quantum−classical method, the MF method neglects nuclear quantum effects, which can become important at low temperatures. Issue 1 has been addressed by Jasper and Truhlar in their decay-of-mixing approaches, which impose demixing of the electronic states, i.e., a decoherence correction, to model the dissipative effect of the environment on the electronic dynamics.[286−288]

The SH method and its latest extensions and modifications also improve on these issues. The stochastic hops mimic the effect of branching of the nuclear wave packets at the crossing region and the nuclei are propagated at any time on a pure adiabatic state. In recent analyses of the equilibrium limits of the SH method for a two-level[289] and a three-level model system,[290] it was found that SH does not in general yield a

Boltzmann equilibrium population of the electronic states but that in practice the observed deviations are small, especially in the limits of small electronic coupling (H_{ab}) and/or strong nonadiabatic coupling ($\mathbf{d}_{kl}$). Recently, nuclear quantum effects were incorporated in the SH method[291] by combining it with ring polymer molecular dynamics[39,292] (see also section 5.4.2). The tunneling contribution to the rate for a one-dimensional two state model of a nonadiabatic reaction could be well reproduced when compared with exact quantum mechanical calculations.
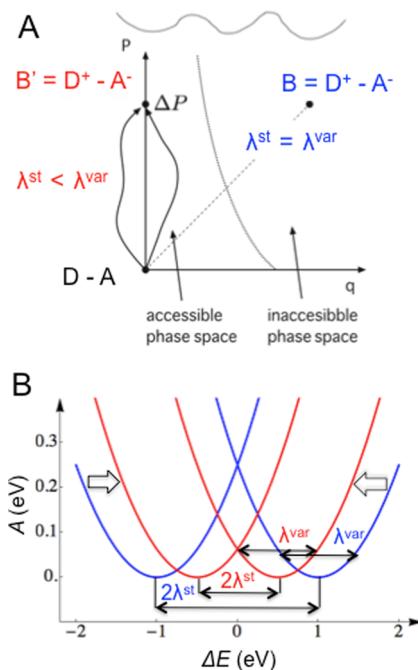
A longstanding problem of standard SH that is particularly relevant for ET simulations is the missing decoherence of the electronic wave function. After passing the crossing region, the off-diagonal electronic density matrix element does not decay sufficiently, leading to an overly coherent electronic wave function with probability density on two or more surfaces. This shortcoming is not new and has been addressed by many researchers.[286,293−297] One of the simplest approaches is to collapse the electronic wave function to a single adiabatic state after leaving the crossing region.[294] More recently, the issue was readdressed by Subotnik and co-workers in a series of papers. Using a simple spin-boson model, the authors found that standard SH rates without decoherence correction scale incorrectly with electronic coupling.[298] They suggested an augmented SH algorithm where decoherence is introduced by stochastically collapsing the electronic wave function according to a rate that depends on positions and momenta.[296,297] The new algorithm, denoted A-FSSH, was shown to recover the correct scaling of ET rates with electronic coupling.[297]

In summary, the field of NAMD simulation has been and remains a very active and vibrant field of research. First implementations have become available that open up the field to applications in condensed phase biological and organic ET and several research groups aim at improving some of the known shortcomings of the original methods introduced some time ago. It remains to be seen if new and improved but still computationally practical NAMD algorithms will be developed in the years to come (see also perspective by John Tully[285]).

5.3. ET Coupled to Slow Conformational Transitions

An interesting problem occurs when ET is coupled to slow relaxation in the ET product state, e.g., a conformational transition of the protein. The latter typically takes place on the millisecond−microsecond or even longer time scales. The situation can be cast again in terms of Sumi−Marcus theory[119] (see section 5.2.2). The fast coordinate P now describes the nanosecond−picosecond response of the cofactors, amino acid side chains, solvent, and water/protein interface, and the slow coordinate q describes the conformational transition of the protein on the millisecond−microsecond or longer time scale; see Figure 15A. The difference with respect to the fast ET discussed in section 5.2.2 is that the equilibrium state on the product surface is effectively never reached within the time scale of ET due to a very large thermodynamic or kinetic barrier for the protein conformational transition, closely corresponding to the "narrow reaction window" limit of Sumi−Marcus theory.

More recently, Matyushov and co-workers suggested an alternative approach to this problem, again based on the concept of the dynamically restricted canonical ensemble.[262] The equilibrium distributions for P and q are assumed to be Gaussian, centered around P_A and q_A with widths σ_P and σ_q, respectively. The equilibrium distribution of ΔE is then the convolution of the two distributions:

Figure 15. (A) Electron transfer coupled to slow conformational change of the protein. The initial state is denoted D−A and the final state D$^+$−A$^-$. The reaction is described by a fast collective coordinate P for the protein and solvent modes coupling to ET and a coordinate q for the slow conformational change. ET along P occurs on a faster time scale than protein conformational change along q, resulting in the formation of a local minimum B′ rather than the equilibrium state B on the product surface. In (B) parabolic free energy profiles are drawn for the equilibrium case (A → B, $\lambda^{st} = \lambda^{var}$, blue) and for the case where protein conformational change is quenched (A → B′, $\lambda^{st} < \lambda^{var}$, red). The freezing of the protein conformational transition leads to a reduced Stokes shift as indicated by the block arrows but is assumed to leave the fluctuations (curvature of the profiles) unchanged. Consequently, the ET activation free energy is reduced by a factor $\chi_G^{-2} = (\lambda^{st}/\lambda^{var})^2$. See section 5.3 for further details. Adapted with permission from ref 36. Copyright 2013 AIP Publishing LLC.

$$p_A(\Delta E) = \text{const} \int_{-\infty}^{\infty} dP \exp\left(-\frac{(P - P_A)^2}{2\sigma_P^2}\right)$$
$$\exp\left[-\frac{\left(\left(\frac{1}{b}(\Delta E - aP)\right) - q_A\right)^2}{2\sigma_q^2}\right] \tag{91}$$

$$= \text{const} \exp\left[-\frac{(\Delta E - \Delta E_A)^2}{2\sigma_A^2}\right] \tag{92}$$

which is also Gaussian with width $\sigma_A = (a^2\sigma_P^2 + b^2\sigma_q^2)^{1/2}$ and center $\Delta E_A = aP_A + bq_A$. The corresponding equilibrium reorganization free energy is

$$\lambda_A^{var} = \frac{\sigma_A^2}{2k_B T} = \lambda_P + \lambda_q \tag{93}$$

where $\lambda_P = a^2\sigma_P^2/(2k_B T)$ and $\lambda_q = b^2\sigma_q^2/(2k_B T)$. One further assumes that ET is slow enough so that both the fast and the slow protein modes coupling to ET are sufficiently well sampled in the reactant state (picoseconds−nanoseconds), but faster than the slow conformational transition in the product state (milliseconds−microseconds); i.e., ET is assumed to take

place in the microsecond−nanosecond range. Because of the separation of time scales, ET will occur along the fast P coordinate while the q coordinate is frozen at the equilibrium value for A. Consequently, the system gets trapped in a local minimum in the product state, denoted in the following as B′; see Figure 15A. The missing relaxation in the q direction means that the Stokes shift and the corresponding reorganization free energy for ET to B′

$$\lambda^{st} = \frac{a}{2}(P_A - P_{B'}) = \frac{1}{2}(\Delta E_A - \Delta E_{B'}) \tag{94}$$

are smaller than for ET to B, $\lambda^{st} = \lambda_P < \lambda_A^{var}$. The free energy difference between B′ and A is then given by

$$\Delta A \equiv \Delta A_{B'A} = \Delta E_A - \lambda^{st} \tag{95}$$

Assuming for simplicity that the fluctuations in B′ are the same as in the initial state A, $\lambda_{B'}^{var} = \lambda_A^{var} \equiv \lambda^{var}$, these considerations lead to two parabolas that for a given curvature (or λ^{var}), have a horizontal separation of minima that is smaller than in standard Marcus theory; see Figure 15B. This has two important consequences: (i) the linear free energy relation eq 9, which is exact for a canonical ensemble, is no longer valid and (ii) the activation free energy is smaller than in the Marcus picture, eq 17. One can readily show that a slightly modified linear free energy relation holds in this situation. The expressions for the parabola for states A and B′ are

$$A_A(\Delta E) = \frac{1}{4\lambda^{var}}(\Delta E - \Delta E_A)^2 \tag{96}$$

$$A_{B'}(\Delta E) = \frac{1}{4\lambda^{var}}(\Delta E - \Delta E_{B'})^2 + \Delta A \tag{97}$$

Subtracting eq 96 from eq 97 and inserting eqs 94 and 95, one obtains

$$A_{B'}(\Delta E) - A_A(\Delta E) = \chi_G^{-1}\Delta E + (1 - \chi_G^{-1})\Delta A \tag{98}$$

where

$$\chi_G = \frac{\lambda^{var}}{\lambda^{st}} \geq 1 \tag{99}$$

Hence, for small ΔA the free energy gap is smaller than the energy gap by the ratio of reorganization free energies, eq 99. If the system is ergodic, i.e., $\chi_G = 1$, eq 98 reduces to the standard linear free energy relation eq 9. Importantly, the (nonadiabatic) activation free energy for ET is now given by

$$\Delta A_{na}^{\ddagger} = A_A(0) - A_A(\Delta E_A) = \frac{(\lambda^{st} + \Delta A)^2}{4\lambda^{var}} \tag{100}$$
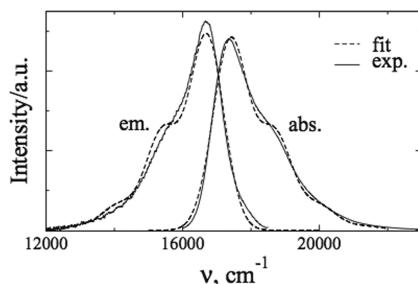
where use of eqs 96 and 95 was made. The ratio of activation free energies for the nonequilibrium reaction A → B′, $\Delta A_{na}^{\ddagger} = \lambda^{st\,2}/(4\lambda^{var})$, and the equilibrium reaction A → B, $\Delta A_{na}^{\ddagger} = \lambda^{var}/4$ (assuming $\Delta A = 0$ for both cases), is then given by

$$\frac{\Delta A_{na}^{\ddagger}(A \rightarrow B')}{\Delta A_{na}^{\ddagger}(A \rightarrow B)} = \chi_G^{-2} \tag{101}$$

Hence, the fact that the conformational transition is too slow to occur on the time scale of the ET reaction leads to a reduction in activation free energy proportional to the square of χ_G. Note, one arrives at this result by requiring that the ET is faster than the slow conformational transition (reduction of Stokes shift, i.e., λ^{st}), but slow enough to couple to the electroelastic

fluctuations that promote the conformational transition (retention of fluctuations, i.e., λ^{var}).

Evidence for nonergodic effects of this kind has been obtained from the line shape analysis of mStrawberry fluorescent protein; see Figure 16. The Stokes shift between

Figure 16. Absorption and emission lines of mStrawberry fluorescent protein (solid lines) and their fit by vibronic progression of Gaussian lines (dashed lines). Note, the Stokes shift is significantly smaller than what one would expect from the widths of the lines, as expressed by the ratio $\chi_G = \lambda^{var}/\lambda^{st} = 1.8$. Reprinted with permission from ref 36. Copyright 2013 AIP Publishing LLC. See ref 368 for experimental data.

absorption and emission lines is significantly smaller than what one would expect from the widths of the lines. The ratio eq 99 deviates significantly from unity, $\chi_G = 1.8$. A discussion of other examples can be found in ref 36. Returning to the relevance for biology, the dynamical freezing of possible protein conformational changes may be interpreted as an effective mechanism that allows for fast biological ET to happen while avoiding the (irreversible) formation of very low free energy states.

5.4. Path-Integral Based Approaches
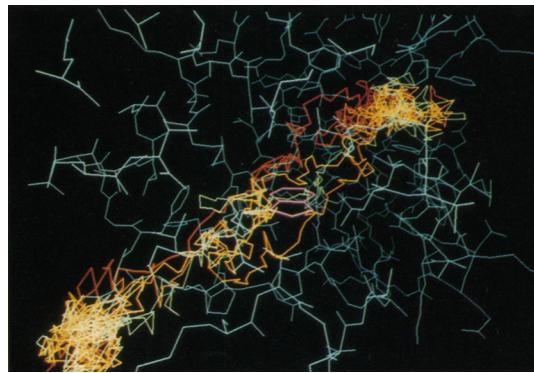
5.4.1. Pseudopotential-Based Path-Integral Monte Carlo. In their pioneering work dating back to 1987, Kuki and Wolynes used the imaginary time path-integral formulation of quantum mechanics[299,300] to model electron tunneling in a Ru-modified protein (Ru-pentammine labeled Zn-porphin myoglobin).[96] The excess electron was treated as a quantum particle that interacts with the fixed nuclear cores of the protein via one-electron pseudopotentials. The authors showed that the electronic coupling matrix element for electron tunneling across the protein is related to the free energy difference A_k required to generate a "kink" in the polymer chain for the electron relative to configurations where the chain is confined to the reactant well. A kink was defined as a polymer configuration where one terminal bead is in the donor well, the other terminal bead is in the acceptor well, and the beads in between, spanning the intervening protein space between the two wells,

$$H_{ab} = k_B T \, \exp[-A_k/(k_B T)] \tag{102}$$

(In ref 96 H_{ab} is denoted Δ.) Examples for kinked configurations of the polymer chain for an excess electron are shown in Figure 17. The problem can be cast equivalently in terms of the time evolution of a two-level system with initial diabatic state ϕ_a and final diabatic state ϕ_b.[301] Assuming a time-independent Hamiltonian with off-diagonal element H_{ab}, one obtains for the coupling matrix element

$$H_{ab} = \frac{\hbar}{it} \frac{I_{ba}}{I_{aa}} \tag{103}$$

where

Figure 17. Four quantum paths for electron tunneling from the heme cofactor to a Ru label in cytochochrome c (red, yellow, orange, and green) as obtained from path-integral Monte Carlo simulation. The protein is shown in stick representation in light blue and Trp14 positioned "in line of flight" is highlighted in magenta. The two redox centers are separated by 22 Å edge to edge. Reproduced with permission from ref 96. Copyright 1987 American Association for the Advancement of Science.
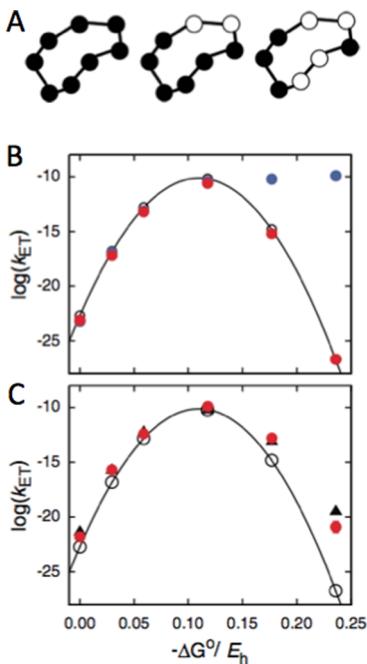
$$I_{ba} = \langle \phi_b | \exp(-i\mathcal{H}t/\hbar) | \phi_a \rangle \tag{104}$$

$$I_{aa} = \langle \phi_a | \exp(-i\mathcal{H}t/\hbar) | \phi_a \rangle \tag{105}$$

The ratio on the right-hand side of eq 103 may be obtained from imaginary-time path integral simulation of the excess electron at "time" $t = -i\hbar\beta$.[301,302]

Using path integral Monte Carlo sampling Kuki et al. generated electron tunneling paths and computed their kink free energy relative to a structureless reference system.[96] The principal result of this work was the identification of the relevant region of the protein for electron tunneling as a cylindrical zone bridging donor and acceptor. A general drawback of pseudopotential simulations is that one assumes that the ET is mediated exclusively by an excess electron or excess hole. For thermal ET reactions one can expect that both electron and hole transfer mechanisms contribute as shown in semiempirical superexchange calculations[97−99] (see also section 4.1.4), implying that multielectronic effects should generally be included. Even for photoinduced ET reactions as investigated by Kuki et al., wherein the initial state the electron is photoexcited to an energy level close to the unoccupied energy levels of the protein, the coupling mechanism is likely to involve both electron transfer to the acceptor and hole transfer to the donor. Another problem of pseudopotential-based path-integral simulation is the numerical error associated with the sampling of tunneling paths. Especially for long-range biological ET reactions the electronic coupling matrix elements are very small numbers, and one may obtain only relative values (with respect to a reference system) to useful accuracy.

5.4.2. Ring-Polymer Molecular Dynamics. In the past 10 years major advances were made by Manolopoulos, Althorpe, Miller, and co-workers in the development of ring-polymer molecular dynamics (RPMD), a variant of PIMD employing ring-shaped polymers (see Figure 18A), and ring polymer rate theory.[39,292,303,304] Key features of the RPMD method are that it yields real-time MD trajectories, preserves the exact Boltzmann distribution, and exhibits time-reversal symmetry. These properties allow RPMD to be used in combination with rare-event sampling methods for the simulation of electron tunneling events in large condensed systems containing

Figure 18. (A) Illustration of ring polymers with $n = 8$ beads and 0 (left), 1 (middle), or 2 (right) kink pairs. Beads shown in white and black correspond to electronic states $i^{(\alpha)} =$ A and B, respectively. (B), (C) Driving force dependence of ET rate for a quantized excess electron with a classical (B) and quantum description (C) of the solvent from position-representation RPMD (blue, eq 106), kinetically constrained RPMD (red, eq 106), semiclassical Marcus theory (black open circles, eq 24), and the rate equation for a quantized effective mode (black triangles, eq 30). Adapted with permission from ref 40. Copyright 2014 AIP Publishing LLC.

thousands of atoms (typically in combination with classical electronic potential). Importantly, ring polymer rate theory was developed, which allows one to rigorously compute quantum reaction rates from RPMD simulations.[39] The RPMD rate for transition through a dividing surface $\xi = \xi^{\ddagger}$, k_{RPMD}, can be expressed as a product of a quantum TST rate, k_{QTST} (= short time limit of the RPMD rate), and a time-dependent transmission coefficient, $\kappa(t)$:

$$k_{RPMD} = \lim_{t \to \infty} \kappa(t) k_{QTST} \tag{106}$$

$$k_{QTST} = (2\pi\beta)^{-1/2} \langle g_{\xi} \rangle_c \frac{\exp(-\beta A(\xi^{\ddagger}))}{\int_{-\infty}^{\xi^{\ddagger}} d\xi \, \exp(-\beta A(\xi))} \tag{107}$$

In eq 107 $\xi = \xi(\mathbf{r})$ is a suitably chosen collective variable depending on the positions of the electron in the n polymer beads, $\mathbf{q}^{(1)}, ..., \mathbf{q}^{(n)}$ and the position of the N nuclei $\mathbf{Q}_1, ..., \mathbf{Q}_N$; the latter are treated here as classical particles, $\mathbf{r} = \{\mathbf{q}^{(1)}, ..., \mathbf{q}^{(n)}, \mathbf{Q}_1, ..., \mathbf{Q}_N\}$. The free energy profile is defined as

$$A(\xi') = -k_B T \ln \langle \delta(\xi(\mathbf{r}) - \xi') \rangle + \text{const} \tag{108}$$

with the thermal average $\langle \cdots \rangle$ given by

$$\langle \cdots \rangle = \frac{\int d\mathbf{r} \int d\mathbf{v} \, \exp(-\beta \mathcal{H}_n(\mathbf{r}, \mathbf{v}))(\cdots)}{\int d\mathbf{r} \int d\mathbf{v} \, \exp(-\beta \mathcal{H}_n(\mathbf{r}, \mathbf{v}))} \tag{109}$$

The Hamiltonian of the n-bead ring polymer, $\mathcal{H}_n$, is given by the usual expression

$$\mathcal{H}_n(\mathbf{r}, \mathbf{v}) = \sum_{j=1}^{N} \frac{1}{2} M_j \mathbf{V}_j^2 + \sum_{\alpha=1}^{n} \frac{1}{2} m_e \mathbf{v}_j^2 + U_n(\mathbf{r}) \tag{110}$$

$$U_n(\mathbf{r}) = \frac{1}{n} \left[\sum_{\alpha=1}^{n} \frac{1}{2} m_e \omega_n^2 (\mathbf{q}^{(\alpha)} - \mathbf{q}^{(\alpha-1)})^2 + U_{ext}(\mathbf{q}^{(\alpha)}, \mathbf{Q}) \right] \tag{111}$$

where $\mathbf{v} = \{\mathbf{v}^{(1)}, ..., \mathbf{v}^{(n)}, \mathbf{V}_1, ..., \mathbf{V}_N\}$, M_j and m_e are the mass of the nuclei and electron, respectively, $\omega_n = n(\beta\hbar)^{-1}$ the intra-bead harmonic angular frequency, and U_{ext} is the physical potential energy of the electron due to interaction with the N nuclei (as given by a pseudopotential). An explicit expression for $\kappa(t)$ appearing in eq 106 and $\langle g_{\xi} \rangle_c$ in eq 107 is given in ref 305.

Recently, Miller and co-workers employed RPMD for direct simulation of ET between two metal ions in aqueous solution[305] using the electron–ion[139] and electron–water[306] pseudopotentials originally developed by Sprik and co-workers. A "bead-count" coordinate $\xi = f_b(\mathbf{q}^{(1)}, ..., \mathbf{q}^{(n)})$ was chosen as a collective variable to describe the progress of electron tunneling. It is equal to 1 if all electron beads are in the donor well, equal to 0 if all electron beads are in the acceptor well, and smoothly interpolates for intermediate cases when the polymer ring visits the intervening region. This high energy region was sampled using a bias potential along f_b and the weighted histogram analysis method (WHAM) for unbiasing and construction of the full free energy profile. Several simulations were carried out for different values of the driving force of the reaction. It was found that, in the normal and activationless region ($\Delta A \geq -\lambda$), the mechanism resembled closely the Marcus picture and the RPMD reaction rate eq 106 was in very good agreement with the nonadiabatic ET rate eq 24; see Figure 18B. However, the RPMD simulation did not capture the inverted region correctly ($\Delta A < -\lambda$), predicting a constant rather than a decreasing reaction rate with decreasing ΔA. This failure was traced back to the inadequate quantization of the real-time electronic state dynamics in the pseudopotential-based RPMD approach.
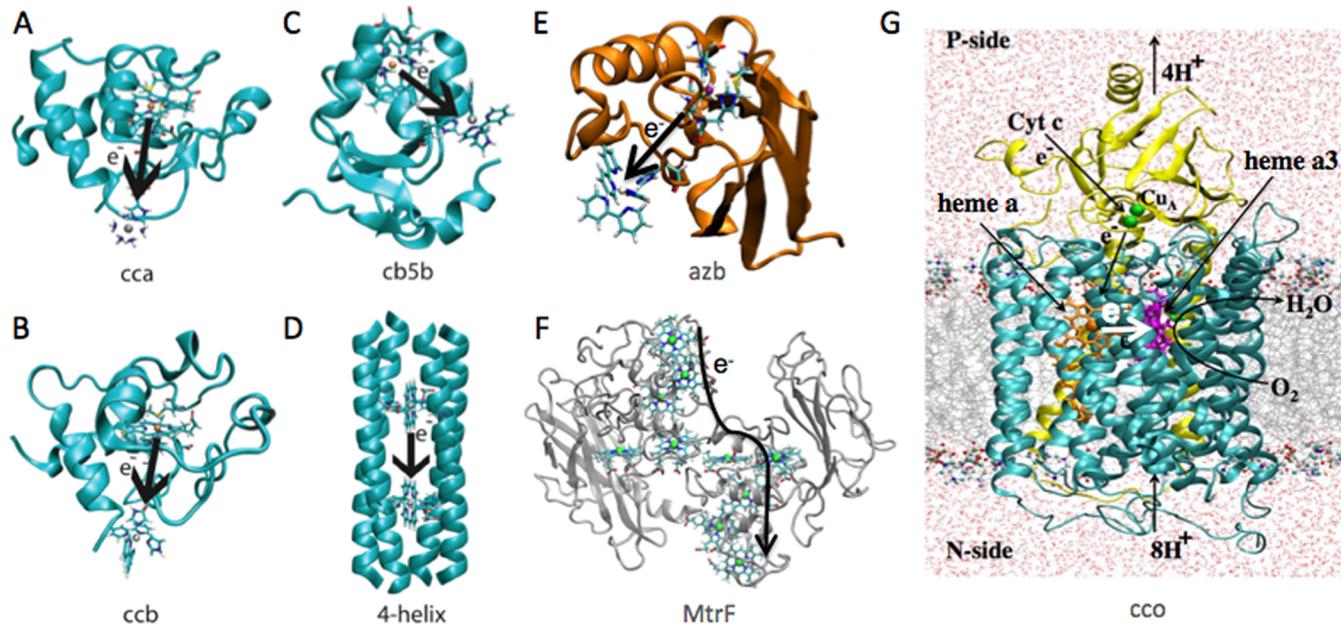
To address this problem, Miller and co-workers extended the RPMD method to allow for the description of quantized nonadiabatic, multielectron processes in large condensed phase systems.[40] The pseudopotential based position representation of the excess electron is replaced by two discrete, multielectron diabatic energies as used in Marcus ET theory. Treating the nuclei quantum mechanically (i.e., each nucleus as a ring polymer), $\mathbf{r} = \{\mathbf{Q}^{(1)}, ..., \mathbf{Q}^{(n)}\} = \{\mathbf{Q}_1^{(1)}, ..., \mathbf{Q}_N^{(1)}, ..., \mathbf{Q}_1^{(n)}, ..., \mathbf{Q}_N^{(n)}\}$, the external potential energy is given by

$$U_{ext} = -k_B T \ln \left[\sum_{\{i^{(\alpha)}\}} \prod_{\alpha=1}^{n} M_{i^{(\alpha)}, i^{(\alpha+1)}}(\mathbf{Q}^{(\alpha)}) \right] \tag{112}$$

where $i^{(\alpha)}$ denotes the electronic diabatic state of bead α, $i^{(\alpha)} =$ A or B with potential energy E_A and E_B, respectively, and $M_{i^{(\alpha)}, i^{(\alpha+1)}}$ are the elements of the matrix

$$\mathbb{M}(\mathbf{Q}) = \begin{pmatrix} \exp(-\beta_n E_A(\mathbf{Q})) & -\beta_n H_{ab}(\mathbf{Q}) \exp(-\beta_n E_A(\mathbf{Q})) \\ -\beta_n H_{ab}(\mathbf{Q}) \exp(-\beta_n E_B(\mathbf{Q})) & \exp(-\beta_n E_B(\mathbf{Q})) \end{pmatrix} \tag{113}$$

$\beta_n = \beta/n$. The sum in eq 112 is over all combinations of $i^{(\alpha)}$ including terms where $i^{(\alpha)} =$ A (or B) for all α, as well as mixed terms exhibiting adjacent bead pairs where the electronic state changes. Such changes are again referred to as "kinks" as before,

Figure 19. Structures of Ru-modified and native electron transfer proteins discussed in the main text. See Table 1 for details on the ET reactions studied and computed and experimental ET parameters. The secondary structure of Ru-modified cytochromes (A)−(C) and of a 4-helix bundle protein (D) are drawn in green. Heme cofactors and Ru complexes are shown in stick representation. Color code: H, white; C, green; N, blue; O, red; S, yellow; Fe, orange; Ru, silver. Solvent molecules are omitted. Reprinted from ref 106. Copyright 2010 American Chemical Society. (E) Ru-modified azurin secondary structure is drawn in orange. Cofactor and Ru complexes as in (A)−(D), Cu is drawn in purple, and solvent is omitted. (F) Deca-heme protein MtrF, PDB code 3PMQ. Protein secondary structure is drawn in gray, heme cofactors are shown in stick representation (green), color code as in (A)−(D), except Fe is drawn light green, and solvent is omitted. (G) Snapshot of an MD simulation of cytochrome *c* oxidase embedded in a membrane. Protein secondary structure of the two subunits is drawn in green and yellow, heme cofactors are shown in stick representation in orange and magenta, lipid tails are in gray, and color code of atoms of lipid head groups as in (A)−(D). Both sides of the membrane are solvated with water. Adapted from ref 231. Copyright 2012 American Chemical Society.

but now in diabatic electronic state space; see Figure 18A. Thus, the external potential eq 112 provides a mean field description of the electronic degrees of freedom for the classical dynamics of the nuclear ring polymer. To describe the progress of the ET reaction, a continuous auxiliary variable was introduced as a collective coordinate ($\xi = y$ in ref 40)). The collective coordinate interpolates between configurations with all beads in diabatic state A ($y \approx 1$), with beads forming kink pairs ($y \approx 0$) and with all beads in diabatic state B ($y \approx -1$).

In this picture, the overestimation of the ET rate in the Marcus inverted regime is due to an overestimation of kinked ring-polymer configurations across nondegenerate diabatic energies. To address this deficiency, the authors augmented the external potential eq 112 with a penalty function that reduces the statistical weight of kinked and nondegenerate configurations. The resultant method denoted "kinetically restrained RPMD" was applied so far to model systems and showed promising first results.[40] In particular, it reproduced correctly the Marcus inverted regime for both quantum and classical nuclei; see Figure 18C. The method may prove useful for future simulation of nonadiabatic ET reactions in condensed phase systems including biomolecules, especially at low temperatures where nuclear quantum effects become important.

6. SELECTED APPLICATIONS

6.1. Ru-Modified Proteins

6.1.1. Reorganization Free Energies. Recently, my co-workers and I reported computed λ values for a number of proteins including Ru-modified cytochromes[105,106] and azur-

ins,[253] a designed 4-helix bundle protein,[106,230] cytochrome *c* oxidase (cco),[231] and a deca-heme cytochrome (MtrF);[307] see Figure 19 for protein structures. All calculations were carried out according to the QM + MM scheme of Figure 9. The results are compiled in Table 1. The total reorganization free energy was found to range from about 0.5 eV for ET deep inside the membrane protein cco to 0.7−1.1 eV for ET between cofactors of smaller proteins that are partly solvent exposed, to 1.4 eV for proteins where at least one redox active group is fully solvent exposed. The calculated values are broadly consistent with the few experimental estimates that are available although in some cases there are significant deviations as I discuss further below. The range of λ values in natural proteins is therefore about 1 eV, corresponding to a variation in ET rate of about 4 orders of magnitude (at $\Delta A = 0$). This is significant, but less than the variations in rate due to electronic coupling/distance, spanning about 9 orders of magnitude.[176]

6.1.2. Inner- and Outer-Sphere Contributions. The total λ is often divided into an inner-sphere contribution due to cofactors and first shell ligands and an outer-sphere contribution due to the protein and solvent. Typical biological cofactors are rather rigid exhibiting only small changes in bond lengths and/or coordination number in response to oxidation/reduction. Hence, inner-sphere reorganization energy is usually rather small, about 0.05−0.15 eV for proteins involving heme cofactors[105,230,231] and about 0.2 eV for Cu proteins.[239,251,253] The theoretical estimates for hemes is broadly consistent with estimates obtained from photoelectron spectroscopy, 0.12−0.14 eV for ET in a Zn-porphin dimer.[308]

The largest contribution by far is the outer-sphere reorganization free energy. For proteins with solvent accessible

Table 1. Reorganization Free Energies (λ) and Rate Constants (k_{ET}) for ET Reactions in Proteins and between Aqueous Ions[a]

ET reaction	abbrev	λ(comp)[b]	λ(exp)	p[c]	χ_G[d]	k_{ET}(exp)
Proteins						
$Ru^{2+} \to Fe^{3+}$ cyt c-His33Ru(NH$_3$)$_5$[e]	cca	1.34	1.15−1.24[f]	1.7	1.1	3.0×10^1[f]
$Cu^+ \to Ru^{3+}$ azurin-His83Ru(bpy$_2$)(im)[g]	azb	1.31	0.80[h]	1.6	1.1	1.2×10^6[h]
$Fe^{2+} \to Ru^{3+}$ cyt c-His33Ru(bpy)$_2$(im)[e]	ccb	1.26	0.74[i]	1.5	1.1	2.6×10^6[i]
$Fe^{2+} \to Ru^{3+}$ cyt b_5-His26Ru(bpy)$_2$(im)[e]	cb5b	1.17	–	1.6	1.1	–
$Fe^{2+} \to Fe^{3+}$ 4-helix bundle-(porphyrin)$_2$[e]	4-helix	0.94	–	1.7	1.1	–
$Fe^{2+} \to Fe^{3+}$ deca-heme cytochrome MtrF[j]	MtrF	0.75−1.13	–	1.4	0.7[k]	–
$Fe^{2+} \to Fe^{3+}$ cco heme a-heme a_3[l]	cco	0.57	–	1.5	1.0[k]	7.1×10^8[m]
$P^* \to B_L$ bacterial reaction center[n]	rc	0.36[n]	0.22[o]	–	–	3.2×10^{11}[p]
$B_L^- \to H_L$ bacterial reaction center	rc	0.36[n]	0.22[o]	–	–	1.6×10^{12}[p]
Aqueous Ions						
$Ru_{aq}^{2+} + Ru_{aq}^{*3+} \to Ru_{aq}^{3+} + Ru_{aq}^{*2+}$		1.78[q]	1.7−1.8[r]	1.1[s]	–	2.0×10^1[t]
$(Ru(bpy)_3^{2+})_{aq} \to (Ru(bpy)_3^{3+})_{aq} + e^{-}$[u,v]		1.24	1.21	–	–	–
$Mn_{aq}^{2+} \to Mn_{aq}^{3+} + e^{-}$[u,w]		3.09	2.98	–	–	–
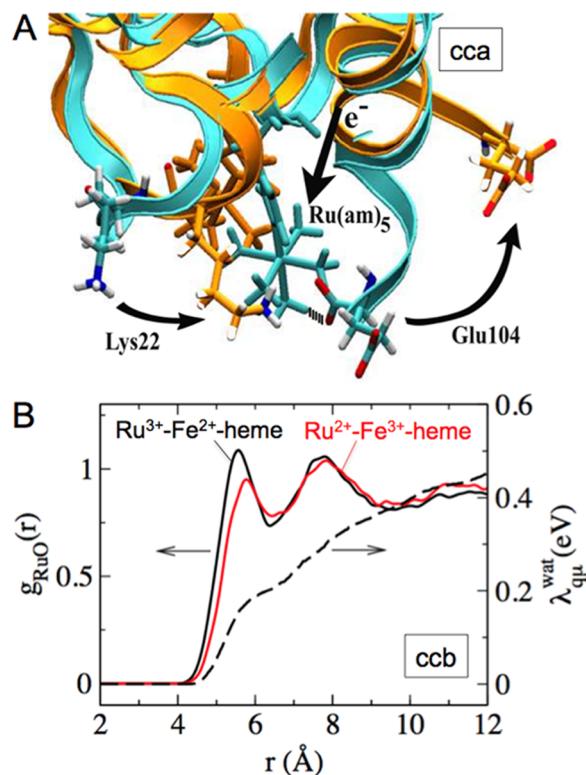
[a]All energies are in eV and all rate constants in s^{-1}, unless stated otherwise. All values are for aqueous solutions except cco, and rc which are embedded in a solvated membrane. See Figure 19 for protein structures. In the main text the proteins are referred to by their abbreviated name (abbrev); (comp) stands for computed and (exp) for experimental. [b]Obtained according to eq 54 with energy gaps computed according to the QM + MM scheme (Figure 9) using the electronically polarizable AMBER02 force field[362] and POL3 water model,[314] unless stated otherwise. The superscript "st" in eq 54 is omitted for simplicity. [c]$p = \lambda^{np}_o/\lambda_o$; ratio between outer-sphere reorganization free energy obtained with the electronically nonpolarizable (np) AMBER99 force field[362] and TIP3P water,[363] λ^{np}_o, and the outer-sphere reorganization free energy λ_o obtained with the polarizable force field as described in footnote b. [d]Nonergodicity parameter eq 99 for outer-sphere reorganization free energy. [e]Reference 106. [f]Reference 312. [g]Reference 253. [h]Reference 313. [i]Reference 227. [j]Reference 307. Range of λ values for nine heme−heme ET reactions in MtrF using the crystal structure termed "final" as initial coordinates. p is the average over all nine ET reactions obtained for the crystal structure termed "preliminary" as initial coordinates. [k]λ was obtained by calculating the energy gap with the AMBER02 force field and POL3 water on trajectories generated with AMBER99 force field and TIP3P water. This slight inconsistency is likely to be the reason for $\kappa \leq 1$. [l]Reference 231. [m]Reference 72. [n]References 233 and 234. Obtained according to eq 85. See ref 233 for details on force field and simulation protocol. [o]Estimated from experimental data. Taken from Figure 4 of ref 24. [p]Reference 364. [q]Reference 198. Value for 5 M ionic strength and a Ru−Ru separation distance of 5.5 Å. [r]Range of values for which the computed rate reproduces the experimental rate. [s]Reference 309. [t]Reference 365, in units of s^{-1} M^{-1}. [u]Reorganization free energy for one-electron oxidation. [v]See Supporting Information of ref 150. [w]Reference 151. Value obtained as explained in Table 2 of ref 106.

redox groups the contributions of the solvent and protein were found to be highly dependent on the specific protein/water environment of the redox group. For instance, for cyt c-His33Ru(am)$_5$ (cca) it was found that most of the outer sphere reorganization free energy is due to charged protein residues close to the Ru complex; see Figure 20A.[106] In this specific example positively charged Lys22 is pulled toward and negatively charged Glu104 away from the Ru complex upon reduction of the metal center. The extent of such responses depends on the flexibility and length of the side chain and the flexibility of the protein backbone. Being the N-terminal residue, Glu104 exhibits a particularly high flexibility accounting for almost a third of the total reorganization free energy according to MD simulations.[106] The situation is rather different for cyt c-His33Ru(bpy)$_2$(im)(ccb).[106] It was found that solvent reorganization around the Ru complex accounts for more than three-quarters of the total λ. Upon electron injection in the Ru complex, the distance between the metal and the first solvation shell slightly increases (see Figure 20B) due to the smaller net charge on the metal.

If no information from experiment or computation is available, a reasonable first guess is to assume that protein and water contribute to about equal amounts to outer-sphere reorganization.[106,233,234] Protein reorganization can be generally viewed as a collective effect including many residues, each of which contributes a small fraction (Glu104 and Lys22 in the above example is somewhat of an exception in this respect). As one would expect, charged residues usually give the largest contributions even if they are relatively far away from the redox active site due to weak dielectric screening by the protein frame, followed by residues with dipolar side chains. This led us to the

conclusion that reorganization free energy may in general not be effectively controlled by single point mutations, but may be controlled to a large extent by the degree of solvent exposure of the ionizable cofactors.[106]

6.1.3. Importance of Electronic Polarizability. The relatively good agreement with experiment is a consequence of using an electronically polarizable force field for the calculations of λ. The outer-sphere reorganization free energy is strongly overestimated if standard, electronically nonpolarizable protein force fields and water models are used (see column with header "p" in Table 1). The reason for this is well-known.[77,105,114,142,255,309] In Marcus' continuum theory for ET, the outer-sphere reorganization free energy, λ_o, is proportional to the Pekar factor of the medium surrounding the cofactors, $\lambda_o \propto (1/\epsilon_{op} - 1/\epsilon_s)$, where ϵ_{op} and ϵ_s are the optical and static dielectric constants of the medium, respectively. In electronically nonpolarizable molecular models the atomic charges are typically adjusted so as to reproduce ϵ_s or properties that depend on ϵ_s, but since the atomic charges are fixed $\epsilon_{op} = 1$. In contrast, the experimental optical dielectric constants of water and aqueous protein solutions are $\epsilon_{op} \approx 1.8$.[105,310] Thus, if $\epsilon_s \gg \epsilon_{op}$, which is usually the case for protein solutions, one can expect that λ_o is overestimated with nonpolarizable force fields by a factor equal to 1.8 (45%). This should be compared to an average ratio λ_o(nonpol)/λ_o(pol) = 1.6 (37%) obtained from simulation. The (small) deviation indicates that the continuum model predicts a slightly too strong dependence of reorganization free energy on the optical dielectric constant, in agreement with other theoretical studies.[311]

Figure 20. (A) Protein response to ET in cca. Two snapshots of the protein were selected randomly and aligned: one from a trajectory in the initial ET state (green) and one from a trajectory of the final ET state (orange). Protein residues that contribute more than 0.1 eV to the total reorganization free energy are depicted in stick representation. (B) Solvent response to ET in ccb. Radial distribution functions, $g_{RuO}(r)$, are shown between the Ru atom of the Ru(bpy)$_2$imHis33 complex of ccb and the oxygen atoms of solvent water molecules. The distribution for the initial ET state (Ru^{3+}) is shown in black solid lines, and the distribution for the final ET state (Ru^{2+}) is shown in red lines. The integrated reorganization free energy of water molecules, $\lambda_{q\mu}^{wat}$, is shown in dashed lines. See Figure 19A for the protein structure. Reprinted from ref 106. Copyright 2010 American Chemical Society.

6.1.4. Comparison with Experiment. The computed reorganization free energy for cyt *c*-His33Ru(NH$_3$)$_5$ was in very good agreement with experiment,[312] but the calculated values for cyt *c*-His33Ru(bpy)$_2$(im) and azurin-His83Ru(bpy$_2$)(im)[227,313] were about 0.5 eV higher than experimental estimates. In the MD simulations, most of the reorganization free energy was found to be due to water surrounding the Ru(bpy)$_2$(im) group (see discussion above). Thus, a first possible explanation for this discrepancy could be that the polarizable water model (POL3[314]) underestimates electronic polarization effects, as was noted in ref 315. However, work on aqueous transition metal ions suggests that this is not a likely reason for the discrepancy. Employing the same QM + MM approach as in the protein simulations, reorganization free energies for oxidation of aqueous Ru(bpy)$_3$$^{2+150}$ (and aqueous Mn^{2+151}) were obtained in excellent agreement with experimental estimates from photoemission spectroscopy[150,151] and with results from all-atom density functional based molecular dynamics simulation[150] (values given in Table 1). Moreover, the reorganization free energy for electron self-exchange between two aqueous Ru ions could be calculated in excellent agreement with experimental data.[198] Thus, given that the

solvent response in aqueous Ru(bpy)$_3$$^{2+}$ could be well described in ref 150, the large deviation for the two Ru(bpy)$_2$(im) labeled proteins is surprising.
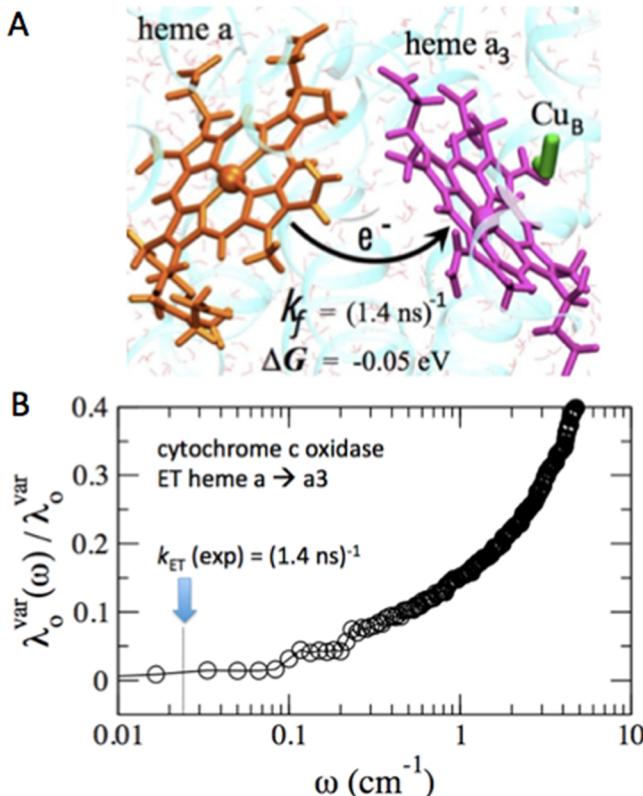
At this point one should perhaps also consider possible uncertainties of the experimental estimates. An impressive effort was made by Gray and co-workers to measure ET rates for a large number of Ru-modified proteins. Using high potential Ru complexes, the Marcus inverted region could be accessed for these proteins for the first time. Yet, the experimental λ value for cyt *c*-His33Ru(bpy)$_2$(im) was obtained from a fit to data containing only a single point that is clearly in the inverted region.[227] The data for azurin-His83Ru(bpy$_2$)(im) did not contain a point that is clearly in the inverted region, but the λ value obtained from the driving force dependence was consistent with an estimate from the temperature dependence of the ET rate.[313] Though, the temperature method is subject to some uncertainties as discussed by Moser and Dutton.[176] Most surprisingly, experimental measurements on Ru-modified azurin in aqueous solution[313] and in protein crystals[316] gave similar reorganization free energy estimates (0.8 eV), which led to the conclusion that solvent reorganization free energy is vanishingly small. This is rather surprising because the electron-accepting Ru complex is solvent exposed in the solution phase experiments and the ET rate is sufficiently slow (microseconds, see Table 1) so that the full dielectric response of water (subnanoseconds) is expected to contribute to the activation barrier. Hence, in order to help resolve the controversy between experiment and computation, it would be of interest to also reinvestigate and possibly extend the set of experimental data that were used for determination of λ values in these proteins.

6.2. Cytochrome *c* Oxidase

6.2.1. Enzyme Function. Cytochrome *c* oxidase (cco, or complex IV, Figure 19G) is located in the inner mitochondrial membrane and catalyzes the reduction of molecular oxygen, the terminal step in cellular respiration. The chemical energy released is converted into a proton gradient[4] that drives the synthesis of ATP in the terminal complex of the respiratory chain, complex V. Given the high significance of cco to any oxygen consuming organism, it is desirable to understand its working principles qualitatively and quantitatively on a molecular level of detail. A large bulk of experimental studies on cco exists including crystal structures,[317−320] mutation experiments,[110,111,321−323] kinetics,[72,109,324−326] and spectroscopic measurements.[327−329] Also many theoretical modeling studies[181,330−332] and molecular simulations[231,333−338] have been carried out. This has given valuable insight into many key features of cco such as the nature of the cofactors, the conserved residues, and intermediates, as well as the nature of proton channels (recently reviewed in ref 339), electron transfer pathways, and proton pumping mechanism (recently reviewed in ref 66).

6.2.2. Heme *a* → Heme *a*$_3$ ET: 20+ years of Controversy. With regard to ET reactions in cco, one of the issues that has been much debated is the kinetics of the terminal electron tunneling step from heme *a* to heme *a*$_3$; see Figure 21A. As mentioned in section 2, an ultrafast tunneling rate was reported for heme *a* → heme *a*$_3$ ET, k_{ET}(exp) = 7 × 10^8 s^{-1} = (1.4 ns)$^{-1}$, and a very small driving force of ΔA = −0.05 eV. The high rate for heme *a* → heme *a*$_3$ tunneling is unusual in the sense that it is at least 3 orders of magnitude faster than typical ET times in proteins,[24,26] exceeded only by

Figure 21. (A) Heme a to heme a_3 ET reaction in cytochrome c oxidase (cco) with experimentally determined parameters indicated.[72,110] Adapted from ref 231. Copyright 2012 American Chemical Society. (B) Integral of the spectrally resolved outer-sphere reorganization free energy (eq 114) divided by the total outer-sphere reorganization free energy as a function of the upper integration limit ω. The analysis was carried out using the data from ref 231. The arrow indicates the experimental reaction rate constant on the scale of inverse centimeters.

the picosecond charge separation event occurring in photosynthetic reaction centers. It was argued that ultrafast reduction of heme a_3 could help increase the chances of trapping O_2 since oxygen only binds to the reduced form,[72] thereby facilitating respiration especially under conditions where oxygen is a limited resource, for example, at low atmospheric pressure.

The search for a possible microscopic explanation for ultrafast tunneling between heme a and a_3 has divided the community for many years. In the Marcus picture, the high ET rate is due either to large electronic coupling between the two cofactors (H_{ab}) or small activation free energy, that is, small reorganization free energy (λ), or a favorable combination of both parameters. Early empirical predictions based on the Moser–Dutton ruler[24,25] were consistent with a nanosecond rate if a reorganization free energy as high as 0.7 eV was assumed.[176] The activation free energy corresponding to this value ($\Delta A^{\ddagger} = (\lambda + \Delta A)^2/(4\lambda) = 0.15$ eV at 300 K) is in apparent contrast with the results of temperature-dependent rate measurements, which show that the rate remains almost unchanged in the temperature range 277–308 K.[110] Semi-empirical calculations of electronic couplings[181] and molecular dynamics estimates of reorganization free energy[338] have further supported the notion that heme a to a_3 tunneling is almost activationless and should be described by λ values as low as 0.2 eV ($\Delta A^{\ddagger} = 0.03$ eV). Such low values are highly unusual for thermal ET in proteins and are surprising indeed if one

bears in mind that the reorganization energy of only two heme groups makes already a contribution of about 0.1 eV (see section 6.1).

The mechanism for ultrafast ET between the two hemes has been revisited recently in a large-scale MD simulation study of cco embedded in a membrane (see Figure 19G).[231] The reorganization free energy was computed again according to the QM + MM scheme using the same electronically polarizable force field as for the Ru-modified proteins above. Importantly, the length of the MD trajectories generated was about equal to the experimental time constant of the ET reaction ($\approx$1–2 ns), so as to avoid sampling of protein motions that are slower than the ET reaction, in accord with section 5.2.1 and eq 85. The energy gap fluctuations were spectrally resolved according to eq 60 from $k_{ET}(\exp) \approx k = 0.02$ cm^{-1} to 10 cm^{-1} (corresponding to time constants of 1.7 ns to 3 ps), and integrated according to eq 114.
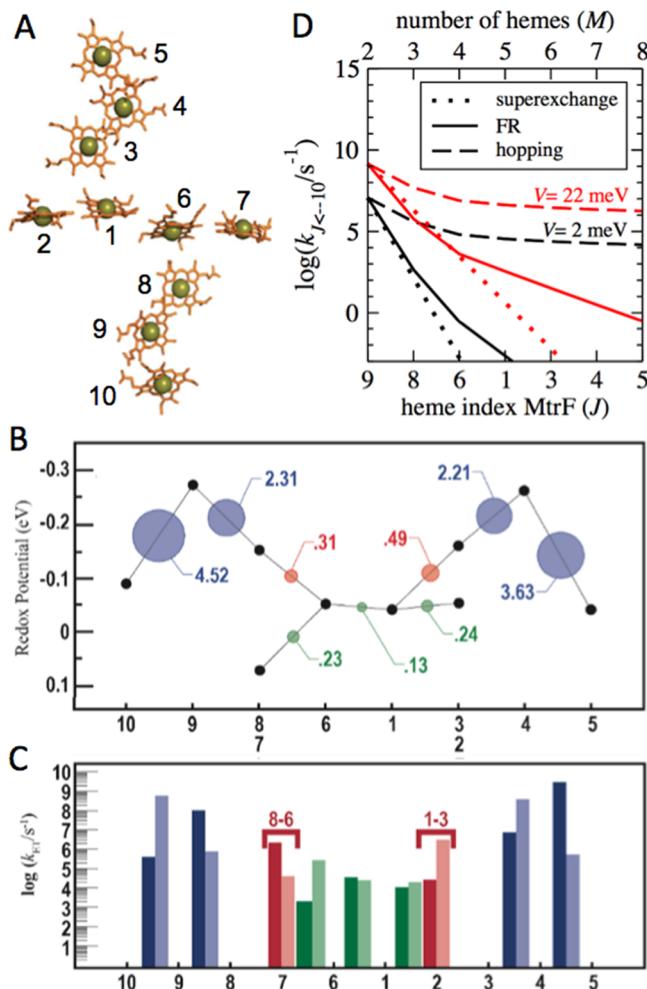
$$\lambda_o^{var}(\omega) = \frac{2}{\pi} \int_k^{\omega} d\omega' \frac{J(\omega')}{\omega'} \qquad (114)$$

As one can see in Figure 21B, most of the reorganization free energy occurs in this spectral region. The total value obtained $\lambda_o^{var} = \lambda_o^{var}(\omega \to \infty) = 0.42$ eV was to within numerical uncertainties identical with the outer sphere reorganization free energy estimated from the Stokes shift, $\lambda_o^{var} = \lambda_o^{st}$. A breakdown of the latter into components of the system gave contributions of 0.31 eV from collective protein reorganization and 0.11 eV from solvent reorganization on either side of the membrane. Adding the inner sphere contribution from DFT calculations (0.15 eV), a total reorganization free energy of $\lambda = 0.57$ eV was reported.

This latest estimate for λ is somewhat closer to the generic 0.7 eV assumed by Moser and Dutton than the 0.2 eV suggested by Jasaitis et al. and Kaila et al. The deviation with respect to the estimate by Kaila et al. is rooted in the different simulation method and analysis protocol as discussed in detail in ref 231. In ref 231 it was also argued that the small but significant barrier obtained, $\Delta A^{\ddagger} = 0.12$ eV, is in agreement with the weak temperature dependence observed in experiment if one allows for only a very minor increase in the donor–acceptor distance as the temperature is increased. Thus, according to these latest results, the ultrafast tunneling reaction is most likely due to a small, but not unusually small reorganization free energy in combination with relatively strong electronic coupling between the two hemes.

6.3. Multiheme Proteins

6.3.1. Function and Applications. Multiheme cytochromes are defined by the presence of two or more c-hemes positioned to facilitate heme-to-heme electron tunneling. Some of these proteins bind up to 10 or more heme groups forming conductive wires ("biological nanowires") on the 1–10 nm scale; see, e.g., Figure 22A. Multi-heme proteins have attracted much interest recently, due to their key roles in mediatorless microbial fuel cells,[340,341] decontamination of water and soil containing radioactive isotopes such as U(VI) and Tc(VII),[342] as well as for the promise they hold out for bionanotechnological applications.[23] The first crystal structure of a deca-heme protein was solved in 2011 (MtrF)[257] and the structure of two homologues, UndA[343] and MtrC,[344] followed. Their redox properties were characterized using spectroelectrochemical methods,[83,345] and the kinetics for ET through MtrC (a homologue of MtrF) onto an iron oxide nanoparticle was

Figure 22. (A) Heme arrangement in the deca-heme protein MtrF, PDB code 3PMQ.[257] The porphyrin units are drawn in orange and the Fe atoms in green. Adapted with permission from ref 347. Copyright 2015 The Royal Society. (B) Computed redox potentials of the heme cofactors vs standard hydrogen electrode[254] and root-mean-square average electronic couplings[178] for each pair as indicated by circles with radius proportional to V. The horizontal axis refers to the heme index defined in (A). Numerical values for V are indicated in units of meV. (C) Heme-to-heme hopping rate constants k_{ET} in MtrF for the forward direction (heme 10 → 5, full colors) and for the backward direction (heme 5 → 10, shaded colors). Each bar indicates the rate constant between the two hemes denoted at the base to the left and to the right of the bar unless indicated otherwise. Figures in (B) and (C) are reprinted with permission from ref 178. Copyright 2014 National Academy of Sciences. (D) Comparison of three different mechanisms for ET in MtrF: superexchange (SE), flickering resonance (FR), and hopping. The simple donor−bridge−acceptor model of Figure 11 is adopted with equal bridge site energies, and equal reorganization free energies and couplings between each heme pair. The rate constant for ET from heme 10 to heme J, $k_{J\leftarrow10}$, is calculated according to eqs 69, 78, and 81 for the following ET parameters: $\lambda = 0.9$ eV,[307] $\Delta A_{BD} = 0.13$ eV, and $\Delta A = 0$. Lines in black are for an average value of electronic couplings as obtained from QM(FODFT)/MM electronic structure calculations[178] ($V = 2$ meV), and lines in red are for an average value for electronic couplings obtained from the empirical Moser−Dutton ruler ($V = 22$ meV, see section 4.1.1). The horizontal axis at the bottom of the panel indicates the heme index shown in (A) and the horizontal axis at the top of the panel indicates the total number of hemes in the chain, comprised of heme 10, heme J, and $M − 2$ bridging hemes. Note that for $M = 2$ the rate ($k_{9\leftarrow10}$) is trivially identical for all three mechanisms.

investigated.[8] Moreover, single-protein conductive AFM and STM measurements were carried out for MtrC[88,346] and MtrF,[88] reporting nanoampere currents at modest bias voltages. Much of our current knowledge on the molecular structure and function of multi-heme proteins was recently reviewed.[347] Here I summarize some of the molecular simulations that have been carried out to help understand the mechanism of ET in these proteins.

6.3.2. Thermodynamics of ET. The assignment of measured (macroscopic) redox potentials to individual hemes is challenging in c-type multi-heme cytochromes because each heme is chemically identical. Recently, MD simulations were carried out and the (microscopic) redox potentials of the 10 hemes of MtrF computed to assist with the assignment.[254] The redox potentials obtained are shown in Figure 22B (black circles). The profile is to a good approximation symmetric with respect to the center of the protein between hemes 6 and 1. This implies that ET along the wire is not a steady downhill process as one might anticipate, but a reversible process, with no or very small dissipation of free energy. Transport is then driven by the redox gradient set by the external electron donor or acceptor. In this sense, the protein indeed acts like a "wire" conducting electrons upon application of a voltage.

6.3.3. Kinetics of ET. Electronic coupling matrix elements for heme-to-heme ET were calculated in a following study[178] using the FODFT ($2N$) approach[169] (similar to the FODFT-($2N − 1$) method of section 4.1.8), in combination with a QM/MM calculation of the orbitals. The couplings averaged over nanosecond MD trajectories are shown in Figure 22B in colored circles with radiuses proportional to their magnitude. It was found that electronic coupling is strongest between heme pairs for which ET is most endergonic (ET to hemes 9 and 4). This led to the conclusion that the protein has evolved to harbor low potential hemes without slowing down ET rates, by placing them in a stacked configuration with neighboring hemes, where electronic interaction is strongest. In this way, the large activation barrier due to low redox potential is fully or at least partly compensated.

The ET parameters were converted in heme-to-heme ET rates, shown in Figure 22C. Assuming that ET through the protein occurs via consecutive heme-to-heme electron hopping, the hopping rates were inserted in a Master equation to obtain the electron flux through the protein (see paragraphs below for a justification of the hopping mechanism). On this basis it was predicted that MtrF supports a maximum flux of 10^4−10^5 electrons per second in aqueous solution, an estimate that remains to be confirmed by solution phase kinetic experiments. Interestingly, this is orders of magnitude smaller than the single-molecule currents measured in conductive AFM and STM experiments.[88,89] The presence of an external potential bias and/or the significantly reduced solvation of the protein in the AFM experiments may give rise to a conduction mechanism that is different from the hopping mechanism probed in solution kinetics experiments. An explanation of the relatively high currents measured in AFM experiments is still outstanding.

6.3.4. Validity of ET Rate-Based Approaches. In light of the recently developed theoretical concepts discussed in section 5, I would like to review possible mechanisms for ET in MtrF. The above estimate for the electron flux through MtrF was obtained by assuming that the relevant ET states in MtrF are localized on single heme units, specifically, the t_{2g} d-orbital manifold of the low-spin c-type hemes, and that the ET

between states on different hemes can be described by electron hopping between neighboring hemes with the usual non-adiabatic ET rate eq 24. As I discuss in the following, the conditions for application of rate-based approaches are indeed met for the solvated protein.

The computed values for reorganization free energy for ET between the hemes are significant, in the range 0.7–1.1 eV[307] as obtained from 10 ns long MD simulations (see Table 1), while electronic coupling matrix elements are about 3 orders of magnitude smaller, ranging from $(\langle|H_{ab}|^2\rangle)^{1/2} = 0.1$ to 4 meV. This shows that the heme-localized electronic states are low energy states ("traps") that are separated by sizable activation barriers of 0.2–0.3 eV ($\approx 10k_BT$ at 300 K). With the activation barriers being large compared to k_BT, an excess electron initially localized on a given heme will be relatively long-lived compared to the vibrational modes coupling to ET. Rare thermal fluctuations will initiate ET leading to formation of the final state via a specific mechanism (e.g., SE, FR, or hopping, see section 6.3.5). Importantly, the computed transition times for nearest neighbor electron hopping are less than 0.1 ns (except for two nanosecond transitions between hemes 4, 5 and 10, 9), indicating that the nonergodicity correction eq 85 for the λ values is not necessary. Moreover, the reorganization free energies obtained from the Stokes shift and from the gap fluctuations are very similar, indicating that the fluctuations are Gaussian. Therefore, the calculations indicate that three important conditions for rate-based models such as SE, FR, and hopping are satisfied, that is, (i) localization of charge carriers on single hemes in initial and final states, (ii) sufficiently slow rates so that equilibrium statistical mechanics remains valid, and (iii) Gaussian statistics of the energy gap.

6.3.5. Super Exchange, Flickering Resonance, or Hopping? I have evaluated the rates for SE, FR, and hopping according to eqs 69, 78, and 81 and have chosen effective ET parameters as follows: $\lambda = 0.9$ eV and $V = \langle H_{ab}^2\rangle^{1/2} = 2$ meV from MD simulations and FODFT calculations (see above), averaged over the seven heme–heme ET reactions along the octa-heme chain. The net free energy change for ET along the octaheme-chain $\Delta A_{5\leftarrow10} \approx 0$ according to MD simulations, and the free energy difference for ET from the donor to the bridge states was chosen to be $\Delta A_{BD} = 0.13$ eV. The latter value is close to the computed redox potential difference between the donor (heme 10) and the first bridge site (heme 9, $\Delta A_{9\leftarrow10} = 0.19$ eV). A slightly smaller barrier was chosen so as to reproduce the flux through the octa-heme chain (1.5×10^4 s^{-1}) as obtained by solving a master equation for electron hopping along the octa-heme chain using the seven as-calculated heme–heme ET rates (see above). The particular choice for ΔA_{BD} is not very important here, as the main conclusion remains the same when this parameter is varied.

The results are shown in Figure 22D. One finds that hopping dominates over both SE and FR for any number of hemes (black lines). The reason for the relatively fast decay of the SE and FR rates relative to hopping is the small electronic coupling between the heme groups. Increasing V to 22 meV, the coupling value at van der Waals distance (3.6 Å) according to the Moser–Dutton ruler (see section 4.1.1), the decay for SE and FR is less steep but the rates are still significantly below the hopping rate. Rather large coupling values in excess of 100 meV, more typical for charge transfer in DNA, are necessary so that FR and SE can compete with hopping at short distances. These results are not unexpected, of course, because of eq 83. The same caveats of the donor–bridge–acceptor model used
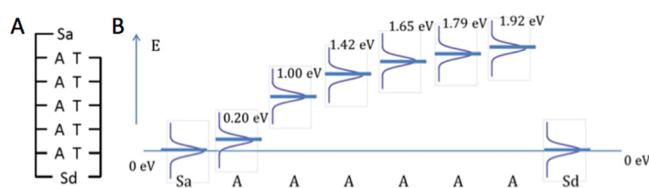
to derive this relation also apply here. However, in view of the very clear advantage of hopping over FR as a consequence of the small coupling values, it is very unlikely that the qualitative picture will change if more refined models for the FR mechanism become available.

6.4. DNA

6.4.1. Brief Survey. Hole transfer in DNA has been the subject of a large number of experimental and computational studies for the last 15 years (see refs 37 and 38 for recent reviews from a computational perspective). Nevertheless, important issues regarding the degree of charge localization, adiabaticity, medium effects, time-scale separations, and the details of the hole transfer mechanism as a whole are still under debate. It is now widely agreed that a bandlike mechanism does not exist,[38,348] at least under ambient conditions, because of thermal disorder and solvent effects, when present. The experiments of Giese and co-workers[121] and Lewis and co-workers[73] on the distance dependence of the charge transport rate in DNA strands were interpreted in terms of one-step superexchange tunneling for short distances (up to three[121] and one A–T base pairs,[73] respectively) and multistep hopping for longer distances; see also section 2. Recognizing the importance of the dielectric environment in dynamically modulating the site energies, the charge carrier in DNA was also described as a polaron.[123,349,350] (This term originates from solid state physics and refers to a charge that is localized due to local lattice distortions, corresponding to the stabilization of of charge by relaxation of solvent dipoles in the current context.) It constituted the basis of, for example, the phonon-assisted polaron-gated[349] and polaron drift models.[123] The possible existence of polarons was supported by the studies of sequence-dependent transfer.[350]

6.4.2. Superexchange or Flickering Resonance at Short-Range? In a recent study, Beratan, Skourtis, and co-workers reexamined the distance dependent rate measurements of Giese and co-workers[121] and Lewis and co-workers,[73] in particular the interpretation that short distance charge transfer occurs via SE tunneling. The authors applied the FR model to both sets of experimental data, charge shift[121] and charge separation[73] across A–T strands using parameters from molecular simulations.[351] A schematic of the stilbene capped DNA hairpin of ref 73 is shown in Figure 23A, and the corresponding model used for the FR calculations is shown in Figure 23B. Note the formation of a Coulomb ramp along the energy levels of the base pairs as a consequence of the energetics for charge separation.

The distance dependence of the computed matching probabilities eq 74 was found to correlate well with the
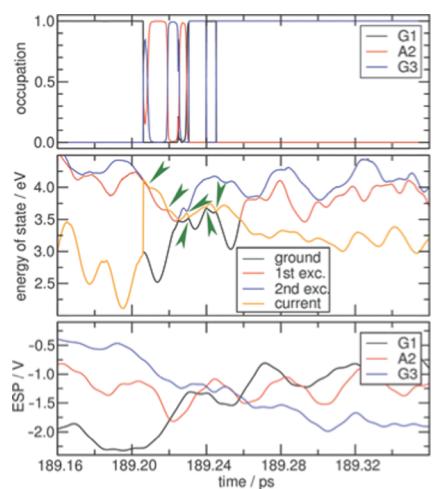
Figure 23. (A) Structure of a DNA hairpin (A, T), capped with stilbene donor (Sd) and acceptor (Sa) groups. Adapted from ref 73. Copyright 2006 American Chemical Society. (B) Coulomb ramp energetics used in the flickering resonance model for ET in a stilbene capped DNA hairpin. Reprinted with permission from ref 35. Copyright 2014 National Academy of Sciences.

measured exponential distance dependence over one, two, and three bridging A−T base pairs for both charge shift and charge separation experiments. Hence, the FR model could reconcile the contradicting experimental results of exponential distance decay (SE type) and relatively long-lived charge populations on the bridge (hopping type). In light of the present analysis of the FR model for a simple model system (specifically eqs 82 and 83), it would be of interest to compare the FR rate to the hopping and SE rates using the same parameters for all three models. Moreover, it would be of interest to see if the FR mechanism for these particular systems is also predicted by the direct charge propagation NAMD methods developed by Elstner and co-workers (see sections 5.2.3 and 6.4.3).

6.4.3. NAMD Simulations. The above-mentioned NAMD implementation based on SCC-DFTB was applied to simulate the transport of an excess hole in a solvated homogeneous DNA sequence AAAA (A for adenine) and for a heterogeneous sequence GAG (reviewed in refs 37 and 38). Both mean field Ehrenfest (MF) and surface hopping (SH) NAMD simulations were carried out. For AAAA, where all site levels are similar in energy, the MF simulations gave a strongly delocalized excess charge, which is likely to be an artifact of the mean field approach as discussed in section 5.2.3. In the SH simulation the hole was mostly localized on a single A and the next-neighbor transfer rate obtained (100 ns^{-1}) was an order of magnitude higher than in experimental measurements. The SH simulations did not include a correction for the missing electronic decoherence in the standard SH algorithm (see section 5.2.3), and inclusion of a decoherence correction may further improve the agreement with experiment.

For GAG, where the energy landscape is no longer flat, MF and SH simulations gave a similar picture, both in terms of charge localization and transfer rates (3−4 ns^{-1}). A typical crossing event from the first G base (G1) to A and from A to the second G base (G2) is shown in Figure 24. Thermal fluctuations bring the adiabatic ground state in energetic

Figure 24. Surface hopping (SH) simulation of hole transfer in a GAG oligonucleotide. A passage through the high-coupling region is shown. Top panel: occupation of the nucleobases by the wave function of the excess hole. Middle panel: energy of the adiabatic states. The active state that determines the nuclear dynamics is depicted in orange and selected adiabatic elementary transfer events are indicated by green arrows. Bottom panel: ESP charges induced at the nucleobases by the molecular environment. Reprinted with permission from ref 37. Copyright 2013 Royal Society of Chemistry.

proximity with the first excited state causing a stochastic hop to the first excited state (first green arrow, panel B) and a decay of the hole population on G1. In response to this, the population on A and G2 increases and shows an oscillatory behavior. Several further surface hops follow in small time intervals until the system settles with the excess hole located on G2. The authors commented that the agreement between MF and SH for this system is likely to be fortuitous and further investigations with a decoherence-corrected SH algorithm are necessary for more quantitative estimates of the transfer rate.

Overall, the SH simulations point toward a hopping mechanism at least for these simple DNA sequences. Investigations of the distance and sequence dependence of the hole transfer are subject to ongoing studies. NAMD simulations may be used to detect possible signatures of the FR transport, by analyzing the trajectories for N-site energetic degeneracies and the corresponding response of the electronic wave functions at such configurations. If N-site energetic degeneracies exist and indeed contribute to the charge transfer, one may be able to extract typical values for the prefactor of the FR rate eq 71 (τ^{-1}) from such simulations.

6.5. DNA-Photolyase and Cryptochrome

The protein DNA-photolyase[352] has attracted attention both experimentally and theoretically due to the ultrafast biological ET reaction it supports. Upon photoactivation, a hole is transferred from a flavin adenine dinucleotide cofactor (FAD) at one side of the protein, to a tryptophan (Trp) residue on the other side of the protein, via two intermediate Trp residues, FAD → Trp1 → Trp2 → Trp3.[353] According to experimental measurements, the hole transfer between the three Trp residues in *E. coli* DNA-photolyase is ultrafast, on the time scale of 10−100 ps.[353] Interestingly, straightforward application of Marcus ET rate theory for the step Trp2 → Trp3 gives rates that are orders of magnitude lower than in experiment.[250] By contrast, SH MD simulations by Elstner and co-workers predicted an ET rate in close correspondence with experiment.[38,250] It was demonstrated that the large deviation of the Marcus ET rate estimate was due to the assumption of thermal equilibrium for each of the two hole transfer steps from. According to the SH simulation the lifetime of the hole on Trp2 is too short for the protein environment to fully relax. Consequently, the effective barrier for Trp2 → Trp3 is lower than under full equilibrium conditions and hence the (uncorrected) Marcus ET rate is too low. It would be interesting to further analyze the MD data and estimate the nonergodicity corrected Marcus ET rate with a reorganization free energy obtained according to eq 85. This correction should bring the ET rate closer to the experimental and SH estimates. DNA-photolyase and the previously mentioned photosystem II are striking examples where nonequilibrium effects, that is, the partial freezing of protein modes, are of great importance, leading to an acceleration of ET rates by several orders of magnitude.

Cryptochromes are another fascinating family of photoreceptor proteins, thought to support the formation of a radical pair upon light absorption. The radical pair is sensitive to weak magnetic fields such as the Earth's magnetic fields providing migratory birds with a magnetic compass. Recently, a femtosecond spectroscopy study reported hole transfer reactions in a plant cryptochrome on the 1−100 ps time scale, involving up to three tryptophan units.[354] Furthermore, a recent SH MD simulation study suggested a prominent role for the solvent to provide the driving force for fast and stable

formation of a well-separated radical pair.[355] This finding carries an important message for computational chemists aiming at modeling such reactions purely by static quantum chemistry. While too much sampling of the dielectric response of the environment can be problematic for ultrafast ET reactions, too little sampling may also lead to qualitatively incorrect results and mechanisms. Within rate-theoretical approaches, the "right amount" of sampling is dictated by the time scale of the reaction and can be determined self-consistently, e.g., using the scheme in Figure 12A. Explicit charge propagation schemes like SH MD do not suffer from this problem because nuclear and electron dynamics are solved simultaneously, and the sampling time is simply determined by the time it takes for the charge to move from the initial to the final state.

7. CONCLUDING REMARKS AND PERSPECTIVES

Much progress has been made since the first computer simulations of biological ET were reported more than 30 years ago. Single-step biological electron tunneling is now very well understood and many computational methods are available at the empirical, classical, and QM level to estimate the Marcus parameters for biological ET. Some of these methods were reviewed in sections 3 and 4. The agreement with experiment may in principle be systematically improved by improving the quality of the force fields and electronic structure calculations and by extending the time scale that can be routinely accessed by MD simulations (although tremendous progress has been made on this front recently). In section 5 I have reviewed and discussed some of the topics that are currently under debate and less well established such as multistate, ultrafast, and nonergodic biological ET. New theoretical models and numerical simulation approaches have been proposed in the past few years to tackle these interesting problems, and they resulted in new pictures or mechanistic proposals for biological ET. In the following I would like to add a few more comments on these new developments and suggest a number of opportunities for further research in the field.

7.1. Nonergodic Effects

The proposal that the dynamical arrest of protein conformational changes leads to a decrease in ET activation free energy and to an acceleration of ET rates is intriguing.[36] Simulations suggest that the dynamical arrest in combination with sufficiently high electronic coupling makes the primary ET in PSII as well as hole transfer in DNA photolyase ultrafast and this seems a very reasonable explanation.[232,233] It remains to be investigated how common nonergodic effects are among redox proteins that support slower microsecond–nanosecond ET. There are only very few experimental examples where this effect has been observed so far, typically by comparing λ^{st} as obtained from the Stokes shift (difference in absorption and emission band) with λ^{var}, obtained from the band shape of optical transitions. In none of the seven proteins shown in Figure 19 significant deviations between λ^{st} and λ^{var} were reported ($\chi_G \approx 1$, see Table 1), suggesting that rate accelerating nonergodic effects may not occur in these proteins. It would be interesting to investigate whether nonergodic effects are correlated with the fold, size, and surface hydrophobicity of the protein. Careful simulations on a curated set of redox proteins with validated polarizable force fields, and possibly conducted independently by different research groups, would be useful to establish this very interesting proposal, which

would have important implications on our fundamental understanding of biological ET.

7.2. Flickering Resonance Mechanism

Can the FR mechanism compete with the established SE/hopping mechanisms? The FR mechanism has been suggested very recently as a possible short-range transport channel in DNA[35] that, by contrast to SE, accounts for both exponential distance dependence and partial excess charge location on the bridge. The data presented herein indicate that the FR mechanism is expected to be less relevant for ET along heme wires as a consequence of the smaller electronic couplings between heme cofactors than between DNA base pairs. It would be desirable to design experiments, motivated and guided by theory, that can support (or exclude) this mechanism in simple biomolecular systems. An indication for this mechanism is the temporary occupation of charge carriers on the bridge sites on the order of 10 fs in combination with a soft exponential distance dependence. Another interesting characteristic of the FR mechanism is the predicted explicit dependence of the exponential decay constant on temperature, $\partial\theta/\partial T = 1/(2\Delta RT)$ (assuming $\partial\lambda/\partial T$ and $\partial V/\partial T$ are small), in contrast to the SE mechanism, where $\partial\beta/\partial T \approx 0$ (assuming, in addition to the above, that $\partial\Delta A/\partial T$ and $\partial\Delta A_{BD}/\partial T$ are small, too). Hence, a possible experimental signature of the FR mechanism is an increase in the distance decay constant with increasing temperature and this effect should be the larger the lower the temperatures ($1/T$). See also discussion of this point in a recent perspective article.[57]

7.3. Note on ET Models

I would like to emphasize that the SE, FR, and hopping mechanisms are *theoretical models* that have been derived for certain limits and under a number of simplifying assumptions. They are very valuable because they provide an intuitive picture of how charge may transfer across and between biological molecules. Unfortunately, the details of the actual electron transport process, occurring on the femto- to subfemtosecond time scale, are difficult if not currently impossible to observe experimentally. Hence, ET models are supported or rejected in a rather indirect way, by comparing experimentally accessible observables, such as the distance or temperature dependence of the measured ET rate, with the corresponding predictions of a particular model. Possible agreement may not be considered as a "proof" of the validity of the model, as one could imagine that there are several different mechanisms that all have a similar distance or temperature dependence.

7.4. "Ab Initio" Ultrafast Biological ET

A powerful alternative to the above models are numerical simulations aimed at solving the ET problem from first principles. "Ab initio" in this context means direct charge propagation by solving the electronic Schrödinger equation within a given approximation and to couple nuclear motion to electronic charge propagation, again within a given approximation. Quantum–classical NAMD methods[270−272,285] are particularly suitable for the study of ultrafast ET, where some of the assumptions made in rate-based approaches (SE, FR, and hopping) can be questioned, e.g., the validity of equilibrium statistical mechanics and even the simple nonergodic corrections discussed.

The semiempirical SH implementation by Elstner and co-workers[37,38] is a good example for progress in this field and for a pragmatic view regarding the right balance between speed and

accuracy. Many of the parameters that go into the SCC-DFTB electronic Hamiltonian have been benchmarked extensively, such as site energies and most recently electronic coupling matrix elements.[169,170] Adding electronic polarizability to the force field and a way to account for the missing electronic decoherence may be crucial to further enhance the predictive power of the method. These subtleties may tip the balance between localized/delocalized transport. In the context of the above discussion, it would be interesting to know, for instance, whether the FR mechanism proposed for DNA, or features of it, is borne out in explicit SH simulations. Future applications may improve our understanding on the distance and sequence dependence of hole transfer in DNA and may further our knowledge of multistate ET in proteins.

7.5. ET between FeS Clusters

Most of our knowledge on protein ET is derived from heme and Cu-containing proteins. A third ubiquitous type of cofactors are FeS clusters, present, e.g., in complex I of the mitochondrial membrane,[6,66] hydrogenases,[11,16,18] and CO-dehydrogenases.[19,22] There is much less known about the molecular details of electron tunneling between FeS clusters. A recent experimental study gave some insight on the kinetics of ET between the three FeS cluster of a hydrogenase enzyme.[85] On the theoretical side, only few studies have been carried out.[187,188] The reason for this may be the rather complicated electronic structure of these clusters. However, relatively cost-effective broken-symmetry DFT calculations were shown to give reasonably good results for nuclear and electronic structure (see, e.g., refs 356 and 357), and one may use such calculations in combination with QM/MM or classical MD to gain further insight into the kinetics and mechanism of biological ET between FeS clusters.

7.6. ET at the Bio/Inorganic Interface

From a biotechnological point of view, the interaction of redox proteins with metal and semiconductor substrates is a very important topic. Redox enzymes such as hydrogenases, CO-dehydrogenase, and laccase are exquisite biological catalysts for production of renewable fuels in bioelectrochemical cells; see Figure 2. Nonetheless, very little molecular detail is known about the interaction between these proteins with electrode materials and about the electrochemical electron transfer reactions they support. Notable exceptions are cytochrome c on Au[358] and STC (a small tetra-heme cytochrome) on iron oxide.[359] Challenges here are the realistic modeling of relevant adsorption structures of the protein on the electrode surface and the calculation of electrochemical ET rates between a molecular species and a periodic solid.

7.7. Bionanoelectronics

Multi-heme cytochromes such as MtrC may represent a new category of bioorganic conductive materials for potentially revolutionizing bionanotechnological applications such as electronic communication, signaling, and sensing with bacterial cells, nontoxic implantable bioelectronics devices, or even artificial skin. The recent integration of such proteins in electronic circuits is indeed an exciting prospect.[23] In order to fully explore the potential and scope for future bioelectronic applications, it is important and necessary to obtain a fundamental understanding of the electronic properties of these fascinating proteins and their complexes with metal substrates (MSs) at an atomistic level of detail. A satisfactory theoretical explanation of their relatively high electric conductivity is still outstanding.[89,178,360] Recently developed theoretical models of redox molecular junctions[361] as well as numerical simulation methods may shine light on this issue in the years to come.

APPENDIX A. DERIVATION OF TWO-STATE MATCHING PROBABILITY P(2) AND EQ 73

The electron removal functions of donor and acceptor sites are assumed to be Gaussian:

$$\rho_1(\Delta E_1) = \frac{1}{\sqrt{2\pi}\,\sigma_D} \exp\left(-\frac{1}{2\sigma_D{}^2}(\Delta E_1 - \Delta E_D)^2\right) \tag{115}$$

$$\rho_2(\Delta E_2) = \frac{1}{\sqrt{2\pi}\,\sigma_A} \exp\left(-\frac{1}{2\sigma_A{}^2}(\Delta E_2 - \Delta E_A)^2\right) \tag{116}$$

where $\Delta E_D = \langle \Delta E_1 \rangle_R$ is the thermally averaged electron removal energy of the reduced donor in the geometry of the reduced state "R" (and the acceptor in the oxidized state), and $\Delta E_A = \langle \Delta E_2 \rangle_O$ is the thermally averaged electron removal energy of the reduced acceptor in the geometry of the oxidized state "O" (with the donor in the oxidized state). The widths of the fluctuations are related to the reorganization free energies of neutral donor, λ_D, and reduced acceptor, λ_A, $\sigma_D = \sqrt{2k_B T \lambda_D}$ and $\sigma_A = \sqrt{2k_B T \lambda_A}$, and the free energy difference for ET from donor to acceptor is $\Delta A = (\Delta E_D - \lambda_D) - (\Delta E_A + \lambda_A)$. The centers of the distributions are thus separated by $\Delta E_D - \Delta E_A = \Delta A + \lambda$, where λ is the total reorganization free energy $\lambda = \lambda_D + \lambda_A$. Note that the definitions for λ and ΔA given are equivalent to the ones in eqs 15 and 16. The difference is that these quantities are defined here in terms electron removal energies of single sites, whereas in eqs 15 and 16 they are defined in terms of vertical ET energies between sites. The matching probability can be written as

$$P(2) = \int_{-\infty}^{\infty} d\Delta E_1\, \rho_1(\Delta E_1) \int_{\Delta E_1 - V}^{\Delta E_1 + V} d\Delta E_2\, \rho_2(\Delta E_2) \tag{117}$$

Applying the mean value theorem, the inner integral is equal to $2V\rho_2(\Delta E_1 + V^*)$, where $V^* \in [-V, V]$. Final integration over ΔE_1 gives

$$P(2) = 2V/(2\pi\sigma^2)^{1/2} \exp\left[-(\Delta A + \lambda + V^*)^2/(4\lambda k_B T)\right] \tag{118}$$

where $\sigma^2 = \sigma_D{}^2 + \sigma_A{}^2 = 2k_B T \lambda$, and ΔA and λ as defined above. In the nonadiabatic limit, defined in ref 35 by $\theta = 2V/(2k_B T \lambda^2)^{1/2} \ll 1$, the coupling term in the exponent, V^*, can be neglected. In this limit the matching probability P(2) is equal to the Franck–Condon factor times $2V$. Comparison of eq 71 with eq 25 gives a frequency $1/\tau = \pi V/\hbar = \pi^2/\tau_{rabi}$, hence eqs 72 and 73. For a discussion of the adiabatic limit ($\theta \approx 1$), I refer to ref 35 and note that the FR expression in this limit is similar, albeit not identical with the adiabatic ET rate eq 26. I note that the above adiabaticity criterion differs from the usual definition eq 23 by a factor $\theta/(2\pi\gamma) = (2^{1/2}h\nu_n)/(\pi^{3/2}V)$. Biological ET reactions are usually nonadiabatic according to both criteria.

APPENDIX B. DERIVATION OF UPPER BOUND TO THE MATCHING PROBABILITY P(M), EQ 75

Expressions for the upper bound to the matching probability are derived in the Supporting Information of ref 35 for the two-

state ($M = 2$) and three-state ($M = 3$) case for different Gaussian widths for donor, bridge, and acceptor distributions. Here I derive the matching probability for the general M-state case with the restriction that all bridge site energies have equal mean energies and that all Gaussian widths are identical; see model shown in Figure 11. A general formula without these restrictions can be obtained following a similar derivation, but the final expression becomes rather lengthy due to nested Gaussian overlap integrals.

The distribution for the donor is

$$\rho_1(\Delta E_1) = 1/(\sqrt{2\pi}\,\sigma_E)\exp[-(\Delta E_1 - \Delta E_D)^2/(2\sigma_E^2)]$$

the distribution for all bridge sites are the same

$$\rho_i(\Delta E_i) = 1/(\sqrt{2\pi}\,\sigma_E)\exp[-(\Delta E_i - \Delta E_B)^2/(2\sigma_E^2)]$$

$i \in [2, M - 1]$, and the distribution for the acceptor is

$$\rho_M(\Delta E_M) = 1/(\sqrt{2\pi}\,\sigma_E)\exp[-(\Delta E_M - \Delta E_A)^2/(2\sigma_E^2)]$$

Starting from the exact expression eq 74 I replace the lower and upper integration limits for the $(M - 1)$ integrals over ΔE_i, $i \in [2, M]$ by $\Delta E_1 - V$ and $\Delta E_1 + V$, respectively. This gives an upper bound to $P(M)$:

$$P(M) \leq \int_{-\infty}^{\infty} d\Delta E_1\, \rho_1(\Delta E_1) \int_{\Delta E_1 - V}^{\Delta E_1 + V} d\Delta E_2\, \rho_2(\Delta E_2)$$
$$\cdots \int_{\Delta E_1 - V}^{\Delta E_1 + V} d\Delta E_M\, \rho_M(\Delta E_M) \tag{119}$$

To solve the integral over ΔE_2, I introduce a new variable $x = (\Delta E_2 - \Delta E_B)/\sigma_E$, define the distribution ρ_2 in terms of the new variable

$$\rho_2'(x) = 1/(\sqrt{2\pi})\exp(-x^2/2)$$

and make a Taylor expansion of ρ_2' around $x_1 = (\Delta E_1 - \Delta E_B)/\sigma_E$. This gives

$$\rho_2'(x) = 1/(\sqrt{2\pi})\exp(-x_1^2/2)[1 - x_1(x - x_1)$$
$$+ 1/2(x_1^2 - 1)(x - x_1)^2 + O((x - x_1)^3)] \tag{120}$$

Insertion of the expansion in the integral gives

$$\int_{\Delta E_1 - V}^{\Delta E_1 + V} d\Delta E_2\, \rho_2(\Delta E_2)$$
$$= 1/(\sqrt{2\pi}) \int_{x_1 - (V/\sigma_E)}^{x_1 + (V/\sigma_E)} dx\, \exp(-x^2/2) \tag{121}$$

$$= \exp(-x_1^2/2)/(\sqrt{2\pi})[2(V/\sigma_E) + 1/3(x_1^2 - 1)(V/\sigma_E)^3$$
$$+ O((V/\sigma_E)^5)] \tag{122}$$

$$= (2V)/(\sqrt{2\pi}\,\sigma_E)\exp[-(\Delta E_1 - \Delta E_B)^2/(2\sigma_E^2)]$$
$$+ O((V/\sigma_E)^3) \tag{123}$$

Carrying out a similar integration over ΔE_i, $i \in [3, M]$, I obtain

$$P(M) \leq (2V)^{M-1}(\sqrt{2\pi})^{-M/2}\sigma_E^{-M} \int_{-\infty}^{\infty} d\Delta E_1$$
$$\exp[-(\Delta E_1 - \Delta E_D)^2/(2\sigma_E^2)]$$
$$\exp[-(M - 2)(\Delta E_1 - \Delta E_B)^2/(2\sigma_E^2)]$$
$$\exp[-(\Delta E_1 - \Delta E_A)^2/(2\sigma_E^2)]$$
$$+ (M - 1)O((V/\sigma_E)^3) \tag{124}$$

Since the product of two Gaussians is again Gaussian, the latter integral can be solved analytically, giving

$$P(M) \leq M^{-1/2}\left(\sqrt{\frac{2}{\pi}}\frac{V}{\sigma_E}\right)^{M-1}$$
$$\exp\left(-\frac{(\Delta E_B - \Delta E_{D/A})^2}{2\sigma_E^2(1/2 + 1/(M - 2))}\right)$$
$$\exp\left[-\frac{(\Delta A + \lambda)^2}{4\sigma_E^2}\right] + (M - 1)O\left(\left(\frac{V}{\sigma_E}\right)^3\right) \tag{125}$$

where $\Delta E_{D/A} = (\Delta E_D + \Delta E_A)/2$ and $\Delta A + \lambda = \Delta E_D - \Delta E_A$. For different bridge lengths M I obtain

$$P(M) \begin{cases} \leq \left(\sqrt{\frac{2}{\pi}}\frac{V}{\sigma_E}\right)^{M-1}\exp\left(-\frac{(\Delta E_B - \Delta E_{D/A})^2}{2\lambda k_B T}\right)\exp\left[-\frac{(\Delta A + \lambda)^2}{4\lambda k_B T}\right] + (M-1)O\left(\left(\frac{V}{\sigma_E}\right)^3\right) & M \geq 4 \\[3mm] \leq \left(\sqrt{\frac{2}{\pi}}\frac{V}{\sigma_E}\right)^{2}\exp\left(-\frac{(\Delta E_B - \Delta E_{D/A})^2}{3\lambda k_B T}\right)\exp\left[-\frac{(\Delta A + \lambda)^2}{4\lambda k_B T}\right] + O\left(\left(\frac{V}{\sigma_E}\right)^3\right) & M = 3 \\[3mm] = \frac{2V}{\sqrt{4\pi k_B T}}\exp\left[-\frac{(\Delta A + \lambda)^2}{4\lambda k_B T}\right] + O\left(\left(\frac{V}{\sigma_E}\right)^3\right) & M = 2 \end{cases} \tag{126}$$

where I have used $\sigma_E^2 = \lambda k_B T$. The expression for $M \geq 4$ is equal to the one given in the main text, eq 75. However, since for $M \geq 4$ the first factor on the right-hand side of eq 126 is of the same order or smaller than the leading error in the expansion of the integral, higher orders of the integral expansion should be taken into account, in principle. For the case $M = 2$ (only donor and acceptor, no bridge sites), the well-known result is recovered that $P(2)$ is equal to $2V$ times the Franck–Condon factor. In this case, the right-hand side is no longer an upper bound but exact to within the error of the integral expansion.

Equation 77 is obtained from the above definition for $\Delta E_{D/A}$ and noting that the free energy difference between donor and acceptor is $\Delta A = \Delta E_D - \Delta E_A - \lambda$, and between donor and bridge sites $\Delta A_{BD} = \Delta E_D - \Delta E_B - \lambda$. On an aside, $\Delta E_{D/A}$, lying halfway between ΔE_D and ΔE_A, is the most likely electron removal energy in the transition state ensemble for ET. The latter is defined by the configurations with vanishing ET energy, $\Delta E_{M1} = \Delta E_1 - \Delta E_M = 0$. This is why $\Delta E_{D/A}$ was chosen in the SE expression eq 67 as the electron removal energy for the tunneling electron in the transition state.

AUTHOR INFORMATION

Corresponding Author

*E-mail: j.blumberger@ucl.ac.uk.

Notes

The authors declare no competing financial interest.

Biography

Jochen Blumberger's research interests focus on the development and application of quantum and classical molecular simulation methods to study redox and charge transfer reactions in biological systems, organic semiconductors, and most recently also at solid/liquid interfaces. He obtained his Ph.D. in 2005 from Cambridge University, U.K., where he worked on density functional based molecular dynamics simulation of redox reactions, under the supervision of Prof. Michiel Sprik. After a 2-year postdoctoral stay with Prof. Michael L. Klein at the University of Pennsylvania, he returned to Cambridge in 2006 on a Royal Society University Research Fellowship. In 2009 he moved to University College London (UCL), Department of Physics and Astronomy, where he was appointed University Lecturer (2009), Reader (2013), and Professor in Chemical Physics (2015).

REFERENCES

(1) Mitchell, P. Coupling of Phosphorylation to Electron and Hydrogen Transfer by a Chemi-Osmotic type of Mechanism. *Nature* **1961**, *191*, 144−148.

(2) Fleming, G. R.; Martin, J.-L.; Breton, J. Rates of primary electron transfer in photosynthetic reaction centres and their mechanistic implications. *Nature* **1988**, *333*, 190−192.

(3) Ferreira, K. N.; Iverson, T. N.; Maghlahoui, K.; Barber, J.; Iwata, S. Architecture of the Photosynthetic Oxygen-Evolving Center. *Science* **2004**, *303*, 1831−1838.

(4) Wikstrom, M. K. Proton pump coupled to cytochrome c oxidase in mitochondria. *Nature* **1977**, *266*, 271−273.

(5) Abrahams, J. P.; Leslie, A. G.; Lutter, R.; Walker, J. E. Structure at 2.8 A resolution of F1-ATPase from bovine heart mitochondria. *Nature* **1994**, *370*, 621−628.

(6) Hirst, J. Mitochondrial Complex I. *Annu. Rev. Biochem.* **2013**, *82*, 551−575.

(7) Myers, C. R.; Nealson, K. H. Bacterial manganese reduction and growth with manganese oxide as the sole electron acceptor. *Science* **1988**, *240*, 1319−1321.

(8) White, G. F.; Shi, Z.; Shi, L.; Wang, Z.; Dohnalkova, A. C.; Marshall, M. J.; Fredrickson, K. K.; Zachara, J. M.; Butt, J. N.; Richardson, D. J.; et al. Rapid electron exchange between surface-exposed bacterial cytochromes and Fe(III) minerals. *Proc. Natl. Acad. Sci. U. S. A.* **2013**, *110*, 6346−6351.

(9) Pirbadian, S.; Barchinger, S. E.; Leung, K. M.; Jangir, H. S. B.; Bouhenni, R. A.; Reed, S. B.; Romine, M. F.; Saffarini, D. A.; Shi, L.; Gorby, Y. A.; et al. Shewanella oneidensis MR-1 nanowires are outer membrane and periplasmic extensions of the extracellular electron transport components. *Proc. Natl. Acad. Sci. U. S. A.* **2014**, *111*, 12883−12888.

(10) Vincent, K. A.; Parkin, A.; Armstrong, F. A. Investigating and Exploiting the Electrocatalytic Properties of Hydrogenases. *Chem. Rev.* **2007**, *107*, 4366−4413.

(11) Fontecilla-Camps, J. C.; Volbeda, A.; Cavazza, C.; Nicolet, Y. Structure/function relationships of [NiFe]- and [FeFe]-hydrogenases. *Chem. Rev.* **2007**, *107*, 4273−4303.

(12) Lubitz, W.; Reijerse, E. J.; Messinger, J. Solar water-splitting into H-2 and O-2: design principles of photosystem II and hydrogenases. *Energy Environ. Sci.* **2008**, *1*, 15−31.

(13) Armstrong, F. A.; Belsey, N. A.; Cracknell, J. A.; Goldet, G.; Parkin, A.; Reisner, E.; Vincent, K. A.; Wait, A. F. Dynamic electrochemical investigations of hydrogen oxidation and production by enzymes and implications for future technology. *Chem. Soc. Rev.* **2009**, *38*, 36−51.

(14) Wang, P.; Best, R. B.; Blumberger, J. Multiscale Simulation Reveals Multiple Pathways for H_2 and O_2 Transport in a [NiFe]-Hydrogenase. *J. Am. Chem. Soc.* **2011**, *133*, 3548−3556.

(15) Wang, P.; Blumberger, J. Mechanistic insight into the blocking of CO diffusion in [NiFe]-hydrogenase mutants through multiscale simulation. *Proc. Natl. Acad. Sci. U. S. A.* **2012**, *109*, 6399−6404.

(16) Fourmond, V.; Greco, C.; Sybirna, K.; Baffert, C.; Wang, P.; Ezanno, P.; Montefiori, M.; Bruschi, M.; Meynial-Salles, I.; Soucaille, P.; Blumberger, J.; Bottin, H.; De Gioia, L.; Leger, C. The oxidative inactivation of FeFe hydrogenase reveals the plasticity of the H-cluster. *Nat. Chem.* **2014**, *6*, 336−342.

(17) Lubitz, W.; Ogata, H.; Rudiger, O.; Reijerse, E. Hydrogenases. *Chem. Rev.* **2014**, *114*, 4081−4148.

(18) Greco, C.; Fourmond, V.; Baffert, C.; Wang, P.; Dementin, S.; Bertrand, P.; Bruschi, M.; Blumberger, J.; De Gioia, L.; Leger, C. Combining experimental and theoretical methods to learn about the reactivity of gas-processing metalloenzymes. *Energy Environ. Sci.* **2014**, *7*, 3543−3573.

(19) Kung, Y.; Drennan, C. L. A role for nickel-iron cofactors in biological carbon monoxide and carbon dioxide utilization. *Curr. Opin. Chem. Biol.* **2011**, *15*, 276−283.

(20) Woolerton, T. W.; Sheard, S.; Pierce, E.; Ragsdale, S. W.; Armstrong, F. A. CO2 photoreduction at enzyme-modified metal oxide nanoparticles. *Energy Environ. Sci.* **2011**, *4*, 2393−2399.

(21) Wang, P.; Bruschi, M.; De Gioia, L.; Blumberger, J. Uncovering a dynamically formed substrate access tunnel in carbon monoxide dehydrogenase/acetyl-CoA synthase. *J. Am. Chem. Soc.* **2013**, *135*, 9493−9502.

(22) Can, M.; Armstrong, F. A.; Ragsdale, S. W. Structure, Function, and Mechanism of the Nickel Metalloenzymes, CO Dehydrogenase, and Acetyl-CoA Synthase. *Chem. Rev.* **2014**, *114*, 4149−4174.

(23) Leung, K. M.; Wanger, G.; El-Naggar, M. Y.; Gorby, Y. A.; Southam, G.; Lau, W. M.; Yang, J. Shewanella oneidensis MR-1 Bacterial Nanowires Exhibit p-Type, Tunable Electronic Behavior. *Nano Lett.* **2013**, *13*, 2407−2411.

(24) Moser, C. C.; Keske, J. M.; Warncke, K.; Farid, R. S.; Dutton, P. L. Nature of biological electron transfer. *Nature* **1992**, *355*, 796−802.

(25) Page, C. C.; Moser, C. C.; Chen, X.; Dutton, P. L. Natural engineering principles of electron tunnelling in biological oxidation-reduction. *Nature* **1999**, *402*, 47−52.

(26) Gray, H. B.; Winkler, J. R. Electron tunneling through proteins. *Q. Rev. Biophys.* **1999**, *36*, 341−372.

(27) Pfeffer, C.; Larsen, S.; Song, J.; Dong, M.; Besenbacher, F.; Meyer, R. L.; Kjeldsen, K. U.; Schreiber, L.; Gorby, Y. A.; El-Naggar,

M. Y.; et al. Filamentous bacteria transport electrons over centimeter distances. *Nature* **2012**, *491*, 218−221.

(28) Halpern, J.; Orgel, L. E. The Theory of Electron Transfer between Metal Ions in Bridged Systems. *Discuss. Faraday Soc.* **1960**, *29*, 32−41.

(29) Hopfield, J. J. Electron Transfer Between Biological Molecules by Thermally Activated Tunneling. *Proc. Natl. Acad. Sci. U. S. A.* **1974**, *71*, 3640−3644.

(30) Beratan, D. N.; Onuchic, J. N.; Hopfield, J. J. Electron tunneling through covalent and noncovalent pathways in proteins. *J. Chem. Phys.* **1987**, *86*, 4488−4498.

(31) Beratan, D. N.; Betts, J. N.; Onuchic, J. N. Protein electron transfer rates set by the bridging secondary and tertiary structure. *Science* **1991**, *252*, 1285−1288.

(32) Mao, J.; Hauser, K.; Gunner, M. R. How Cytochromes with Different Folds Control Heme Redox Potentials. *Biochemistry* **2003**, *42*, 9829−9840.

(33) Song, Y.; Mao, J.; Gunner, M. R. MCCE2: Improving protein pKa calculations with extensive side chain rotamer sampling. *J. Comput. Chem.* **2009**, *30*, 2231−2247.

(34) Gamiz-Hernandez, A. P.; Kieseritzky, G.; Ishikita, H.; Knapp, E. W. Rubredoxin function: redox behavior from electrostatics. *J. Chem. Theory Comput.* **2011**, *7*, 742−752.

(35) Zhang, Y.; Liu, C.; Balaeff, A.; Skourtis, S. S.; Beratan, D. N. Biological charge transfer via flickering resonance. *Proc. Natl. Acad. Sci. U. S. A.* **2014**, *111*, 10049−10054.

(36) Matyushov, D. V. Protein electron transfer: Dynamics and statistics. *J. Chem. Phys.* **2013**, *139*, 025102.

(37) Kubař, T.; Elstner, M. Efficient algorithms for the simulation of non-adiabatic electron transfer in complex molecular systems: application to DNA. *Phys. Chem. Chem. Phys.* **2013**, *15*, 5794−5813.

(38) Kubař, T.; Elstner, M. A hybrid approach to simulation of electron transfer in complex molecular systems. *J. R. Soc., Interface* **2013**, *10*, 20130415.

(39) Habershon, S.; Manolopoulos, D. E.; Markland, T. E.; Miller, T. F., III. Ring-Polymer Molecular Dynamics: Quantum Effects in Chemical Dynamics from Classical Trajectories in an Extended Phase Space. *Annu. Rev. Phys. Chem.* **2013**, *64*, 387−413.

(40) Menzeleev, A. R.; Bell, F.; Miller, T. F., III Kinetically constrained ring-polymer molecular dynamics for non-adiabatic chemical reactions. *J. Chem. Phys.* **2014**, *140*, 064103−17.

(41) Newton, M. D.; Sutin, N. Electron transfer reactions in condensed phases. *Annu. Rev. Phys. Chem.* **1984**, *35*, 437−480.

(42) Marcus, R. A.; Sutin, N. Electron transfers in chemistry and biology. *Biochim. Biophys. Acta, Rev. Bioenerg.* **1985**, *811*, 265−322.

(43) Newton, M. D. Quantum Chemical Probes of Electron-Transfer Kinetics: The Nature of Donor-Acceptor Interactions. *Chem. Rev.* **1991**, *91*, 767−792.

(44) Bixon, M.; Jortner, J. Electron transfer - from isolated molecules to biomolecules. *Adv. Chem. Phys.* **1999**, *106*, 35−202.

(45) Newton, M. D. Control of Electron Transfer Kinetics: Models for Medium Reorganization and Donor Acceptor Coupling. *Adv. Chem. Phys.* **1999**, *106*, 303−375.

(46) Skourtis, S. S.; Beratan, D. N. Theories of StructureFunction Relationships for Bridge-Mediated Electron Transfer Reactions. *Adv. Chem. Phys.* **1999**, *106*, 377−452.

(47) Iversen, G.; Kharkats, Y. I.; Kuznetsov, A. M.; Ulstrup, J. Fluctuations and Coherence in Long-Range and Multicenter Electron Transfer. *Adv. Chem. Phys.* **1999**, *106*, 453−514.

(48) Warshel, A.; Parson, W. W. Dynamics of biochemical and biophysical reactions: insight from computer simulations. *Q. Rev. Biophys.* **2001**, *34*, 563−679.

(49) Beratan, D. N.; Skourtis, S. S.; Balabin, I. A.; Balaeff, A.; Keinan, S.; Venkatramani, R.; Xiao, D. Steering Electrons on Moving Pathways. *Acc. Chem. Res.* **2009**, *42*, 1669−1678.

(50) Moser, C. C.; Anderson, J. L. R.; Dutton, P. L. Guidelines for tunneling in enzymes. *Biochim. Biophys. Acta, Bioenerg.* **2010**, *1797*, 1573−1586.

(51) Skourtis, S. S.; Waldeck, D. H.; Beratan, D. N. Fluctuations in Biological and Bioinspired Electron-Transfer Reactions. *Annu. Rev. Phys. Chem.* **2010**, *61*, 461−485.

(52) Van Voorhis, T.; Kowalczyk, T.; Kaduk, B.; Wang, L.-P.; Cheng, C.-L.; Wu, Q. The Diabatic Picture of Electron Transfer, Reaction Barriers, and Molecular Dynamics. *Annu. Rev. Phys. Chem.* **2010**, *61*, 149−170.

(53) Venkatramani, R.; Keinan, S.; Balaeff, A.; Beratan, D. N. Nucleic Acid Charge Transfer: Black, White and Gray. *Coord. Chem. Rev.* **2011**, *255*, 635−648.

(54) Saen-Oon, S.; Lucas, M. F.; Guallar, V. Electron transfer in proteins: theory, applications and future perspectives. *Phys. Chem. Chem. Phys.* **2013**, *15*, 15271−15285.

(55) Skourtis, S. S. In *Quantum Effects in Biology*; Masoud Mohseni, G. S. E., Omar, Y., Plenio, M. B., Eds.; Cambridge University Press: Cambridge, U.K., 2014; Chapter 9, pp 198−217.

(56) Winkler, J. R.; Gray, H. B. Electron Flow through Metalloproteins. *Chem. Rev.* **2014**, *114*, 3369−3380.

(57) Beratan, D. N.; Liu, C.; Migliore, A.; Polizzi, N. F.; Skourtis, S. S.; Zhang, P.; Zhang, Y. Charge Transfer in Dynamical Biosystems, or The Treachery of (Static) Images. *Acc. Chem. Res.* **2015**, *48*, 474−481.

(58) Narth, C.; Gillet, N.; Cailliez, F.; Levy, B.; de la Lande, A. Electron Transfer, Decoherence, and Protein Dynamics: Insights from Atomistic Simulations. *Acc. Chem. Res.* **2015**, *48*, 1090−1097.

(59) de la Lande, A.; Gillet, N.; Chen, S.; Salahub, D. R. Progress and challenges in simulating and understanding electron transfer in proteins. *Arch. Biochem. Biophys.* **2015**, *582*, 28.

(60) Hammes-Schiffer, S.; Stuchebrukhov, A. A. Theory of Coupled Electron and Proton Transfer Reactions. *Chem. Rev.* **2010**, *110*, 6939−6960.

(61) Kaila, V. R. I.; Verkhovsky, M. I.; Wikstrom, M. Proton-Coupled Electron Transfer in Cytochrome Oxidase. *Chem. Rev.* **2010**, *110*, 7062−7081.

(62) Siegbahn, P. E. M.; Blomberg, M. R. A. Quantum Chemical Studies of Proton-Coupled Electron Transfer in Metalloenzymes. *Chem. Rev.* **2010**, *110*, 7040−7061.

(63) Kumar, A.; Sevilla, M. D. Proton-Coupled Electron Transfer in DNA on Formation of Radiation-Produced Ion Radicals. *Chem. Rev.* **2010**, *110*, 7002−7023.

(64) Weinberg, D. R.; Gagliardi, C. J.; Hull, J. F.; Murphy, C. F.; Kent, C. A.; Westlake, B. C.; Paul, A.; Ess, D. H.; McCafferty, D. G.; Meyer, T. J. Proton-Coupled Electron Transfer. *Chem. Rev.* **2012**, *112*, 4016−4093.

(65) Migliore, A.; Polizzi, N. F.; Therien, M. J.; Beratan, D. N. Biochemistry and Theory of Proton-Coupled Electron Transfer. *Chem. Rev.* **2014**, *114*, 3381−3465.

(66) Wikstrom, M.; Sharma, V.; Kaila, V. R. I.; Hosler, J. P.; Hummer, G. New Perspectives on Proton Pumping in Cellular Respiration. *Chem. Rev.* **2015**, *115*, 2196−2221.

(67) Natali, M.; Campagna, S.; Scandola, F. Photoinduced electron transfer across molecular bridges: electron- and hole-transfer superexchange pathways. *Chem. Soc. Rev.* **2014**, *43*, 4005−4018.

(68) Olaya-Castro, A.; Scholes, G. D. Energy transfer from Forster-Dexter theory to quantum coherent light-harvesting. *Int. Rev. Phys. Chem.* **2011**, *30*, 49−77.

(69) Leger, C.; Bertrand, P. Direct Electrochemistry of Redox Enzymes as a Tool for Mechanistic Studies. *Chem. Rev.* **2008**, *108*, 2379−2438.

(70) Gates, A. J.; Kemp, G. L.; To, C. Y.; Mann, J.; Marritt, S. J.; Mayes, A. G.; Richardson, D. J.; Butt, J. N. The relationship between redox enzyme activity and electrochemical potentialcellular and mechanistic implications from protein film electrochemistry. *Phys. Chem. Chem. Phys.* **2011**, *13*, 7720−7731.

(71) Haffa, A. L. M.; Lin, S.; Katilius, E.; Williams, J. C.; Taguchi, A. K. W.; Allen, J. P.; Woodbury, N. W. The dependence of the initial electron-transfer rate on driving force in Rhodobacter sphaeroides reaction centers. *J. Phys. Chem. B* **2002**, *106*, 7376−7384.

(72) Pilet, E.; Jasaitis, A.; Liebl, U.; Vos, M. H. Electron transfer between hemes in mammalian cytochrome c oxidase. *Proc. Natl. Acad. Sci. U. S. A.* **2004**, *101*, 16198−16203.

(73) Lewis, F. D.; Zhu, H.; Daublain, P.; Fiebig, T.; Raytchev, M.; Wang, Q.; Shafirovich, V. Crossover from superexchange to hopping as the mechanism for photoinduced charge transfer in DNA hairpin conjugates. *J. Am. Chem. Soc.* **2006**, *128*, 791−800.

(74) Heyes, D. J.; Quinn, A.-M.; Cullis, P. M.; Lee, M.; Munro, A. W.; Scrutton, N. S. Internal electron transfer in multi-site redox enzymes is accessed by laser excitation of thiouredopyrene-3,6,8-trisulfonate (TUPS). *Chem. Commun.* **2009**, 1124−1126.

(75) Millett, F.; Havens, J.; Rajagukguk, S.; Durham, B. Design and use of photoactive ruthenium complexes to study electron transfer within cytochrome bc1 and from cytochrome bc1 to cytochrome c. *Biochim. Biophys. Acta, Bioenerg.* **2013**, *1827*, 1309−1319.

(76) Simonneaux, G.; Bondon, A. Mechanism of Electron Transfer in Heme Proteins and Models: The NMR Approach. *Chem. Rev.* **2005**, *105*, 2627−2646.

(77) Ungar, L. W.; Newton, M. D.; Voth, G. A. Classical and quantum simulation of electron transfer through a polypeptide. *J. Phys. Chem. B* **1999**, *103*, 7367−7382.

(78) Farver, O.; Pecht, I. Copper Proteins as Model Systems for Investigating Intramolecular Electron Transfer Processes. *Adv. Chem. Phys.* **1999**, *107*, 555−589.

(79) Farver, O.; Marshall, N. M.; Wherland, S.; Lu, Y.; Pecht, I. Designed Azurins Show Lower Reorganization Free Energies for Intraprotein Electron Transfer. *Proc. Natl. Acad. Sci. U. S. A.* **2013**, *110*, 10536−10540.

(80) El Hammi, E.; Houee-Levin, C.; Řezáč, J.; Levy, B.; Demachy, I.; Baciou, L.; de la Lande, A. New insights into the mechanism of electron transfer within flavohemoglobins: tunnelling pathways, packing density, thermodynamic and kinetic analyses. *Phys. Chem. Chem. Phys.* **2012**, *14*, 13872−13880.

(81) Farver, O.; Hosseinzadeh, P.; Marshall, N. M.; Wherland, S.; Lu, Y.; Pecht, I. Long-Range Electron Transfer in Engineered Azurins Exhibits Marcus Inverted Region Behavior. *J. Phys. Chem. Lett.* **2015**, *6*, 100−105.

(82) Chi, Q.; Zhang, J.; Andersen, J. E. T.; Ulstrup, J. Ordered Assembly and Controlled Electron Transfer of the Blue Copper Protein Azurin at Gold (111) Single-Crystal Substrates. *J. Phys. Chem. B* **2001**, *105*, 4669−4679.

(83) Marritt, S. J.; Kemp, G. L.; Xiaoe, L.; Durrant, J. R.; Cheesman, M. R.; Butt, J. N. Spectroelectrochemical characterization of a pentaheme cytochrome in solution and as electrocatalytically active films on nanocrystalline metal-oxide electrodes. *J. Am. Chem. Soc.* **2008**, *130*, 8588−8589.

(84) Ly, H. K.; Wisitruangsakul, N.; Sezer, M.; Feng, J.-J.; Kranich, A.; Weidinger, I. M.; Zebger, I.; Murgida, D. H.; Hildebrandt, P. Electric-field effects on the interfacial electron transfer and protein dynamics of cytochrome c. *J. Electroanal. Chem.* **2011**, *660*, 367−376.

(85) Dementin, S.; Burlat, B.; Fourmond, V.; Leroux, F.; Liebgott, P.-P.; Abou Hamdan, A.; Leger, C.; Rousset, M.; Guigliarelli, B.; Bertrand, P. Rates of Intra- and Intermolecular Electron Transfers in Hydrogenase Deduced from Steady-State Activity Measurements. *J. Am. Chem. Soc.* **2011**, *133*, 10211−10221.

(86) Bortolotti, C. A.; Siwko, M. E.; Castellini, E.; Ranieri, A.; Sola, M.; Corni, S. The Reorganization Energy in Cytochrome c is Controlled by the Accessibility of the Heme to the Solvent. *J. Phys. Chem. Lett.* **2011**, *2*, 1761−1765.

(87) Monari, S.; Battistuzzi, G.; Bortolotti, C. A.; Yanagisawa, S.; Sato, K.; Li, C.; Salard, I.; Kostrz, D.; Borsari, M.; Ranieri, A.; et al. Understanding the Mechanism of Short-Range Electron Transfer Using an Immobilized Cupredoxin. *J. Am. Chem. Soc.* **2012**, *134*, 11848−11851.

(88) Wigginton, N. S.; Rosso, K. M.; Lower, B. H.; Shi, L.; Hochella, M. F. J. Electron tunneling properties of outer-membrane decaheme cytochromes from Shewanella oneidensis. *Geochim. Cosmochim. Acta* **2007**, *71*, 543−555.

(89) Byun, H. S.; Pirbadian, S.; Nakano, A.; Shi, L.; El-Naggar, M. Y. Kinetic Monte Carlo Simulations and Molecular Conductance Measurements of the Bacterial Decaheme Cytochrome MtrF. *ChemElectroChem* **2014**, *1*, 1932−1939.

(90) El-Naggar, M. Y.; Wanger, G.; Leung, K.; Yuzvinsky, T. D.; Southam, G.; Yang, J.; Lau, W. M.; Nealson, K. H.; Gorby, Y. A. Electrical transport along bacterial nanowires from Shewanella oneidensis MR-1. *Proc. Natl. Acad. Sci. U. S. A.* **2010**, *107*, 18127−18131.

(91) Gray, H. B.; Winkler, J. R. Electron transfer in proteins. *Annu. Rev. Biochem.* **1996**, *65*, 537−561.

(92) Bhattacharyya, A. K.; Lipka, J. J.; Waskell, L.; Tollin, G. Laser flash photolysis studies of the reduction kinetics of NADPH:cytochrome P-450 reductase. *Biochemistry* **1991**, *30*, 759−765.

(93) Shih, C.; Museth, A. K.; Abrahamsson, M.; Blanco-Rodriguez, A. M.; Di Bilio, A. J.; Sudhamsu, J.; Crane, B. R.; Ronayne, K. L.; Towrie, M.; Vlcek, A.; et al. Tryptophan-Accelerated Electron Flow Through Proteins. *Science* **2008**, *320*, 1760−1762.

(94) Takematsu, K.; Williamson, H.; Blanco-Rodriguez, A. M.; Sokolova, L.; Nikolovski, P.; Kaiser, J. T.; Towrie, M.; Clark, I. P.; Vlcek, A., Jr.; Winkler, J. R.; et al. Tryptophan-Accelerated Electron Flow Across a Protein-Protein Interface. *J. Am. Chem. Soc.* **2013**, *135*, 15515−15525.

(95) Gray, H.; Winkler, J. R. Electron flow through metalloproteins. *Biochim. Biophys. Acta, Bioenerg.* **2010**, *1797*, 1563−1572.

(96) Kuki, A.; Wolynes, P. Electron-tunneling paths in proteins. *Science* **1987**, *236*, 1647−1652.

(97) Siddarth, P.; Marcus, R. Correlation between theory and experiment in electron-transfer reactions in proteins: electronic couplings in modified cytochrome c and myoglobin derivatives. *J. Phys. Chem.* **1993**, *97*, 13078−13082.

(98) Gruschus, J.; Kuki, A. New Hamiltonian model for long-range electronic superexchange in complex molecular structures. *J. Phys. Chem.* **1993**, *97*, 5581−5593.

(99) Gruschus, J.; Kuki, A. Ellipsoidal delocalization of tunneling electrons in long-range electron transfer proteins. *J. Phys. Chem. B* **1999**, *103*, 11407−11414.

(100) Skourtis, S.; Balabin, I.; Kawatsu, T.; Beratan, D. Protein dynamics and electron transfer: Electronic decoherence and non-Condon effects. *Proc. Natl. Acad. Sci. U. S. A.* **2005**, *102*, 3552−3557.

(101) Prytkova, T.; Kurnikov, I.; Beratan, D. Ab initio based calculations of electron-transfer rates in metalloproteins. *J. Phys. Chem. B* **2005**, *109*, 1618−1625.

(102) Kawatsu, T.; Beratan, D.; Kakitani, T. Conformationally averaged score functions for electronic propagation in proteins. *J. Phys. Chem. B* **2006**, *110*, 5747−5757.

(103) Migliore, A.; Corni, S.; Di Felice, R.; Molinari, E. First-principles density-functional theory calculations of electron-transfer rates in azurin dimers. *J. Chem. Phys.* **2006**, *124*, 064501−16.

(104) Prytkova, T. R.; Kurnikov, I. V.; Beratan, D. N. Coupling coherence distinguishes structure sensitivity in protein electron transfer. *Science* **2007**, *315*, 622−625.

(105) Blumberger, J. Free energies for biological electron transfer from QM/MM calculation: method, application and critical assessment. *Phys. Chem. Chem. Phys.* **2008**, *10*, 5651−5667.

(106) Tipmanee, V.; Oberhofer, H.; Park, M.; Kim, K. S.; Blumberger, J. Prediction of Reorganization Free Energies for Biological Electron Transfer: A Comparative Study of Ru-Modified Cytochromes and a 4-Helix Bundle Protein. *J. Am. Chem. Soc.* **2010**, *132*, 17032−17040.

(107) Oliveberg, M.; Malmstroem, B. G. Internal electron transfer in cytochrome c oxidase: evidence for a rapid equilibrium between cytochrome a and the bimetallic site. *Biochemistry* **1991**, *30*, 7053−7057.

(108) Verkhovsky, M. I.; Morgan, J. E.; Wikstroem, M. Intramolecular electron transfer in cytochrome c oxidase: a cascade of equilibria. *Biochemistry* **1992**, *31*, 11860−11863.

(109) Verkhovsky, M. I.; Jasaitis, A.; Wikstrom, M. Ultrafast haem-haem electron transfer in cytochrome c oxidase. *Biochim. Biophys. Acta, Bioenerg.* 2001, *1506*, 143−146.

(110) Jasaitis, A.; Rappaport, F.; Pilet, E.; Liebl, U.; Vos, M. H. Activationless electron transfer through the hydrophobic core of cytochrome c oxidase. *Proc. Natl. Acad. Sci. U. S. A.* 2005, *102*, 10882−10886.

(111) Jasaitis, A.; Johansson, M. P.; Wikstrom, M.; Vos, M. H.; Verkhovsky, M. I. Nanosecond electron tunneling between the hemes in cytochrome bo(3). *Proc. Natl. Acad. Sci. U. S. A.* 2007, *104*, 20811−20814.

(112) Wang, H.; Lin, S.; Allen, J. P.; Williams, J. C.; Blankert, S.; Laser, C.; Woodbury, N. W. Protein dynamics control the kinetics of initial electron transfer in photosynthesis. *Science* 2007, *316*, 747−750.

(113) Parson, W. W.; Warshel, A. Dependence of Photosynthetic Electron-Transfer Kinetics on Temperature and Energy in a Density-Matrix Model. *J. Phys. Chem. B* 2004, *108*, 10474−10483.

(114) Ceccarelli, M.; Marchi, M. Simulation and modeling of the Rhodobacter sphaeroides bacterial reaction center II: Primary charge separation. *J. Phys. Chem. B* 2003, *107*, 5630−5641.

(115) Marchi, M.; Gehlen, J. N.; Chandler, D.; Newton, M. D. Diabatic surfaces and the pathway for primary electron transfer in a photosynthetic reaction center. *J. Am. Chem. Soc.* 1993, *115*, 4178−4190.

(116) Parson, W. W.; Warshel, A. A density-matrix model of photosynthetic electron transfer with microscopically estimated vibrational relaxation times. *Chem. Phys.* 2004, *296*, 201−216.

(117) Borrelli, R.; Di Donato, M.; Peluso, A. Quantum Dynamics of Electron Transfer from Bacteriochlorophyll to Pheophytin in Bacterial Reaction Centers. *J. Chem. Theory Comput.* 2007, *3*, 673−680.

(118) Chaudhury, S.; Cherayil, B. J. Modulation of electron transfer kinetics by protein conformational fluctuations during early-stage photosynthesis. *J. Chem. Phys.* 2007, *127*, 145103−6.

(119) Sumi, H.; Marcus, R. A. Dynamical effects in electron transfer reactions. *J. Chem. Phys.* 1986, *84*, 4894−4914.

(120) Medvedev, E. S.; Kotelnikov, A. I.; Barinov, A. V.; Psikha, B. L.; Ortega, J. M.; Popovic, D. M.; Stuchebrukhov, A. A. Protein Dynamics Control of Electron Transfer in Photosynthetic Reaction Centers from Rps. Sulfoviridis. *J. Phys. Chem. B* 2008, *112*, 3208−3216.

(121) Giese, B.; Amaudrut, J.; Kohler, A.-K.; Spormann, M.; Wessely, S. Direct observation of hole transfer through DNA by hopping between adenine bases and by tunnelling. *Nature* 2001, *412*, 318−320.

(122) Berlin, Y. A.; Burin, A. L.; Ratner, M. A. Charge hopping in DNA. *J. Am. Chem. Soc.* 2001, *123*, 260−268.

(123) Conwell, E. M. Charge transport in DNA in solution: the role of polarons. *Proc. Natl. Acad. Sci. U. S. A.* 2005, *102*, 8795−8799.

(124) Conron, S. M. M.; Thazhathveetil, A. K.; Wasielewski, M. R.; Burin, A. L.; Lewis, F. D. Direct measurement of the dynamics of hole hopping in extended DNA G-tracts. An unbiased random walk. *J. Am. Chem. Soc.* 2010, *132*, 14388−14390.

(125) Thazhathveetil, A. K.; Trifonov, A.; Wasielewski, M. R.; Lewis, F. D. Increasing the speed limit for hole transport in DNA. *J. Am. Chem. Soc.* 2011, *133*, 11485−11487.

(126) Marcus, R. A. Theory of oxidation-reduction reactions involving electron transfer.1. *J. Chem. Phys.* 1956, *24*, 966−978.

(127) Marcus, R. A. Electrostatic Free Energy and Other Properties of States Having Nonequilibrium Polarization. I. *J. Chem. Phys.* 1956, *24*, 979−989.

(128) Pacher, T.; Cederbaum, L. S.; Köppel, H. Approximately diabatic states from block diagonalization of the electronic Hamiltonian. *J. Chem. Phys.* 1988, *89*, 7367−7381.

(129) Cave, R. J.; Newton, M. D. Calculation of electronic coupling matrix elements for ground and excited state electron transfer reactions: Comparison of the generalized MullikenHush and block diagonalization methods. *J. Chem. Phys.* 1997, *106*, 9213−9226.

(130) Wu, Q.; Van Voorhis, T. Extracting electron transfer coupling elements from constrained density functional theory. *J. Chem. Phys.* 2006, *125*, 164105−9.

(131) Subotnik, J. E.; Yeganeh, S.; Cave, R. J.; Ratner, M. A. Constructing diabatic states from adiabatic states: Extending generalized Mulliken-Hush to multiple charge centers with Boys localization. *J. Chem. Phys.* 2008, *129*, 244101−14.

(132) Subotnik, J. E.; Cave, R. J.; Steele, R. P.; Shenvi, N. The initial and final states of electron and energy transfer processes: Diabatization as motiva ted by system-solvent interactions. *J. Chem. Phys.* 2009, *130*, 234102−14.

(133) Migliore, A. Nonorthogonality Problem and Effective Electronic Coupling Calculation: Application to Charge Transfer in pi-Stacks Relevant to Biochemistry and Molecular Electronics. *J. Chem. Theory Comput.* 2011, *7*, 1712−1725.

(134) Zusman, L. D. Outer-sphere electron transfer in polar solvents. *Chem. Phys.* 1980, *49*, 295−304.

(135) Warshel, A. Dynamics of reactions in polar solvents. Semiclassical trajectory studies of electron-transfer and proton-transfer reactions. *J. Phys. Chem.* 1982, *86*, 2218−2224.

(136) Kakitani, T.; Mataga, N. New energy gap laws for the charge separation process in the fluorescence quenching reaction and the charge recombination process of ion pairs produced in polar solvents. *J. Phys. Chem.* 1985, *89*, 8−10.

(137) Kakitani, T.; Mataga, N. Different energy gap laws for the three types of electron-transfer reactions in polar solvents. *J. Phys. Chem.* 1986, *90*, 993−995.

(138) Kakitani, T.; Mataga, N. Comprehensive study on the role of coordinated solvent mode played in electron-transfer reactions in polar solutions. *J. Phys. Chem.* 1987, *91*, 6277−6285.

(139) Kuharski, R. A.; Bader, J. S.; Chandler, D.; Sprik, M.; Klein, M. L.; Impey, R. W. Molecular model for aqueous ferrousferric electron transfer. *J. Chem. Phys.* 1988, *89*, 3248−3257.

(140) Carter, E. A.; Hynes, J. T. Solute-dependent solvent force constants for ion pairs and neutral pairs in a polar solvent. *J. Phys. Chem.* 1989, *93*, 2184−2187.

(141) Tachiya, M. Relation between the electron-transfer rate and the free energy change of reaction. *J. Phys. Chem.* 1989, *93*, 7050−7052.

(142) King, G.; Warshel, A. Investigation of the free energy functions for electron transfer reactions. *J. Chem. Phys.* 1990, *93*, 8682−8692.

(143) Blumberger, J.; Tateyama, Y.; Sprik, M. Ab initio molecular dynamics simulation of redox reactions in solution. *Comput. Phys. Commun.* 2005, *169*, 256−261.

(144) Tateyama, Y.; Blumberger, J.; Sprik, M.; Tavernelli, I. Density-functional molecular-dynamics study of the redox reactions of two anionic, aqueous transition-metal complexes. *J. Chem. Phys.* 2005, *122*, 234505−17.

(145) Blumberger, J.; Sprik, M. Quantum versus classical electron transfer energy as reaction coordinate for the aqueous Ru^{2+}/Ru^{3+} redox reaction. *Theor. Chem. Acc.* 2006, *115*, 113−126.

(146) Blumberger, J.; Tavernelli, I.; Klein, M. L.; Sprik, M. Diabatic free energy curves and coordination fluctuations for the aqueous Ag^{+}/Ag^{2+} redox couple: A biased Born-Oppenheimer molecular dynamics investigation. *J. Chem. Phys.* 2006, *124*, 064507−12.

(147) Tateyama, Y.; Blumberger, J.; Ohno, T.; Sprik, M. Free Energy calculation of Water Addition Coupled to Reduction of Aqueous RuO_4^{-}. *J. Chem. Phys.* 2007, *126*, 204506−10.

(148) Blumberger, J. Cu_{aq}^{+}/Cu_{aq}^{2+} Redox Reaction Exhibits Strong Nonlinear Solvent Response Due to Change in Coordination Number. *J. Am. Chem. Soc.* 2008, *130*, 16065−16068.

(149) Cheng, J.; Sulpizi, M.; Sprik, M. Redox Potentials and pKa for Benzoquinone from Density Functional Theory Based Molecular Dynamics. *J. Chem. Phys.* 2009, *131*, 154504−20.

(150) Seidel, R.; Faubel, M.; Winter, B.; Blumberger, J. Single-ion reorganization free energy of aqueous $Ru(bpy)_3^{2+/3+}$ and $Ru(H_2O)_6^{2+/3+}$ from photoemission spectroscopy and density functional molecular dynamics simulation. *J. Am. Chem. Soc.* 2009, *131*, 16127−16137.

(151) Moens, J.; Seidel, R.; Geerlings, P.; Faubel, M.; Winter, B.; Blumberger, J. Energy Levels and Redox Properties of Aqueous $Mn^{2+/3+}$ from Photoemission Spectroscopy and Density Functional

Molecular Dynamics Simulation. *J. Phys. Chem. B* **2010**, *114*, 9173−9182.

(152) Vuilleumier, R.; Tay, K. A.; Jeanmairet, G.; Borgis, D.; Boutin, A. Extension of Marcus picture for electron transfer reactions with large solvation changes. *J. Am. Chem. Soc.* **2012**, *134*, 2067−2074.

(153) Drechsel-Grau, C.; Sprik, M. Activation energy for a model ferrous-ferric half reaction from transition path sampling. *J. Chem. Phys.* **2012**, *136*, 034506−11.

(154) Eyring, H. The Activated Complex in Chemical Reactions. *J. Chem. Phys.* **1935**, *3*, 107−115.

(155) Landau, L. D. On the theory of transfer of energy at collisions. I. *Phys. Z. Sowjetunion* **1932**, *1*, 88.

(156) Zener, C. Non-Adiabatic Crossing of Energy Levels. *Proc. R. Soc. London, Ser. A* **1932**, *137*, 696−702.

(157) Nitzan, A. *Chemical Dynamics in Condensed Phases*; Oxford University Press: New York, 2006.

(158) Brunschwig, B. S.; Logan, J.; Newton, M. D.; Sutin, N. A semiclassical treatment of electron-exchange reactions. Application to the hexaaquoiron(II)-hexaaquoiron(III) system. *J. Am. Chem. Soc.* **1980**, *102*, 5798−5809.

(159) Troisi, A.; Nitzan, A.; Ratner, M. A. A rate constant expression for charge transfer through fluctuating bridges. *J. Chem. Phys.* **2003**, *119*, 5782−5788.

(160) Marcus, R. A. Electron transfer reactions in chemistry. Theory and experiment. *Rev. Mod. Phys.* **1993**, *65*, 599−610.

(161) Song, X.; Marcus, R. A. Quantum correction for electron transfer rates. Comparison of polarizable versus nonpolarizable descriptions of solvent. *J. Chem. Phys.* **1993**, *99*, 7768−7773.

(162) Jortner, J. Temperature dependent activation energy for electron transfer between biological molecules. *J. Chem. Phys.* **1976**, *64*, 4860−4867.

(163) Langhoff, S. R.; Davidson, E. R. Configuration interaction calculations on the nitrogen molecule. *Int. J. Quantum Chem.* **1974**, *8*, 61−72.

(164) Butscher, W.; Shih, S.; Buenker, R. J.; Peyerimhoff, S. D. Configuration interaction calculations for the N2 molecule and its three lowest dissociation limits. *Chem. Phys. Lett.* **1977**, *52*, 457−462.

(165) Szalay, P. G.; Muller, T.; Gidofalvi, G.; Lischka, H.; Shepard, R. Multiconfiguration Self-Consistent Field and Multireference Configuration Interaction Methods and Applications. *Chem. Rev.* **2012**, *112*, 108−181.

(166) Angeli, C.; Cimiraglia, R.; Evangelisti, S.; Leininger, T.; Malrieu, J.-P. Introduction of n-electron valence states for multireference perturbation theory. *J. Chem. Phys.* **2001**, *114*, 10252−10264.

(167) Angeli, C.; Cimiraglia, R.; Malrieu, J.-P. n-electron valence state perturbation theory: A spinless formulation and an efficient implementation of the strongly contracted and of the partially contracted variants. *J. Chem. Phys.* **2002**, *117*, 9138−9153.

(168) Angeli, C.; Cimiraglia, R.; Malrieu, J.-P. N-electron valence state perturbation theory: a fast implementation of the strongly contracted variant. *Chem. Phys. Lett.* **2001**, *350*, 297−305.

(169) Kubas, A.; Hoffmann, F.; Heck, A.; Oberhofer, H.; Elstner, M.; Blumberger, J. Electronic couplings for molecular charge transfer: benchmarking CDFT, FODFT and FODFTB against high-level ab initio calculations. *J. Chem. Phys.* **2014**, *140*, 104105−21.

(170) Kubas, A.; Gajdos, F.; Heck, A.; Oberhofer, H.; Elstner, M.; Blumberger, J. Electronic couplings for molecular charge transfer: benchmarking CDFT, FODFT and FODFTB against high-level ab initio calculations. II. *Phys. Chem. Chem. Phys.* **2015**, *17*, 14342−14354.

(171) Blumberger, J.; McKenna, K. Constrained Density Functional Theory Applied to Electron Tunnelling between Defects in MgO. *Phys. Chem. Chem. Phys.* **2013**, *15*, 2184−2196.

(172) Moser, C. C.; Chobot, S. E.; Page, C. C.; Dutton, P. L. Distance metrics for heme protein electron tunneling. *Biochim. Biophys. Acta, Bioenerg.* **2008**, *1777*, 1032−1037.

(173) Jones, M. L.; Kurnikov, I. V.; Beratan, D. N. The Nature of Tunneling Pathway and Average Packing Density Models for Protein-Mediated Electron Transfer. *J. Phys. Chem. A* **2002**, *106*, 2002−2006.

(174) Beratan, D. N.; Balabin, I. A. Heme-copper oxidases use tunneling pathways. *Proc. Natl. Acad. Sci. U. S. A.* **2008**, *105*, 403−404.

(175) Balabin, I. A.; Beratan, D. N.; Skourtis, S. S. Persistence of Structure Over Fluctuations in Biological Electron-Transfer Reactions. *Phys. Rev. Lett.* **2008**, *101*, 158102.

(176) Moser, C. C.; Page, C. C.; Dutton, P. L. Darwin at the molecular scale: selection and variance in electron tunnelling proteins including cytochrome c oxidase. *Philos. Trans. R. Soc., B* **2006**, *361*, 1295−1305.

(177) Smith, D. M. A.; Rosso, K. M.; Dupuis, M.; Valiev, M.; Straatsma, T. P. Electronic Coupling between Heme Electron-Transfer Centers and Its Decay with Distance Depends Strongly on Relative Orientation. *J. Phys. Chem. B* **2006**, *110*, 15582−15588.

(178) Breuer, M.; Rosso, K. M.; Blumberger, J. Electron flow in multi-heme bacterial cytochromes is a balancing act between heme electronic interaction and redox potentials. *Proc. Natl. Acad. Sci. U. S. A.* **2014**, *111*, 611−616.

(179) Priyadarshy, S.; Skourtis, S. S.; Risser, S. M.; Beratan, D. N. Bridgemediated electronic interactions: Differences between Hamiltonian and Green function partitioning in a nonorthogonal basis. *J. Chem. Phys.* **1996**, *104*, 9473−9481.

(180) Beratan, D. N.; Hopfield, J. J. Calculation of tunneling matrix elements in rigid systems: mixed-valence dithiaspirocyclobutane molecules. *J. Am. Chem. Soc.* **1984**, *106*, 1584−1894.

(181) Tan, M.-L.; Balabin, I.; Onuchic, J. N. Dynamics of electron transfer pathways in cytochrome c oxidase. *Biophys. J.* **2004**, *86*, 1813−1819.

(182) Stuchebrukhov, A. A. Tunneling currents in electron transfer reactions in proteins. *J. Chem. Phys.* **1996**, *104*, 8424−8432.

(183) Stuchebrukhov, A. A. Tunneling currents in electron transfer reaction in proteins. II. Calculation of electronic superexchange matrix element and tunneling currents using nonorthogonal basis sets. *J. Chem. Phys.* **1996**, *105*, 10819−10829.

(184) Stuchebrukhov, A. A. Long-distance electron tunneling in proteins. *Theor. Chem. Acc.* **2003**, *110*, 291−306.

(185) Hagras, M. A.; Stuchebrukhov, A. A. Transition Flux Formula for the Electronic Coupling Matrix Element. *J. Phys. Chem. B* **2015**, *119*, 7712−7721.

(186) Nishioka, H.; Kimura, A.; Yamato, T.; Kawatsu, T.; Kakitani, T. Interference, Fluctuation, and Alternation of Electron Tunneling in Protein Media. 1. Two Tunneling Routes in Photosynthetic Reaction Center Alternate Due to Thermal Fluctuation of Protein Conformation. *J. Phys. Chem. B* **2005**, *109*, 1978−1987.

(187) Hayashi, T.; Stuchebrukhov, A. A. Electron tunneling in respiratory complex I. *Proc. Natl. Acad. Sci. U. S. A.* **2010**, *107*, 19157−19162.

(188) Hayashi, T.; Stuchebrukhov, A. A. Quantum Electron Tunneling in Respiratory Complex I. *J. Phys. Chem. B* **2011**, *115*, 5354−5364.

(189) Skourtis, S.; Nitzan, A. Effects of initial state preparation on the distance dependence of electron transfer through molecular bridges and wires. *J. Chem. Phys.* **2003**, *119*, 6271−6276.

(190) Domcke, W.; Woywod, C. Direct construction of diabatic states in the CASSCF approach. Application to the conical intersection of the 1A2 and 1B1 excited states of ozone. *Chem. Phys. Lett.* **1993**, *216*, 362−368.

(191) Cave, R. J.; Newton, M. D. Generalization of the Mulliken-Hush treatment for the calculation of electron transfer matrix elements. *Chem. Phys. Lett.* **1996**, *249*, 15−19.

(192) Voityuk, A. A.; Rösch, N. Fragment charge difference method for estimating donor-acceptor electronic coupling: Applicati on to DNA pi-stacks. *J. Chem. Phys.* **2002**, *117*, 5607−5616.

(193) Hsu, C.-P.; You, Z.-Q.; Chen, H.-C. Characterization of the Short-Range Couplings in Excitation Energy Transfer. *J. Phys. Chem. C* **2008**, *112*, 1204−1212.

(194) Farazdel, A.; Dupuis, M.; Clementi, E.; Aviram, A. Electric-field induced intramolecular electron transfer in spiro.pi.-electron systems and their suitability as molecular electronic devices. A theoretical study. *J. Am. Chem. Soc.* **1990**, *112*, 4206−4214.

(195) Senthilkumar, K.; Grozema, F. C.; Bickelhaupt, F. M.; Siebbeles, L. D. A. Charge transport in columnar stacked triphenylenes: Effects of conformational fluctuations on charge transfer integrals and site energies. *J. Chem. Phys.* **2003**, *119*, 9809−9817.

(196) Coropceanu, V.; Cornil, J.; da Silva Filho, D. A.; Olivier, Y.; Silbey, R.; Bredas, J.-L. Charge Transport in Organic Semiconductors. *Chem. Rev.* **2007**, *107*, 926−952.

(197) Kirkpatrick, J. An Approximate Method for Calculating Transfer Integrals Based on the Zindo Hamiltonian. Int. *Int. J. Quantum Chem.* **2008**, *108*, 51−56.

(198) Oberhofer, H.; Blumberger, J. Insight into the mechanism of the Ru^{2+}-Ru^{3+} electron self-exchange reaction from quantitative rate calculations. *Angew. Chem., Int. Ed.* **2010**, *49*, 3631−3634.

(199) Oberhofer, H.; Blumberger, J. Revisiting electronic couplings and incoherent hopping models for electron transport in crystalline C_{60} at ambient temperatures. *Phys. Chem. Chem. Phys.* **2012**, *14*, 13846−13852.

(200) Migliore, A.; Sit, P. H.-L.; Klein, M. L. Evaluation of Electronic Coupling in Transition-Metal Systems Using DFT: Application to the Hexa-Aquo Ferric-Ferrous Redox Couple. *J. Chem. Theory Comput.* **2009**, *5*, 307−323.

(201) Migliore, A. Full-electron calculation of effective electronic couplings and excitation energies of charge transfer states: Application to hole transfer in DNA pi-stacks. *J. Chem. Phys.* **2009**, *131*, 114113−12.

(202) Wu, Q.; Van Voorhis, T. Direct optimization method to study constrained systems within density-functional theory. *Phys. Rev. A: At., Mol., Opt. Phys.* **2005**, *72*, 024502.

(203) Wu, Q.; Cheng, C.-L.; Van Voorhis, T. Configuration interaction based on constrained density functional theory: A multireference method. *J. Chem. Phys.* **2007**, *127*, 164119−9.

(204) Oberhofer, H.; Blumberger, J. Charge constrained density functional molecular dynamics for simulation of condensed phase electron transfer reactions. *J. Chem. Phys.* **2009**, *131*, 064101−11.

(205) Oberhofer, H.; Blumberger, J. Electronic coupling matrix elements from charge constrained density functional theory calculations using a plane wave basis set. *J. Chem. Phys.* **2010**, *133*, 244105−10.

(206) de la Lande, A.; Salahub, D. R. Derivation of interpretative models for long range electron transfer from constrained density functional theory. *J. Mol. Struct.: THEOCHEM* **2010**, *943*, 115−120.

(207) Sena, A. M. P.; Miyazaki, T.; Bowler, D. R. Linear Scaling Constrained Density Functional Theory in CONQUEST. *J. Chem. Theory Comput.* **2011**, *7*, 884−889.

(208) Ramos, P.; Papadakis, M.; Pavanello, M. Performance of Frozen Density Embedding for Modeling Hole Transfer Reactions. *J. Phys. Chem. B* **2015**, *119*, 7541−7557.

(209) Cave, R. J.; Baxter, D. V.; Goddard, W. A., III; Baldeschwieler, J. D. Theoretical studies of electron transfer in metal dimers: $XY^+ \rightarrow X^+Y$, where X, Y = Be, Mg, Ca, Zn, Cd. *J. Chem. Phys.* **1987**, *87*, 926−935.

(210) Cave, R. J.; Newton, M. D. Multistate Treatments of the Electronic Coupling in Donor-Bridge-Acceptor Systems: Insights and Caveats from a Simple Model. *J. Phys. Chem. A* **2014**, *118*, 7221−7234.

(211) McKenna, K.; Blumberger, J. Crossover from Incoherent to Coherent Electron Tunneling between Defects in MgO. *Phys. Rev. B: Condens. Matter Mater. Phys.* **2012**, *86*, 245110.

(212) Shephard, M. J.; Paddon-Row, M. N.; Jordan, K. D. Why Is a Simple n-Alkyl Bridge More Efficient Than a Polynorbornyl Bridge at Mediating Through-Bond Coupling? *J. Am. Chem. Soc.* **1994**, *116*, 5328−5333.

(213) Valiev, M.; Bylaska, E. J.; Govind, N.; Kowalski, K.; Straatsma, T. P.; Van Dam, H. J. J.; Wang, D.; Nieplocha, J.; Apra, E.; Windus, T. L.; et al. NWChem: A comprehensive and scalable open-source solution for large scale molecular simulations. *Comput. Phys. Commun.* **2010**, *181*, 1477−1489.

(214) Shao, Y.; Molnar, L. F.; Jung, Y.; Kussmann, J.; Ochsenfeld, C.; Brown, S. T.; Gilbert, A. T. B.; Slipchenko, L. V.; Levchenko, S. V.; O'Neill, D. P.; et al. Advances in methods and algorithms in a modern quantum chemistry program package. *Phys. Chem. Chem. Phys.* **2006**, *8*, 3172−3191.

(215) Köster, A. M.; Calaminici, P.; Casida, M. E.; Flores-Moreno, R.; Geudtner, G.; Goursot, A.; Heine, T.; Ipatov, A.; Janetzko, F.; del Campo, J. M.; et al. deMon developers. *deMon2k*; 2006.

(216) Bowler, D. R.; Choudhury, R.; Gillan, M. J.; Miyazaki, T. Recent progress with large-scale ab initio calculations: the CONQUEST code. *Phys. Status Solidi B* **2006**, *243*, 989−1000.

(217) CPMD version 4.1, The CPMD Consortium. MPI für Festkörperforschung and the IBM Zurich Research Laboratory, 2015. http://www.cpmd.org.

(218) de la Lande, A.; Babcock, N. S.; Řezáč, J.; Sanders, B. C.; Salahub, D. R. Surface residues dynamically organize water bridges to enhance electron transfer between proteins. *Proc. Natl. Acad. Sci. U. S. A.* **2010**, *107*, 11799−11804.

(219) Řezáč, J.; Levy, B.; Demachy, I.; de la Lande, A. Robust and Efficient Constrained DFT Molecular Dynamics Approach for Biochemical Modeling. *J. Chem. Theory Comput.* **2012**, *8*, 418−427.

(220) Langen, R.; Chang, I.-J.; Germanas, J. P.; Richards, J. H.; Winkler, J. R.; Gray, H. B. Electron tunneling in proteins: coupling through a beta-strand. *Science* **1995**, *268*, 1733−1735.

(221) Chen, H.; Ratner, M. A.; Schatz, G. C. Time-Dependent Theory of the Rate of Photo-induced Electron Transfer. *J. Phys. Chem. C* **2011**, *115*, 18810−18821.

(222) Cheng, C.-L.; Evans, J. S.; Van Voorhis, T. V. Simulating molecular conductance using real-time density functional theory. *Phys. Rev. B: Condens. Matter Mater. Phys.* **2006**, *74*, 155112.

(223) Sutton, C.; Sears, J. S.; Coropceanu, V.; Bredas, J.-L. Understanding the Density Functional Dependence of DFT-Calculated Electronic Couplings in Organic Semiconductors. *J. Phys. Chem. Lett.* **2013**, *4*, 919−924.

(224) Zwanzig, R. W. High-Temperature Equation of State by a Perturbation Method. I. Nonpolar Gases. *J. Chem. Phys.* **1954**, *22*, 1420−1426.

(225) Small, D. W.; Matyushov, D. V.; Voth, G. A. The theory of electron transfer reactions: What may be missing? *J. Am. Chem. Soc.* **2003**, *125*, 7470−7478.

(226) Miller, J. R.; Calcaterra, L. T.; Closs, G. L. Intramolecular long-distance electron transfer in radical anions. The effects of free energy and solvent on the reaction rates. *J. Am. Chem. Soc.* **1984**, *106*, 3047−3049.

(227) Mines, G. A.; Bjerrum, M. J.; Hill, M. G.; Casimiro, D. R.; Chang, I.-J.; Winkler, J. R.; Gray, H. B. Rates of heme oxidation and reduction in Ru(His33)cytochrome c at very high driving forces. *J. Am. Chem. Soc.* **1996**, *118*, 1961−1965.

(228) Blumberger, J.; Lamoureux, G.; Klein, M. L. *J. Chem. Theory Comput.* **2007**, *3*, 1837−1850.

(229) Simonson, T. Gaussian fluctuations and linear response in an electron transfer protein. *Proc. Natl. Acad. Sci. U. S. A.* **2002**, *99*, 6544−6549.

(230) Blumberger, J.; Klein, M. L. Reorganization free energies for long-range electron transfer in a porphyrin-binding four-helix bundle protein. *J. Am. Chem. Soc.* **2006**, *128*, 13854−13867.

(231) Tipmanee, V.; Blumberger, J. Kinetics of the terminal electron transfer step in cytochrome c oxidase. *J. Phys. Chem. B* **2012**, *116*, 1876−1883.

(232) LeBard, D. N.; Kapko, V.; Matyushov, D. V. Energetics and kinetics of primary charge separation in bacterial photosynthesis. *J. Phys. Chem. B* **2008**, *112*, 10322−10342.

(233) LeBard, D. N.; Matyushov, D. V. Energetics of bacterial photosynthesis. *J. Phys. Chem. B* **2009**, *113*, 12424−12437.

(234) LeBard, D. N.; Matyushov, D. V. Proteinwater electrostatics and principles of bioenergetics. *Phys. Chem. Chem. Phys.* **2010**, *12*, 15335−15348.

(235) Matyushov, D. V.; Voth, G. A. Modeling the free energy surfaces of electron transfer in condensed phases. *J. Chem. Phys.* **2000**, *113*, 5413−5424.

(236) Sulpizi, M.; Raugei, S.; VandeVondele, J.; Carloni, P.; Sprik, M. Calculation of redox properties: Understanding short- and long-range effects in rubredoxin. *J. Phys. Chem. B* **2007**, *111*, 3969−3976.

(237) Alfonso-Prieto, M.; Oberhofer, H.; Klein, M. L.; Rovira, C.; Blumberger, J. Proton Transfer Drives Protein Radical Formation in Helicobacter pylori Catalase but Not in Penicillium vitale Catalase. *J. Am. Chem. Soc.* **2011**, *133*, 4285−4298.

(238) Cascella, M.; Magistrato, A.; Tavernelli, I.; Carloni, P.; Röthlisberger, U. Role of protein frame and solvent for the redox properties of azurin from Pseudomonas aeruginosa. *Proc. Natl. Acad. Sci. U. S. A.* **2006**, *103*, 19641−19646.

(239) Hu, L.; Farrokhnia, M.; Heimdal, J.; Shleev, S.; Rulisek, L.; Ryde, U. Reorganization Energy for Internal Electron Transfer in Multicopper Oxidases. *J. Phys. Chem. B* **2011**, *115*, 13111−13126.

(240) Futera, Z.; Sodeyama, K.; Burda, J. V.; Einaga, Y.; Tateyama, Y. A double-QM/MM method for investigating donor acceptor electron-transfer reactions in solution. *Phys. Chem. Chem. Phys.* **2014**, *16*, 19530−19539.

(241) Hu, H.; Lu, Z.; Yang, W. QM/MM Minimum Free-Energy Path: Methodology and Application to Triosephosphate Isomerase. *J. Chem. Theory Comput.* **2007**, *3*, 390−406.

(242) Zeng, X.; Hu, H.; Hu, X.; Cohen, A. J.; Yang, W. Ab initio quantum mechanical/molecular mechanical simulation of electron transfer process: Fractional electron approach. *J. Chem. Phys.* **2008**, *128*, 124510−10.

(243) Hu, H.; Lu, Z.; Parks, J. M.; Burger, S. K.; Yang, W. Quantum mechanics/molecular mechanics minimum free-energy path for accurate reaction energetics in solution and enzymes: Sequential sampling and optimization on the potential of mean force surface. *J. Chem. Phys.* **2008**, *128*, 034105−18.

(244) Zeng, X.; Hu, X.; Yang, W. Fragment-Based Quantum Mechanical/Molecular Mechanical Simulations of Thermodynamic and Kinetic Process of the Ru2+Ru3+ Self-Exchange Electron Transfer. *J. Chem. Theory Comput.* **2012**, *8*, 4960−4967.

(245) Olsson, M. H. M.; Hong, G.; Warshel, A. Frozen Density Functional Free Energy Simulations of Redox Proteins: Computational Studies of the Reduction Potential of Plastocyanin and Rusticyanin. *J. Am. Chem. Soc.* **2003**, *125*, 5025−5039.

(246) Amadei, A.; Daidone, I.; Aschi, M. A general theoretical model for electron transfer reactions in complex systems. *Phys. Chem. Chem. Phys.* **2012**, *14*, 1360−1370.

(247) Amadei, A.; Daidone, I.; Bortolotti, C. A. A general statistical mechanical approach for modeling redox thermodynamics: the reaction and reorganization free energies. *RSC Adv.* **2013**, *3*, 19657−19665.

(248) Bhattacharyya, S.; Stankovich, M.; Truhlar, D.; Gao, J. Combined Quantum Mechanical and Molecular Mechanical Simulations of One- and Two-Electron Reduction Potentials of Flavin Cofactor in Water, Medium-Chain Acyl-CoA Dehydrogenase, and Cholesterol Oxidase. *J. Phys. Chem. A* **2007**, *111*, 5729−5742.

(249) Mueller, R.; North, M.; Yang, C.; Hati, S.; Bhattacharyya, S. Interplay of Flavins Redox States and Protein Dynamics: An Insight from QM/MM Simulations of Dihydronicotinamide Riboside Quinone Oxidoreductase 2. *J. Phys. Chem. B* **2011**, *115*, 3632−3641.

(250) Woiczikowski, P. B.; Steinbrecher, T.; Kubař, T.; Elstner, M. Nonadiabatic QM/MM Simulations of Fast Charge Transfer in Escherichia coli DNA Photolyase. *J. Phys. Chem. B* **2011**, *115*, 9846−9863.

(251) Sigfridsson, E.; Olsson, M.; Ryde, U. A Comparison of the Inner-Sphere Reorganization Energies of Cytochromes, Iron-Sulfur Clusters, and Blue Copper Proteins. *J. Phys. Chem. B* **2001**, *105*, 5546−5552.

(252) Muegge, I.; Qi, P. X.; Wand, A. J.; Chu, Z. T.; Warshel, A. The reorganization energy of cytochrome c revisited. *J. Phys. Chem. B* **1997**, *101*, 825−836.

(253) Tipmanee, V. Towards a quantitative prediction of reorganisation energy for intraprotein electron transfer. Ph.D. Thesis, University of Cambridge, 2012.

(254) Breuer, M.; Zarzycki, P.; Blumberger, J.; Rosso, K. M. Thermodynamics of electron flow in the bacterial deca-heme cytochrome MtrF. *J. Am. Chem. Soc.* **2012**, *134*, 9868−9871.

(255) Sterpone, F.; Ceccarelli, M.; Marchi, M. Linear response and electron transfer in complex biomolecular systems and a reaction center protein. *J. Phys. Chem. B* **2003**, *107*, 11208−11215.

(256) Doukov, T. I.; Blasiak, L. C.; Seravalli, J.; Ragsdale, S. W.; Drennan, C. L. Xenon in and at the End of the Tunnel of Bifunctional Carbon Monoxide Dehydrogenase/Acetyl-CoA Synthase. *Biochemistry* **2008**, *47*, 3474−3483.

(257) Clarke, T. A.; Edwards, M.; Gates, A.; Hall, A.; White, G.; Bradley, J.; Reardon, C.; Shi, L.; Beliaev, A.; Marshall, M. J.; et al. Structure of a bacterial cell surface decaheme electron conduit. *Proc. Natl. Acad. Sci. U. S. A.* **2011**, *108*, 9384−9389.

(258) Renger, T.; Marcus, R. A. Variable-Range Hopping Electron Transfer through Disordered Bridge States: Application to DNA. *J. Phys. Chem. A* **2003**, *107*, 8404−8419.

(259) Warren, J. J.; Ener, M. E.; Vlcek, A., Jr.; Winkler, J. R.; Gray, H. B. Electron hopping through proteins. *Coord. Chem. Rev.* **2012**, *256*, 2478−2487.

(260) Warren, J. J.; Herrera, N.; Hill, M. G.; Winkler, J. R.; Gray, H. B. Electron Flow through Nitrotyrosinate in Pseudomonas aeruginosa Azurin. *J. Am. Chem. Soc.* **2013**, *135*, 11151−11158.

(261) Warren, J. J.; Winkler, J. R.; Gray, H. B. Hopping maps for photosynthetic reaction centers. *Coord. Chem. Rev.* **2013**, *257*, 165−170.

(262) Matyushov, D. V. Nonergodic activated kinetics in polar media. *J. Chem. Phys.* **2009**, *130*, 164522−8.

(263) Robin, M.; Day, P. Mixed Valence Chemistry-A Survey and Classification. *Adv. Inorg. Chem. Radiochem.* **1968**, *10*, 247−422.

(264) Gautier, N.; Dumur, F.; Lloveras, V.; Vidal-Gancedo, J.; Veciana, J.; Rovira, C.; Hudhomme, P. Intramolecular Electron Transfer Mediated by a Tetrathiafulvalene Bridge in a Purely Organic Mixed-Valence System. *Angew. Chem., Int. Ed.* **2003**, *42*, 2765−2768.

(265) Richardson, D. E.; Taube, H. Mixed-Valence Molecules: Electronic Delocalization and Stabilization. *Coord. Chem. Rev.* **1984**, *10*, 107−129.

(266) Warshel, A. Bicycle-pedal model for the first step in the vision process. *Nature* **1976**, *260*, 679−683.

(267) Warshel, A.; Hwang, J.-K. Simulation of the dynamics of electron transfer reactions in polar solvents: Semiclassical trajectories and dispersed polaron approaches. *J. Chem. Phys.* **1986**, *84*, 4938−5957.

(268) Creighton, S.; Hwang, J.-K.; Warshel, A.; Parson, W., W.; Norris, J. Simulating the Dynamics of the Primary Charge Separation Process in Bacterial Photosynthesis. *Biochemistry* **1988**, *27*, 774−781.

(269) Tully, J. C. Molecular Dynamics with electronic transitions. *J. Chem. Phys.* **1990**, *93*, 1061−1071.

(270) Tully, J. C. In *Classical and Quantum Dynamics in Condensed Phase Simulations*; Berne, B. J., Ciccotti, G., Coker, D. F., Eds.; World Scientific: Singapore, 1998; pp 34−71.

(271) Tully, J. C. Mixed Quantum-Classical Dynamics. *Modern Methods for Multidimensional Dynamics Computations in Chemistry*; World Scientific: Singapore, 1998; pp 493−514

(272) Akimov, A. V.; Neukirch, A. J.; Prezhdo, O. V. Theoretical Insights into Photoinduced Charge Transfer and Catalysis at Oxide Interfaces. *Chem. Rev.* **2013**, *113*, 4496−4565.

(273) Ding, F.; Chapman, C. T.; Liang, W.; Li, X. Mechanisms of bridge-mediated electron transfer: A TDDFT electronic dynamics study. *J. Chem. Phys.* **2012**, *137*, 22A512−9.

(274) Niehaus, T. A.; Heringer, D.; Torralva, B.; Frauenheim, T. Importance of electronic self-consistency in the TDDFT based treatment of nonadiabatic molecular dynamics. *Eur. Phys. J. D* **2005**, *35*, 467−477.

(275) Kubař, T.; Elstner, M. Coarse-grained time-dependent density functional simulation of charge transfer in complex systems: application to hole transfer in DNA. *J. Phys. Chem. B* **2010**, *114*, 11221−11240.

(276) Troisi, A. Charge transport in high mobility molecular semiconductors: calssical models and new theories. *Chem. Soc. Rev.* **2011**, *40*, 2347−2358.

(277) Gajdos, F.; Oberhofer, H.; Dupuis, M.; Blumberger, J. On the Inapplicability of Electron-Hopping Models for the Organic Semiconductor Phenyl-C61-butyric Acid Methyl Ester (PCBM). *J. Phys. Chem. Lett.* **2013**, *4*, 1012−1017.

(278) Troisi, A.; Orlandi, G. Charge-Transport Regime of Crystalline Organic Semiconductors: Diffusion Limited by Thermal Off-Diagonal Electronic Disorder. *Phys. Rev. Lett.* **2006**, *96*, 086601.

(279) Wang, L.; Beljonne, D. Flexible Surface Hopping Approach to Model the Crossover from Hopping to Band-like Transport in Organic Crystals. *J. Phys. Chem. Lett.* **2013**, *4*, 1888−1894.

(280) Wang, L.; Beljonne, D. Charge transport in organic semiconductors: Assessment of the mean field theory in the hopping regime. *J. Chem. Phys.* **2013**, *139*, 064316−12.

(281) Wang, L.; Prezhdo, O. V.; Beljonne, D. Mixed quantum-classical dynamics for charge transport in organics. *Phys. Chem. Chem. Phys.* **2015**, *17*, 12395−12406.

(282) Ren, J.; Vukmirovic, N.; Wang, L.-W. Nonadiabatic molecular dynamics simulation for carrier transport in a pentathiophene butyric acid monolayer. *Phys. Rev. B: Condens. Matter Mater. Phys.* **2013**, *87*, 205117.

(283) Plasser, F.; Granucci, G.; Pittner, J.; Barbatti, M.; Persico, M.; Lischka, H. Surface hopping dynamics using a locally diabatic formalism: Charge transfer in the ethylene dimer cation and excited state dynamics in the 2-pyridone dimer. *J. Chem. Phys.* **2012**, *137*, 22A514−13.

(284) Curchod, B. F.; Penfold, T. J.; Rothlisberger, U.; Tavernelli, I. Nonadiabatic ab initio molecular dynamics using linear-response time-dependent density functional theory. *Open Phys.* **2013**, *11*, 1059−1065.

(285) Tully, J. C. Perspective: Nonadiabatic dynamics theory. *J. Chem. Phys.* **2012**, *137*, 22A301−7.

(286) Zhu, C.; Nangia, S.; Jasper, A. W.; Truhlar, D. G. Coherent switching with decay of mixing: An improved treatment of electronic coherence for non-Born-Oppenheimer trajectories. *J. Chem. Phys.* **2004**, *121*, 7658−7670.

(287) Zhu, C.; Jasper, A. W.; Truhlar, D. G. Non-Born-Oppenheimer Liouville-von Neumann Dynamics. Evolution of a Subsystem Controlled by Linear and Population-Driven Decay of Mixing with Decoherent and Coherent Switching. *J. Chem. Theory Comput.* **2005**, *1*, 527−540.

(288) Jasper, A. W.; Nangia, S.; Zhu, C.; Truhlar, D. G. Non-Born-Oppenheimer Molecular Dynamics. *Acc. Chem. Res.* **2006**, *39*, 101−108.

(289) Schmidt, J. R.; Shenvi, N.; Tully, J. C. Mixed quantum-classical equilibrium: Surface hopping. *J. Chem. Phys.* **2008**, *129*, 114110−6.

(290) Sherman, M. C.; Corcelli, S. A. Thermal equilibrium properties of surface hopping with an implicit Langevin bath. *J. Chem. Phys.* **2015**, *142*, 024110−8.

(291) Shushkov, P.; Li, R.; Tully, J. C. Ring polymer molecular dynamics with surface hopping. *J. Chem. Phys.* **2012**, *137*, 22A549−12.

(292) Craig, I. R.; Manolopoulos, D. E. Quantum statistics and classical mechanics: Real time correlation functions from ring polymer molecular dynamics. *J. Chem. Phys.* **2004**, *121*, 3368−3373.

(293) Prezhdo, O. V.; Rossky, P. J. Evaluation of quantum transition rates from quantum-classical molecular dynamics simulations. *J. Chem. Phys.* **1997**, *107*, 5863−5878.

(294) Fang, J. Y.; Hammes-Schiffer, S. Improvement of the Internal Consistency in Trajectory Surface Hopping. *J. Phys. Chem. A* **1999**, *103*, 9399−9407.

(295) Granucci, G.; Persico, M. Critical appraisal of the fewest switches algorithm for surface hopping. *J. Chem. Phys.* **2007**, *126*, 134114−11.

(296) Shenvi, N.; Subotnik, J. E.; Yang, W. Simultaneous-trajectory surface hopping: A parameter-free algorithm for implementing decoherence in nonadiabatic dynamics. *J. Chem. Phys.* **2011**, *134*, 144102−12.

(297) Landry, B. R.; Subotnik, J. E. How to recover Marcus theory with fewest switches surface hopping: Add just a touch of decoherence. *J. Chem. Phys.* **2012**, *137*, 22A513−13.

(298) Landry, B. R.; Subotnik, J. E. Standard surface hopping predicts incorrect scaling for Marcus golden-rule rate: The decoherence problem cannot be ignored. *J. Chem. Phys.* **2011**, *135*, 191101−4.

(299) Feynman, R. P.; Hibbs, A. R. *Quantum Mechanics and Path Integrals*; McGraw-Hill: New York, 1965.

(300) Chandler, D.; Wolynes, P. G. Exploiting the isomorphism between quantum theory and classical statistical mechanics of polyatomic fluids. *J. Chem. Phys.* **1981**, *74*, 4078−4095.

(301) Benjamin, I.; Nitzan, A. Path-integral computations of tunneling processes. *J. Chem. Phys.* **2005**, *123*, 104103−8.

(302) Marchi, M.; Chandler, D. Pathintegral calculation of the tunnel splitting in aqueous ferrousferric electron transfer. *J. Chem. Phys.* **1991**, *95*, 889−894.

(303) Richardson, J. O.; Althorpe, S. C. Ring-polymer molecular dynamics rate-theory in the deep-tunneling regime: Connection with semiclassical instanton theory. *J. Chem. Phys.* **2009**, *131*, 214106−12.

(304) Hele, T. J. H.; Althorpe, S. C. Derivation of a true (t 0+) quantum transition-state theory. I. Uniqueness and equivalence to ring-polymer molecular dynamics transition-state-theory. *J. Chem. Phys.* **2013**, *138*, 084108−13.

(305) Menzeleev, A. R.; Ananth, N.; Miller, T. F., III. Direct simulation of electron transfer using ring polymer molecular dynamics: Comparison with semiclassical instanton theory and exact quantum methods. *J. Chem. Phys.* **2011**, *135*, 074106−17.

(306) Sprik, M.; Impey, R. W.; Klein, M. L. Study of electron solvation in polar solvents using path integral calculations. *J. Stat. Phys.* **1986**, *43*, 967−972.

(307) Breuer, M.; Zarzycki, P.; Shi, L.; Clarke, T. A.; Edwards, M.; Butt, J.; Richardson, D. J.; Fredrickson, J. K.; Zachara, J. M.; Blumberger, J.; et al. Molecular Structure and Free Energy Landscape for Electron Transport in the Deca-Heme Cytochrome MtrF. *Biochem. Soc. Trans.* **2012**, *40*, 1198−1203.

(308) Amashukeli, X.; Gruhn, N. E.; Lichtenberger, D. L.; Winkler, J. R.; Gray, H. B. Inner-sphere electron-transfer reorganization energies of zinc porphyrins. *J. Am. Chem. Soc.* **2004**, *126*, 15566−15571.

(309) Blumberger, J.; Lamoureux, G. Reorganization free energies and quantum corrections for a model electron self-exchange reaction: comparison of polarizable and non-polarizable solvent models. *Mol. Phys.* **2008**, *106*, 1597−1611.

(310) Lide, D. R. *CRC Handbook of Chemistry and Physics*; CRC Press: Boca Raton, FL, 1995.

(311) Gupta, S.; Matyushov, D. V. Effects of solvent and solute polarizability on the reorganization energy of electron transfer. *J. Phys. Chem. A* **2004**, *108*, 2087−2096.

(312) Meade, T. J.; Gray, H. B.; Winkler, J. R. Driving-force effects on the rate of long-range electron transfer in ruthenium-modified cytochrome c. *J. Am. Chem. Soc.* **1989**, *111*, 4353−4356.

(313) Di Bilio, A. J.; Hill, M. G.; Bonander, N.; Karlsson, B. G.; Villahermosa, R. M.; Malmström, B. G.; Winkler, J. R.; Gray, H. B. Reorganization energy of blue copper: Effects of temperature and driving force on the rates of electron transfer in ruthenium- and osmium-modified azurins. *J. Am. Chem. Soc.* **1997**, *119*, 9921−9922.

(314) Caldwell, J. W.; Kollman, P. A. Structure and Properties of Neat Liquids Using Nonadditive Molecular Dynamics: Water, Methanol, and N-Methylacetamide. *J. Phys. Chem.* **1995**, *99*, 6208−6219.

(315) Ren, P.; Ponder, J. W. Polarizable atomic multipole water model for molecular mechanics simulation. *J. Phys. Chem. B* **2003**, *107*, 5933−5947.

(316) Crane, B. R.; Di Bilio, A. J.; Winkler, J. R.; Gray, H. B. Electron Tunneling in Single Crystals of Pseudomonas aeruginosa Azurins. *J. Am. Chem. Soc.* **2001**, *123*, 11623−11631.

(317) Iwata, S.; Ostermeier, C.; Ludwig, B.; Michel, H. Structure at 2.8 A resolution of cytochrome c oxidase from Paracoccus denitrificans. *Nature* **1995**, *376*, 660−669.

(318) Ostermeier, C.; Harrenga, A.; Ermler, U.; Michel, H. Structure at 2.7 A resolution of the Paracoccus denitrificans two-subunit cytochrome c oxidase complexed with an antibody FV fragment. *Proc. Natl. Acad. Sci. U. S. A.* **1997**, *94*, 10547−10553.

(319) Yoshikawa, S.; Shinzawa-Itoh, K.; Nakashima, R.; Yaono, R.; Yamashita, E.; Inoue, N.; Yao, M.; Fei, M. J.; Libeu, C. P.; Mizushima, T.; et al. Redox-coupled crystal structural changes in bovine heart cytochrome c oxidase. *Science* **1998**, *280*, 1723−1729.

(320) Tsukihara, T.; Shimokata, K.; Katayama, Y.; Shimada, H.; Muramoto, K.; Aoyama, H.; Mochizuki, M.; Shinzawa-Itoh, K.; Yamashita, E.; Yao, M.; et al. The low-spin heme of cytochrome c oxidase as the driving element of the proton-pumping process. *Proc. Natl. Acad. Sci. U. S. A.* **2003**, *100*, 15304−15309.

(321) Thomas, J. W.; Puustinen, A.; Alben, J. O.; Gennis, R. B.; Wikstrom, M. Substitution of asparagine for aspartate-135 in subunit I of the cytochrome bo ubiquinol oxidase of Escherichia coli eliminates proton-pumping activity. *Biochemistry* **1993**, *32*, 10923−10928.

(322) Junemann, S.; Meunier, B.; Fisher, N.; Rich, P. R. Effects of Mutation of the Conserved Glutamic Acid-286 in Subunit I of Cytochrome c Oxidase from Rhodobacter sphaeroides. *Biochemistry* **1999**, *38*, 5248−5255.

(323) Pawate, A. S.; Morgan, J.; Namslauer, A.; Mills, D.; Brzezinski, P.; Ferguson-Miller, S.; Gennis, R. B. A mutation in subunit I of cytochrome oxidase from Rhodobacter sphaeroides results in an increase in steady-state activity but completely eliminates proton pumping. *Biochemistry* **2002**, *41*, 13417−13423.

(324) Faxen, K.; Gilderson, G.; Adelroth, P.; Brzezinski, P. A mechanistic principle for proton pumping by cytochrome c oxidase. *Nature* **2005**, *437*, 286−289.

(325) Belevich, I.; Verkhovsky, M. I.; Wikstrom, M. Proton-coupled electron transfer drives the proton pump of cytochrome c oxidase. *Nature* **2006**, *440*, 829−832.

(326) Brzezinski, P.; Larsson, G. Redox-driven proton pumping by heme-copper oxidases. *Biochim. Biophys. Acta, Bioenerg.* **2003**, *1605*, 1−13.

(327) Rich, P. R.; Breton, J. Attenuated Total Reflection Fourier Transform Infrared Studies of Redox Changes in Bovine Cytochrome c Oxidase: Resolution of the Redox Fourier Transform Infrared Difference Spectrum of Heme a3. *Biochemistry* **2002**, *41*, 967−973.

(328) Iwaki, M.; Puustinen, A.; Wikstrom, M.; Rich, P. R. ATR-FTIR Spectroscopy and Isotope Labeling of the PM Intermediate of Paracoccus denitrificans Cytochrome c Oxidase. *Biochemistry* **2004**, *43*, 14370−14378.

(329) Iwaki, M.; Puustinen, A.; Wikstrom, M.; Rich, P. R. Structural and Chemical Changes of the PM Intermediate of Paracoccus denitrificans Cytochrome c Oxidase Revealed by IR Spectroscopy with Labeled Tyrosines and Histidine. *Biochemistry* **2006**, *45*, 10873−10885.

(330) Popovic, D. M.; Stuchebrukhov, A. A. Proton pumping mechanism and catalytic cycle of cytochrome c oxidase: Coulomb pump model with kinetic gating. *FEBS Lett.* **2004**, *566*, 126−130.

(331) Blomberg, M. R. A.; Siegbahn, P. E. M. Quantum chemistry applied to the mechanisms of transition metal containing enzymes - cytochrome c oxidase, a particularly challenging case. *J. Comput. Chem.* **2006**, *27*, 1373−1384.

(332) Kim, Y. C.; Wikstrom, M.; Hummer, G. Kinetic gating of the proton pump in cytochrome c oxidase. *Proc. Natl. Acad. Sci. U. S. A.* **2009**, *106*, 13707−13712.

(333) Wikstrom, M.; Verkhovsky, M. I.; Hummer, G. Water-gated mechanism of proton translocation by cytochrome c oxidase. *Biochim. Biophys. Acta, Bioenerg.* **2003**, *1604*, 61−65.

(334) Olkhova, E.; Hutter, M. C.; Lill, M. A.; Helms, V.; Michel, H. Dynamic water networks in cytochrome C oxidase from Paracoccus denitrificans investigated by molecular dynamics simulations. *Biophys. J.* **2004**, *86*, 1873−1889.

(335) Xu, J.; Voth, G. A. Computer simulation of explicit proton translocation in cytochrome c oxidase: the D-pathway. *Proc. Natl. Acad. Sci. U. S. A.* **2005**, *102*, 6795−6800.

(336) Olsson, M. H. M.; Sharma, P. K.; Warshel, A. Simulating redox coupled proton transfer in cytochrome c oxidase: Looking for the proton bottleneck. *FEBS Lett.* **2005**, *579*, 2026−2034.

(337) Olsson, M. H. M.; Warshel, A. Monte Carlo simulations of proton pumps: on the working principles of the biological valve that controls proton pumping in cytochrome c oxidase. *Proc. Natl. Acad. Sci. U. S. A.* **2006**, *103*, 6500−6505.

(338) Kaila, V. R. I.; Johansson, M. P.; Sundholm, D.; Wikstrom, M. Interheme electron tunneling in cytochrome c oxidase. *Proc. Natl. Acad. Sci. U. S. A.* **2010**, *107*, 21470−21475.

(339) Rich, P. R.; Marechal, A. Functions of the hydrophilic channels in protonmotive cytochrome c oxidase. *J. R. Soc., Interface* **2013**, *10*, 20130183.

(340) Yi, H.; Nevin, K. P.; Kim, B.-C.; Franks, A. E.; Klimes, A.; Tender, L. M.; Lovley, D. R. Selection of a variant of Geobacter sulfurreducens with enhanced capacity for current production in microbial fuel cells. *Biosens. Bioelectron.* **2009**, *24*, 3498−3503.

(341) Fitzgerald, L. A.; Petersen, E. R.; Gross, B. J.; Soto, C. M.; Ringeisen, B. R.; El-Naggar, M. Y.; Biffinger, J. C. Aggrandizing Power Output from Shewanella oneidensis MR-1 Microbial Fuel Cells using Calcium Chloride. *Biosens. Bioelectron.* **2012**, *31*, 492−498.

(342) Zhuang, K.; Ma, E.; Lovley, D. R.; Mahadevan, R. The design of long-term effective uranium bioremediation strategy using a community metabolic model. *Biotechnol. Bioeng.* **2012**, *109*, 2475−2483.

(343) Edwards, M. J.; Hall, A.; Shi, L.; Fredrickson, J. K.; Zachara, J. M.; Butt, J. N.; Richardson, D. J.; Clarke, T. A. The Crystal Structure of the Extracellular 11-heme Cytochrome UndA Reveals a Conserved 10-heme Motif and Defined Binding Site for Soluble Iron Chelates. *Structure* **2012**, *20*, 1275−1284.

(344) Edwards, M. J.; White, G. F.; Norman, M.; Tome-Fernandez, A.; Ainsworth, E.; Shi, L.; Fredrickson, J. K.; Zachara, J. M.; Butt, J. N.; Richardson, D. J.; et al. Redox Linked Flavin Sites in Extracellular Decaheme Proteins Involved in Microbe-Mineral Electron Transfer. *Sci. Rep.* **2015**, *5*, 11677.

(345) Hartshorne, R. S.; et al. Characterization of an extracellular conduit between bacteria and the extracellular environment. *Proc. Natl. Acad. Sci. U. S. A.* **2009**, *106*, 22169−22174.

(346) Wigginton, N. S.; Rosso, K. M.; Hochella, M. F. Mechanisms of Electron Transfer in Two Decaheme Cytochromes from a Metal-Reducing Bacterium. *J. Phys. Chem. B* **2007**, *111*, 12857−12864.

(347) Breuer, M.; Rosso, K. M.; Blumberger, J.; Butt, J. N. Multi-heme Cytochromes in Shewanella oneidensis MR-1: Structures, Functions and Opportunities. *J. R. Soc., Interface* **2015**, *12*, 20141117.

(348) Lewis, J.; Cheatham, T.; Starikov, E. B.; Wang, H.; Sankey, O. F. Dynamically amorphous character of electronic states in poly(dA)-poly(dT) DNA. *J. Phys. Chem. B* **2003**, *107*, 2581−2587.

(349) Henderson, P. T.; Jones, D.; Hampikian, G.; Kan, Y.; Schuster, G. B. Long-distance charge transport in duplex DNA: the phonon-assisted polaron-like hopping mechanism. *Proc. Natl. Acad. Sci. U. S. A.* **1999**, *96*, 8353−8358.

(350) Liu, C.-S.; Schuster, G. B. Base sequence effects in radical cation migration in duplex DNA: support for the polaron-like hopping model. *J. Am. Chem. Soc.* **2003**, *125*, 6098−6102.

(351) Kubař, T.; Kleinekathofer, U.; Elstner, M. Solvent fluctuations drive the hole transfer in DNA: A mixed quantum-classical study. *J. Phys. Chem. B* **2009**, *113*, 13107−13117.

(352) Park, H. W.; Kim, S. T.; Sancar, A.; Deisenhofer, J. Crystal structure of DNA photolyase from Escherichia coli. *Science* **1995**, *268*, 1866−1872.

(353) Brettel, K.; Byrdin, M. Reaction mechanisms of DNA photolyase. *Curr. Opin. Struct. Biol.* **2010**, *20*, 693−701.

(354) Immeln, D.; Weigel, A.; Kottke, T.; Pérez Lustres, J. L. Primary Events in the Blue Light Sensor Plant Cryptochrome: Intraprotein Electron and Proton Transfer Revealed by Femtosecond Spectroscopy. *J. Am. Chem. Soc.* **2012**, *134*, 12536−12546.

(355) Lüdemann, G.; Solov'yov, I. A.; Kubař, T.; Elstner, M. Solvent Driving Force Ensures Fast Formation of a Persistent and Well-

Separated Radical Pair in Plant Cryptochrome. *J. Am. Chem. Soc.* **2015**, *137*, 1147−1156.

(356) Greco, C.; Fantucci, P.; Ryde, U.; De Gioia, L. Fast Generation of Broken-Symmetry States in a Large System Including Multiple Iron-Sulfur Assemblies: Investigation of QM/MM Energies, Cluster Charges and Spin Populations. *Int. J. Quantum Chem.* **2010**, *111*, 3949−3960.

(357) Kubas, A.; De Sancho, D.; Best, R.; Blumberger, J. Aerobic damage of [FeFe] hydrogenases: activation barriers for O_2 chemical attachment. *Angew. Chem., Int. Ed.* **2014**, *53*, 4081−4084.

(358) Siwko, M. E.; Corni, S. Cytochrome C on a gold surface: investigating structural relaxations and their role in protein surface electron transfer by molecular dynamics simulations. *Phys. Chem. Chem. Phys.* **2013**, *15*, 5945−5956.

(359) Kerisit, S.; Rosso, K. M.; Dupuis, M.; Valiev, M. Molecular Computational Investigation of Electron-Transfer Kinetics Across Cytochrome-Iron Oxide Interfaces. *J. Phys. Chem. C* **2007**, *111*, 11363−11375.

(360) Polizzi, N. F.; Skourtis, S. S.; Beratan, D. N. Physical constraints on charge transport through bacterial nanowires. *Faraday Discuss.* **2012**, *155*, 43−62.

(361) Migliore, A.; Nitzan, A. Irreversibility and Hysteresis in Redox Molecular Conduction Junctions. *J. Am. Chem. Soc.* **2013**, *135*, 9420−9432.

(362) Case, D. A.; Darden, T.; Cheatham, T., III; Simmerling, C.; Wang, J.; Duke, R.; Luo, R.; Crowley, M.; Walker, R. C.; Zhang, W. et al. *AMBER 10*; University of California: San Francisco, 2008.

(363) Jorgensen, W. L.; Chandrasekhar, J.; Madura, J. D.; Impey, R. W.; Klein, M. L. Comparison of simple potential functions for simulating liquid water. *J. Chem. Phys.* **1983**, *79*, 926−935.

(364) Holzapfel, W.; Finkele, U.; Kaiser, W.; Oesterhelt, D.; Scheer, H.; Stilz, H. U.; Zinth, W. Initial electron-transfer in the reaction center from Rhodobacter sphaeroides. *Proc. Natl. Acad. Sci. U. S. A.* **1990**, *87*, 5168−5172.

(365) Bernhard, P.; Helm, L.; Ludi, A.; Merbach, A. E. Direct measurement of a prominent outer-sphere electron self-exhchange - kinetic parameters for the hexaaquaruthenium(II)/(III) couple determined by O-17 and Ru-99 NMR. *J. Am. Chem. Soc.* **1985**, *107*, 312−317.

(366) Image from http://www.physics.purdue.edu/sergei/Photosynthesis.

(367) Image courtesy of Prof. P. L. Dutton, University of Pennsylvania.

(368) Drobizhev, M.; Makarov, N. S.; Tillo, S. E.; Hughes, T. E.; Rebane, A. Describing Two-Photon Absorptivity of Fluorescent Proteins with a New Vibronic Coupling Mechanism. *J. Phys. Chem. B* **2012**, *116*, 1736−1744.